2012

Hybrid femtosecond/picosecond coherent anti-Stokes Raman scattering for gas-phase temperature measurements

Joseph Daniel Miller
Iowa State University

Hybrid femtosecond/picosecond coherent anti-Stokes Raman scattering for gas-phase temperature measurements

by

Joseph Daniel Miller

A dissertation submitted to the graduate faculty

in partial fulfillment of the requirements for the degree of

DOCTOR OF PHILOSOPHY

Major: Mechanical Engineering

Program of Study Committee:
Terrence R. Meyer, Major Professor
Rodney O. Fox
James R. Gord
Michael G. Olsen
Shankar Subramaniam
Jigang Wang

Iowa State University

Ames, Iowa

2012

Dedicated to my beautiful and patient wife, Lana

"I am the Light of the world; he who follows me will not walk in the darkness, but will have the Light of life."
- Jesus the Christ (John 8:12 NAS)

"I was merely thinking God's thoughts after Him. Since we ... are priests of the highest God in regard to the book of nature, it benefits us to be thoughtful, not of the glory of our minds, but rather, above all else, of the glory of God."
- Johannes Kepler

TABLE OF CONTENTS

LIST OF TABLES

LIST OF FIGURES

ABSTRACT

Hybrid femtosecond/picosecond coherent anti-Stokes Raman scattering (fs/ps CARS) is employed for quantitative gas-phase temperature measurements in combustion processes and heated flows. In this approach, ultrafast 100-fs laser pulses are used to induce vibrational and rotational transitions in N_2 and O_2, while a third spectrally narrowed picosecond pulse is used to probe the molecular response. Temporal suppression of the nonresonant contribution and elimination of collisional effects are achieved by delay of the probe pulse, while sufficient spectral resolution is maintained for frequency-domain detection and thermometry. A theoretical framework is developed to model experimental spectra by phenomenologically describing the temporal evolution of the vibrational and rotational wavepackets as a function of temperature and pressure.

Interference-free, single-shot vibrational fs/ps CARS thermometry is demonstrated at 1-kHz from 1400–2400 K in a H_2-air flame, with accuracy better than 3%. A time-asymmetric exponential pulse shape is introduced to optimize nonresonant suppression with a 10^3 reduction at a probe delay of 0.31 ps. Low-temperature single-shot thermometry (300–700 K) with better than 1.5% accuracy is demonstrated using a fully degenerate rotational fs/ps CARS scheme, and the influence of collision energy transfer on thermometry error is quantified at atmospheric pressure. Interference-free thermometry, without nonresonant contributions and collision-induced error, is demonstrated for the first time using rotational fs/ps CARS at room temperature and pressures from 1–15 atm. Finally, the temporal and spectral resolution of fs/ps CARS is exploited for transition-resolved time-domain measurements of N_2 and O_2 self-broadened *S*-branch Raman linewidths at pressures of 1–20 atm.

CHAPTER 1. INTRODUCTION

This dissertation introduces a new approach to quantitative coherent anti-Stokes Raman scattering (CARS) thermometry in gas-phase reacting flows. In traditional nanosecond CARS, the temporal response of the probed molecule is ignored while in time-domain CARS, the frequency-domain information is not directly resolved. In this dissertation, hybrid femtosecond/picosecond coherent anti-Stokes Raman scattering ("fs/ps CARS" or "hybrid CARS") is used to investigate both the temporal and spectral response of the probed molecule for quantitative thermometry. If one considers an analogy to a piece of music, frequency domain CARS yields information about the notes played in a given piece (key signature) but neglects to inform us of the temporal pattern associated with each note. In contrast, time-domain CARS reveals the beat of the musical piece (time signature and tempo) yet obscures information about the notes associated with the beat pattern. Therefore, this dissertation endeavors to introduce a simultaneously time- and frequency-resolved CARS technique with sufficient temporal resolution for suppression of interference from nonresonant background and collision energy transfer and sufficient spectral resolution for quantitative frequency-domain detection of individual energy transitions for thermometry and chemical identification.

1.1 Motivation

Combustion is a critical component of energy production with nearly 84% of all energy in the United States derived from combustion processes in 2010 as shown in Fig. 1.1 [1]. While combustion reactions have been studied for thousands of years, significant

challenges remain including the reduction of pollutant emissions and increase in combustion efficiency. This is particularly important in the combustion of alternative (e.g., biomass-derived) fuels where chemical composition may vary as a function of feedstock and conversion technology. Solutions to these challenges are limited by our inability to both measure and predict the formation of key intermediate species (CH, NO, OH, CH_2O) and thermodynamic properties (temperature, pressure, species concentration). These properties are inherently time varying in practical combustors and highly dependent on fluid–flame interactions. It is therefore critical to measure fundamental thermodynamic parameters within the reaction zone at rates characteristic of the energetic combustion instabilities (0.1–10 kHz) which influence combustion quality.

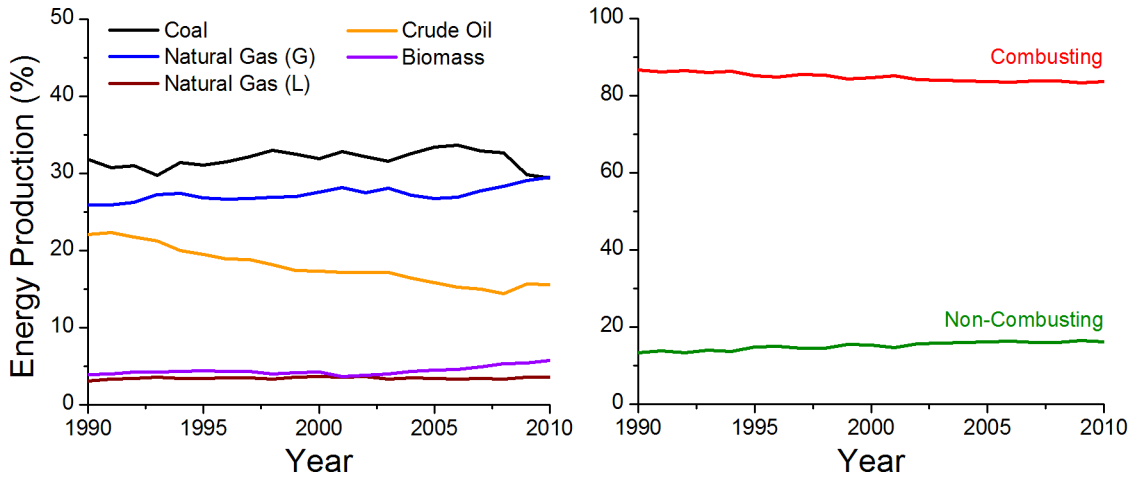

Figure 1.1. Percentage of total energy production as a function of source (left) and process (right) from 1990–2010 from Ref. [1].

Of particular importance is the ability to provide high-fidelity data sets for validation of combustion theory and predictive models. Simultaneous time-dependent measurements of temperature, pressure, and the concentration of major species are specifically needed due to

their prominent role in the formation of highly-reactive intermediate species. In general, the state of a combustion reaction is driven by the chemical kinetics of the associated global and elementary reactions [2]. A global reaction mechanism is comprised of a series of elementary reactions, typically consisting of one- two- or three-molecule reactions, each of which have independent reaction rates. The rate at which the reactions occur coupled with the fluid dynamics of the system dictate the stability of the combustion process and resulting products. In general, for a bimolecular reaction

$$A + B \xrightarrow{k} C + D \tag{1.1}$$

with reactants A and B, products C and D, and rate k, the rate of production of species C is given by

$$\frac{d[C]}{dt} = A_c T^b \exp\left(\frac{-E_A}{RT}\right)[A][B] \tag{1.2}$$

where A_c is the pre-exponential factor which describes the frequency of collisions (contains units of kmol/m^{3}s), T is the temperature (K), E_A is the activation energy of the reaction (kJ/kmol), R is the ideal gas constant (kJ/kmol K), $[A]$ is the molar concentration of species A (kmol/m^3), and $[B]$ is the molar concentration of species B. From Eq 1.2, it is evident that the temperature and species concentrations are primary variables in the formation of new species. For example, the production of thermal NO is described in a simple manner by the extended Zeldovich mechanism

$$\frac{d[NO]}{dt} = 3.6 \times 10^{11} \exp\left(\frac{-38370}{T}\right)[O][N_2] \tag{1.3}$$

where temperature, oxygen, and nitrogen play major roles in the pollutant's time-dependent formation.

1.2 Coherent Anti-Stokes Raman Scattering

For nearly four decades, coherent anti-Stokes Raman scattering (CARS) spectroscopy has been utilized to measure both temperature and species concentrations of major and minor species in combustion environments [3]. The advantages of CARS spectroscopy stem from the importance of temperature and species concentration measurements in combustion reactions as highlighted in Eqs. 1.2 and 1.3. CARS spectroscopy is uniquely suited for temperature and species measurements due to its direct measurement of the temperature-dependent Boltzmann-distributed population of vibrational and rotational energy states. In this regard, the spectral structure is highly temperature dependent, while the amplitude of the signal is related to the concentration of the targeted species. While absolute concentration measurements are challenging, relative concentration measurements with respect to major species have been highly successful. Diatomic nitrogen is most frequently measured due to its low activity and high relative concentration in air-breathing combustion.

CARS is particularly applicable to high-temperature and high-pressure systems where traditional thermocouple measurements exhibit large errors due to conduction, convection, and radiation heat transfer. Furthermore, as a laser-based diagnostic tool CARS measurements are *in situ*, meaning the spectroscopic process occurs in the sample volume, and non-invasive. As such, temperature and species-extraction probes which disturb the chemical and fluid dynamics of the system are avoided. Additionally, the laser-like CARS signal exhibits a third-order dependence on laser power, and can be spatially separated from background scatter with high collection efficiency. As a result, CARS can be applied in harsh combustion conditions to provide accurate and precise temperature and species measurements where physical probe techniques are not feasible.

1.3 Objectives

Although CARS thermometry has become the *de facto* method for high-accuracy thermometry in combustion reactions over the past 40 years, several significant challenges complicate data analysis and limit accuracy and precision in practical combustion systems. Four primary challenges have driven innovation in gas-phase CARS research over the past four decades [4]: (*i*) the simultaneous measurement of temperature and concentration of multiple species using a single CARS system, (*ii*) the application of CARS systems to challenging combustion environments, (*iii*) the suppression of nonresonant background and collisional energy transfer effects in CARS measurements at high pressure and high temperature, and (*iv*) the measurement of temperature and species concentration at high repetition rates (1 kHz or higher) to investigate transient instabilities and phenomena associated with turbulent reacting flows. Although many innovative variations on the CARS technique have been employed, no single technique has been developed which addresses all four challenges. A particularly promising CARS technique with recent application in condensed-phase sensing is fs/ps CARS [5-8]. While its applicability for identifying molecules with widely spaced and broad vibrational Raman transitions has been documented in several publications, its suitability for quantitative gas-phase thermometry is unknown. Therefore, the goal of this dissertation is to develop, characterize, and apply quantitative hybrid fs/ps CARS thermometry to address each of the four challenges outlined above. In this regard, this dissertation aims to achieve the following objectives:

Objective 1: To develop a theoretical framework for hybrid fs/ps CARS thermometry in gas-phase combustion reactions, with particular emphasis on the use of vibrational and pure-rotational transitions of N_2 and O_2 (*i*).

Objective 2: To investigate the suppression of nonresonant contributions through temporal delay and spectral shaping of the CARS probe pulse (*ii* and *iii*).

Objective 3: To quantify collision-induced thermometry error as a function of probe delay, validate the collision-free assumption for hybrid fs/ps CARS thermometry, and determine appropriate linewidth models when necessary by providing direct measurements of Raman linewidths (*ii* and *iii*).

Objective 4: To demonstrate accurate and precise temperature measurements using a single laser source at a repetition rate of 1 kHz (*iv*).

1.4 Organization of the Dissertation

This dissertation is concerned with the development and application of a simultaneously time- and frequency-resolved coherent anti-Stokes Raman scattering technique that provides sufficient temporal and spectral resolution for high-accuracy thermometry in gas-phase reacting flows. Chapter 2 is a literature review on the development and application of coherent anti-Stokes Raman scattering for high-temperature reacting flows and low-temperature high-pressure flows, including initial work with narrowband nanosecond lasers and recent advances in ultrafast (femtosecond and picosecond) CARS spectroscopy. A detailed theoretical description of the fs/ps CARS process is presented in Chapter 3 along with the development of a spectral fitting algorithm for best-fit thermometry. Chapter 3 ends with a description of the experimental setup of fs/ps

CARS and associated high-temperature, high-pressure hardware used for technique validation. The next five chapters address individual challenges associated with the development and application of fs/ps CARS. Chapter 4 is adapted from the first paper published using this technique for high-temperature gas-phase vibrational thermometry, and includes comparisons to theory, analysis of accuracy and precision as a function of temperature, and high-speed thermometry in a pulsed diffusion flame. Chapter 5 is adapted from a published paper demonstrating temporal suppression of the nonresonant background and details the selection of an optimal time-asymmetric probe shape. Chapter 6 is adapted from the first published work utilizing rotational rather than vibrational transitions in the fs/ps CARS technique. Accurate low-temperature measurements are presented along with the influence and measurement of collision energy transfer on individual *S*-branch rotational transitions. In Chapter 7, interference-free (nonresonant- and collision-free) rotational CARS at pressures up to 15 atm is demonstrated for the first time, adapted from a published paper with a focus on the influence of collision energy transfer on apparent rotational temperature. A time-asymmetric exponential probe pulse is introduced which greatly simplifies the CARS technique utilizing a Fabry–Pérot etalon and requiring no frequency conversion. Chapter 8 is adapted from a published paper demonstrating the advantages of fs/ps CARS for direct measurement of collisional linewidth for individual rotational transitions, and provides the first time-domain measurements of N_2 and O_2 self-broadened *S*-branch linewidths at elevated pressure (> 1 atm). This dissertation concludes in Chapter 9 with a summary of the current work along with a suggested direction for future work in this field.

1.5 References

1. "Annual Energy Review 2010," (U.S. Energy Information Administration, 2011).
2. S. R. Turns, *An introduction to combustion: concepts and applications,* 3rd ed., (McGraw-Hill, Boston, 2011).
3. A. C. Eckbreth, *Laser diagnostics for combustion temperature and species*, (Gordon and Breach Publishers, 1996).
4. S. Roy, J. R. Gord, and A. K. Patnaik, "Recent advances in coherent anti-Stokes Raman scattering spectroscopy: Fundamental developments and applications in reacting flows," *Prog. Energ. Comb.* **36**, 280–306 (2010).
5. D. Pestov, R. K. Murawski, G. O. Ariunbold, X. Wang, M. C. Zhi, A. V. Sokolov, V. A. Sautenkov, Y. V. Rostovtsev, A. Dogariu, Y. Huang, and M. O. Scully, "Optimizing the laser-pulse configuration for coherent Raman spectroscopy," *Science* **316**, 265–268 (2007).
6. D. Pestov, R. K. Murawski, A. Gombojav, X. Wang, M. C. Zhi, A. V. Sokolov, V. A. Sautenkov, Y. V. Rostovtsev, and M. O. Scully, "Hybrid of Frequency and Time Resolved CARS," *2007 Conference on Lasers & Electro-Optics* **1–5**, 1361–1362 (2007).
7. B. D. Prince, A. Chakraborty, B. M. Prince, and H. U. Stauffer, "Development of simultaneous frequency- and time-resolved coherent anti-Stokes Raman scattering for ultrafast detection of molecular Raman spectra," *J. Chem. Phys.* **125**, 044502 (2006).
8. B. D. Prince, "Development and application of a hybrid femtosecond/picosecond coherent Raman probe designed for study of excited state systems," (Iowa State University, 2008).

CHAPTER 2. REVIEW OF LITERATURE

2.1 Introduction

Coherent anti-Stokes Raman scattering (CARS) spectroscopy has been used extensively for investigating combusting temperature and species concentration, and several excellent reviews of the subject can be found in Eckbreth [1] and Roy *et al.* [2]. As enumerated by Roy and outlined previously in this dissertation, four issues have driven the development and application of CARS in reacting flows over the past thirty years: (*i*) the measurement of temperature and concentration of multiple species using one CARS system, (*ii*) the application of traditional CARS systems to challenging reacting flow environments, (*iii*) the suppression of nonresonant background and the analysis of collision energy transfer in CARS measurements at high-pressure, high-temperature conditions, and (*iv*) the measurement of temperature and species concentration at high repetition rates, 1 kHz or higher, to address transient instabilities and phenomena associated with turbulent reacting flows.

Due to the large body of work on CARS imaging in condensed phase matter [3], this literature review will not attempt to provide a complete overview of CARS research. Instead, the focus will remain on the application of CARS spectroscopy for quantitative gas-phase thermometry and species measurements except when condensed phase work is directly applicable. This review begins with an overview of gas-phase CARS spectroscopy focusing on both vibrational and rotational CARS. Initial work using nanosecond sources and recent progress with picosecond and femtosecond lasers is investigated. Innovations for reducing nonresonant background are discussed and studies on the influence of collision energy

transfer and rotation-vibration interactions are reviewed. The review ends with an investigation of recent work in time-resolved CARS in regards to high-speed measurements and suppression of interferences.

2.2 CARS Measurements in Reacting Flows

Coherent anti-Stokes Raman scattering (CARS) spectroscopy was first demonstrated in crystalline and isotropic materials by Maker and Terhune in 1965 [4], although the "CARS" terminology was introduced in 1974 by Begeley *et al.* [5]. Initially, solid-state materials were investigated since the intensity of generated light is highly dependent on density. However, gas-phase concentration measurements were performed using a Q-switched ruby laser in 1974 by Regnier *et al.* [6], and temperature measurements by Moya *et al.* in 1975 [7]. Since these initial experiments, CARS has been used extensively for concentration and temperature measurements in reacting and non-reacting gas-phase flows [1]. Gas-phase CARS spectroscopy is particularly advantageous since small diatomic molecules typically exhibit well-defined vibrational and rotational spectra. In many cases, the transitions are widely separated and easily modeled, leading to highly accurate "calibration-free" temperature measurements analyzed directly from theory. While a detailed review of all gas-phase CARS work can be found elsewhere and will not be repeated here [1, 2], innovations in gas-phase CARS measurements with significance for this work are listed in Table 2.1 on the next page.

Table 2.1. Dates of innovations in CARS spectroscopy with significance for this work

Year	Innovation	Author
1965	First observance of "three-wave mixing"	Maker and Terhune
1974	CARS spectroscopy for gas-phase concentration measurements (H_2)	Regnier *et al.*
1975	CARS spectroscopy for gas-phase temperature measurements (H_2)	Moya *et al.*
1976	Single-shot CARS	Roh *et al.*
1980	Temporal nonresonant suppression using picosecond pulses	Kamga and Sceats
1980	CARS thermometry in a practical combustor (N_2)	Eckbreth
1981	Nonresonant suppression through polarization scheme	Eckbreth and Hall
1985	Dual-broadband multiplexed CARS	Eckbreth and Anderson
1987	Dual-pump CARS for investigation of two species	Eckbreth and Lucht
2001	Time-domain femtosecond CARS thermometry (N_2)	Beaud *et al.*
2002	Single-shot femtosecond CARS	Motzkus and Lang
2003	Triple-pump CARS for temperature and concentration of 3 species (N_2, O_2, and H_2 or CO_2)	Roy *et al.*
2005	Picosecond vibrational CARS thermometry (N_2)	Roy *et al.* and Meyer *et al.*
2006	Hybrid fs/ps CARS in condensed-phase solution	Prince *et al.*
2006	Femtosecond CARS thermometry using frequency-spread dephasing	Lucht *et al.*
2009	1-kHz fs-CARS thermometry	Roy *et al.*
2009	Single-shot multispecies fs-CARS (N_2, CO)	Roy *et al.*
2009	Picosecond rotational CARS thermometry (N_2)	Seeger *et al.*
2010	Temperature and concentration measurements of 6 species using ns CARS (N_2, O_2, H_2, C_2H_4, CO, and	Tedder *et al.*
2010	Direct time-domain Raman linewidth measurements (H_2)	Kulatilaka *et al.*
2011	Femtosecond-CARS line imaging	Kulatilaka *et al.*

2.2.1 Vibrational CARS

Resonant CARS signal is proportional to the population difference between the initial and final state of a Raman transition, such that vibrational transitions primarily occur at elevated temperature where a significant percentage of the ground state population is shifted into the first and second vibrational energy levels. While vibrational CARS (VCARS) thermometry has been demonstrated using many combustion molecules, the most commonly utilized are N_2 [8], O_2 [9], and H_2 [7] due to their significant concentration in air-breathing combustion.

Initial work used narrow-bandwidth ns lasers to probe a single rovibrational transition. By scanning the wavelength of the Stokes or pump pulse, the CARS spectrum was resolved. A broadband approach was quickly introduced by Taran's group to allow single-laser-pulse multiplexed CARS using a broadband Stokes and narrowband pump [10]. In this case, the excitation bandwidth was limited to the bandwidth of the Stokes pulse. The majority of work in VCARS has focused on the simultaneous excitation of all rovibrational transitions for thermometry and has, therefore, utilized the broadband CARS configuration. An additional advantage of this approach is the ability to simultaneously excite multiple molecules. This is typically performed by increasing the width of the Stokes pulse using dye lasers [11] or using broadband pulses for both the pump and Stokes pulses [12] if the transitions are closely spaced, or utilizing multiple pump pulses if they are widely spaced. Seminal work on dual-pump CARS measurements of two species was performed by Lucht [13], while subsequent efforts have sought to increase the number of molecules using up to three pump pulses [9]. Many CARS schemes now use a combination of multiple pump

pulses and broadband Stokes pulses to measure all major species involved in the combustion reaction [14].

In general, vibrational CARS is most accurate at temperatures above 1250 K [15]. Below this temperature, the thermometry accuracy is highly dependent on the rovibrational transitions in the ground vibrational state which are closely spaced and sparsely populated. For this reason, CARS thermometry at low temperature is typically performed using pure rotational transitions in the ground vibrational state using pure-rotational CARS (RCARS).

2.2.2 Rotational CARS

Pure-rotational CARS has been used extensively for low-temperature heat transfer flows [16] and flames [15, 17]. While exhibiting highest accuracy at low temperature, RCARS has been extended to temperatures above 1500 K with great success by detailed investigation of Raman line strengths and linewidths of excited rotational levels [14, 17]. Much of the work in RCARS thermometry has been driven by application to high-pressure systems by T. Seeger and coworkers [18] and high temperature systems by P.-E. Bengtsson and coworkers [14, 17].

At high pressure, the Raman linewidths become broadened and significant error can arise if appropriate values are unknown [18]. This is particularly important when heterogeneous collisions are considered between molecules with large concentrations in the sample volume. Since a primary advantage of RCARS is the simultaneous excitation of multiple molecules, the analysis of these interactions has been studied for many molecules but most notably N_2–O_2 [19]. At high temperature, the effects of excited vibrational states

cause complex vibration–rotation interactions which must be understood for accurate thermometry [17].

2.3 Nanosecond CARS

Initial work in gas-phase CARS thermometry, including that cited in Sections 2.1 and 2.2, was implemented using nanosecond laser sources [8]. These sources were required due to the high peak power necessary to initiate the third-order process. The Nd:YAG laser is most commonly used for this purpose due to high pulse energy (greater than 1 J at 532 nm) and accessibility of laser dyes suitable for 532-nm pumping. Complex arrangements using multiple Nd:YAG and dye laser combinations have been used to excite multiple species [9, 11]; however, the repetition rate of these lasers are typically limited to 10's of Hz which is significantly lower than the frequencies associated with fluid–flame interactions in real-world combustors.

Additionally, nanosecond CARS spectra are highly sensitive to collisions and require complex corrections to Raman linewidths at high pressure [19]. Nonresonant contributions play a major role at both high and low pressure but suppression of this interference is limited to polarization techniques which greatly reduce the resonant signal simultaneously [20, 21]. Additionally, polarization can be rotated as a function of wavelength due to stress-induced birefringence in windowed combustors, limiting the effectiveness of the polarization techniques. Recently, ns-CARS was used to investigate the influence of vibration-rotation interactions on Raman transition line strengths, and therefore temperature, via the Hermann–Wallis Factor. A series of papers by Marrocco have renewed interest in the formulation of

this term and provided corrections for the Raman cross-section of many important molecules in vibrational and rotational CARS thermometry [22-26].

The primary advantage of ns CARS is the ability to spectrally resolve closely-spaced Raman transitions with high pulse energy. Thus, time-domain information is ignored in favor of detailed spectral information. While proven in certain experimental conditions with high accuracy, the lack of high-repetition-rate sources and existence of composition-dependent contributions in complex flows has motivated the replacement of these systems with short-pulsed lasers in the picosecond and femtosecond regimes.

2.4 Picosecond CARS

Picosecond CARS represents a unique compromise between spectral and temporal resolution. For example, nonresonant suppression was demonstrated using picosecond laser pulses by Kamga and Sceats in 1980 [27], where 30-ps pulses from a dye laser were used to suppress nonresonant background 100× by temporal delay of the probe pulse. Quantitative gas-phase thermometry with nonresonant background suppression using ps pulses was later demonstrated by Roy and coworkers [28, 29] using vibrational CARS of N_2. In this case, 100-ps pulses from a modeless dye laser were employed for sufficiently resolved CARS spectra. Pure-rotational ps CARS was subsequently demonstrated by Seeger *et al.* [30] using a similar ps dye laser configuration. In addition to thermometry, this work elucidated the influence of collision energy transfer on temperature [30] and concentration [31] measurement accuracy. In all of these works, a frequency-domain CARS model was used to simulate the spectra. However, since each transition decays with a unique rate constant corresponding to the Raman linewidth, the spectrum appears to shift to higher temperatures

at long delay times [30]. The same trend is seen for species concentration since each molecule decays at a different rate [31]. This necessitates a time- and frequency-dependent model and has not been introduced in previous work.

Recently, the sensitivity to collision energy transfer has been utilized to measure Raman linewidths in the time domain with high accuracy. Linewidth measurements have been demonstrated for H_2 [32] and N_2 [33] using ps sources. Since long delays are easily achieved with ps CARS, the measurement of high-temperature lifetimes with long decay rates are particularly important for validating collision-energy-transfer models at atmospheric pressure.

2.5 Femtosecond CARS

While ns and ps CARS thermometry depends on frequency domain analysis, the broad bandwidth of fs laser pulses requires time-domain analysis of CARS signals. Thermometry using fs CARS was first demonstrated with a regeneratively amplified mode-locked fs laser by Motzkus *et al.* in 1999 [34, 35]. The temperature was derived by fitting long (up to 1 ns) VCARS transients using a phenomenological molecular response. This initiated a significant series of papers on the application of fs CARS to gas-phase diatomic species in flames and at elevated pressure. At the same time, femtosecond degenerate four-wave mixing was used to measure N_2, O_2, and CO_2 rotational transients [36]. Pressure-broadened linewidth models were explored for Q-branch N_2 [37, 38] along with the precise determination of molecular constants [39, 40]. For single-shot thermometry, Lang and Motzkus introduced a unique chirped-probe-pulse (CPP) approach to map multiple

vibrational transients into the frequency domain for spectral detection [41]. In this case, the probe was delayed by ~10 ps to sample highly periodic vibrational recurrences.

Building on this work, S. Roy, J. Gord and co-workers at the Air Force Research Laboratory in collaboration with R. Lucht at Purdue University used the initial decay of the Raman coherence for gas-phase thermometry [42]. Termed frequency-spread dephasing (FSD), as temperature increases and multiple vibrational states become populated, the initial Raman coherence de-phases more rapidly due to increased interference between transitions. An added benefit of using FSD for quantitative thermometry is the ability to sample the molecular response before collision energy transfer becomes important. The broad bandwidth of the 100-fs pump and Stokes pulses can also be used to simultaneously excite N_2 and CO [43] and O_2 and CO_2 [44]. The relative concentration is observed as oscillations in the FSD signal at short delay times. For single-shot measurements, a CPP was implemented in a similar manner to Lang and Motzkus except that the initial FSD was used for thermometry [45]. This was demonstrated using a single laser pulse at 1 kHz resulting in CARS thermometry at kHz rates for the first time. Recently, this technique has been used for temperature measurements along a line to extend the dimensionality of the technique from point to one dimension [46].

2.6 Hybrid Femtosecond/Picosecond CARS

While both fs-CARS and ps-CARS have been used for single-shot thermometry, applications in practical combustion devices are limited. The CPP fs-CARS scheme can be highly sensitive to beam distortion through windowed combustors, while ps-CARS is limited to 10 or 20 Hz measurement rates. A novel approach was proposed by Stauffer *et al.* in 2006

using 100-fs pump and Stokes pulses to induce the Raman coherence of condensed-phase molecules, followed by a frequency-narrowed ps probe pulse [47, 48]. Termed fs/ps CARS, this technique yielded sufficient temporal resolution for suppression of the nonresonant contributions while maintaining sufficient spectral resolution for frequency-domain detection. In 2007, a similar coherent Raman configuration was introduced by Scully *et al.* and used to detect condensed-phase bacteria and explosives [49-51]. This fs/ps configuration has been used extensively in condensed-phase sensing, standoff detection, and CARS microscopy [52-55]. However, only one publication has applied the fs/ps CARS technique to gas-phase sensing, used to measure relative O_2 concentration by Pestov *et al.* in 2008 [56].

A similar approach has been used with ultra-short (7–15 fs) laser pulses for single-beam CARS microscopy by the Silberberg, Motzkus, and Dantus groups [57-59]. Ultra-short ultra-broad fs pulses were used to excite multiple molecules simultaneously over the entire visible spectral region and probed by a shaped ps pulse, all of which are derived from the same laser pulse with a collinear phase-matching geometry. A series of papers from the collaboration of Roy, Gord, and Dantus recently resulted in concentration measurements of CO_2 and N_2 [60, 61]. An additional benefit of single-beam CARS is the ability to control the excitation and suppression of individual vibrational transitions using complex shaping of the pump and Stokes pulses. However, the ability to perform quantitative thermometry using this approach is unknown either due to variations in refractive index or other potential uncertainties in the probe pulse characteristics [62].

2.7 Conclusions

Although CARS thermometry has been demonstrated in many forms over the past forty years, fs/ps CARS is a potential solution to the four challenges outlined in Chapter 1. While the use of fs/ps CARS for condensed-phase sensing is fairly mature, its potential for quantitative gas-phase thermometry is essentially unknown. In general, several questions are important to consider:

(1) Can sufficient spectral resolution be obtained with 1-10 ps transform-limited pulses for accurate quantitative thermometry from vibrational and rotational transitions?

(2) Can sufficient signal be obtained for single-shot high-temperature CARS thermometry at 1 kHz?

(3) Can the molecular response of gas-phase molecules be probed after the decay of nonresonant contributions yet prior to significant collision energy transfer?

(4) Can a quantitative theoretical framework for the time-dependent molecular response be formulated to model the experimental data as a function of temperature and pressure?

In response to these questions, this dissertation presents results from 5 published papers concerned with the development and application of hybrid fs/ps CARS for quantitative vibrational and rotational thermometry in reacting and non-reacting flows.

2.8 References

1. A. C. Eckbreth, *Laser diagnostics for combustion temperature and species*, (Gordon and Breach Publishers, 1996).
2. S. Roy, J. R. Gord, and A. K. Patnaik, "Recent advances in coherent anti-Stokes Raman scattering spectroscopy: Fundamental developments and applications in reacting flows," *Prog. Energ. Comb.* **36**, 280–306 (2010).
3. C. L. Evans and X. S. Xie, "Coherent anti-Stokes Raman scattering microscopy: chemical imaging for biology and medicine," *Annu. Rev. Anal. Chem.* **1**, 883–909 (2008).
4. P. D. Maker and R. W. Terhune, "Study of optical effects due to an induced polarization third order in electric field strength," *Phys. Rev.* **137**, A801 (1965).
5. R. F. Begley, A. B. Harvey, and R. L. Byer, "Coherent anti-Stokes Raman-spectroscopy," *Appl. Phys. Lett.* **25**, 387–390 (1974).
6. P. R. Regnier, F. Moya, and J. P. E. Taran, "Gas concentration measurement by coherent Raman anti-Stokes scattering," *AIAA J.* **12**, 826–831 (1974).
7. F. S. Moya, S. A. J. Druet, and J. P. E. Taran, "Gas spectroscopy and temeprature measurement by coherent Raman anti-Stokes scattering," *Opt. Commun.* **13**, 169–174 (1975).
8. A. C. Eckbreth, "Cars thermometry in practical combustors," *Combust. Flame* **39**, 133–147 (1980).
9. S. Roy, T. R. Meyer, M. S. Brown, V. N. Velur, R. P. Lucht, and J. R. Gord, "Triple-pump coherent anti-Stokes Raman scattering (CARS): temperature and multiple-species concentration measurements in reacting flows," *Opt. Commun.* **224**, 131–137 (2003).
10. W. B. Roh, W. P. Schreiber, and J. P. E. Taran, "Single-pulse coherent anti-Stokes Raman scattering," *Appl. Phys. Lett.* **29**, 174–176 (1976).
11. S. A. Tedder, J. L. Wheeler, A. D. Cutler, and P. M. Danehy, "Width-increased dual-pump enhanced coherent anti-Stokes Raman spectroscopy," *Appl. Opt.* **49**, 1305–1313 (2010).
12. A. C. Eckbreth and T. J. Anderson, "Dual broadband CARS for simultaneous, multiple species measurements," *Appl. Opt.* **24**, 2731–2736 (1985).
13. R. P. Lucht, "Three-laser coherent anti-Stokes Raman scattering measurements of two species," *Opt. Lett.* **12**, 78–80 (1987).
14. S. Roy, T. R. Meyer, R. P. Lucht, M. Afzelius, P. E. Bengtsson, and J. R. Gord, "Dual-pump dual-broadband coherent anti-Stokes Raman scattering in reacting flows," *Opt. Lett.* **29**, 1843–1845 (2004).
15. T. Seeger and A. Leipertz, "Experimental comparison of single-shot broadband vibrational and dual-broadband pure rotational coherent anti-Stokes Raman scattering in hot air," *Appl. Opt.* **35**, 2665–2671 (1996).
16. S. P. Kearney, R. P. Lucht, and A. M. Jacobi, "Temperature measurements in convective heat transfer flows using dual-broadband, pure-rotationl coherent anti-Stokes Raman spectroscopy (CARS)," *Exp. Therm. Fluid Sci.* **19**, 13–26 (1999).
17. L. Martinsson, P. E. Bengtsson, M. Alden, S. Kroll, and J. Bonamy, "A test of different rotational Raman linewidth models: accuracy of rotational coherent anti-Stokes Raman

scattering thermometry in nitrogen from 295 K to 1850 K," *J. Chem. Phys.* **99**, 2466–2477 (1993).
18. T. Seeger, F. Beyrau, A. Brauer, and A. Leipertz, "High-pressure pure rotational CARS: comparison of temperature measurements with O_2, N_2 and synthetic air," *J. Raman Spectrosc.* **34**, 932–939 (2003).
19. M. Afzelius, P. E. Bengtsson, J. Bood, J. Bonamy, F. Chaussard, H. Berger, and T. Dreier, "Dual-broadband rotational CARS modelling of nitrogen at pressures up to 9 MPa. II. Rotational Raman line widths," *Appl. Phys. B* **75**, 771–778 (2002).
20. A. C. Eckbreth and R. J. Hall, "Cars concentration sensitivity with and without non-resonant background suppression," *Combust. Sci. Technol.* **25**, 175–192 (1981).
21. F. Vestin, M. Afzelius, and P. E. Bengtsson, "Development of rotational CARS for combustion diagnostics using a polarization approach," *P. Combust. Inst.* **31**, 833–840 (2007).
22. M. Marrocco, "Reliability of Herman-Wallis factors for Raman spectroscopy of Q-branch molecular transitions," *Chem. Phys. Lett.* **442**, 224–227 (2007).
23. M. Marrocco, "Comparative analysis of Herman-Wallis factors for uses in coherent anti-Stokes Raman spectra of light molecules," *J. Raman Spectrosc.* **40**, 741–747 (2009).
24. M. Marrocco, "Herman-Wallis factor to improve thermometric accuracy of vibrational coherent anti-Stokes Raman spectra of H_2," *P. Combust. Inst.* **32**, 863–870 (2009).
25. M. Marrocco, "CARS thermometry revisited in light of the intramolecular perturbation," *J. Raman Spectrosc.* **41**, 870–874 (2010).
26. A. Bohlin, P.-E. Bengtsson, and M. Marrocco, "On the sensitivity of rotational CARS N_2 thermometry to the Herman–Wallis factor," *J. Raman Spectrosc.* **42**, 1843–1847 (2011).
27. F. M. Kamga and M. G. Sceats, "Pulse-sequenced coherent anti-Stokes Raman scattering spectroscopy: method for suppression of the non-resonant background," *Opt. Lett.* **5**, 126–128 (1980).
28. T. R. Meyer, S. Roy, and J. R. Gord, "Improving signal-to-interference ratio in rich hydrocarbon-air flames using picosecond coherent anti-stokes Raman scattering," *Appl. Spectrosc.* **61**, 1135–1140 (2007).
29. S. Roy, T. R. Meyer, and J. R. Gord, "Time-resolved dynamics of resonant and nonresonant broadband picosecond coherent anti-Stokes Raman scattering signals," *Appl. Phys. Lett.* **87**, 264103 (2005).
30. T. Seeger, J. Kiefer, A. Leipertz, B. D. Patterson, C. J. Kliewer, and T. B. Settersten, "Picosecond time-resolved pure-rotational coherent anti-Stokes Raman spectroscopy for N_2 thermometry," *Opt. Lett.* **34**, 3755–3757 (2009).
31. T. Seeger, J. Kiefer, Y. Gao, B. D. Patterson, C. J. Kliewer, and T. B. Settersten, "Suppression of Raman-resonant interferences in rotational coherent anti-Stokes Raman spectroscopy using time-delayed picosecond probe pulses," *Opt. Lett.* **35**, 2040–2042 (2010).
32. W. D. Kulatilaka, P. S. Hsu, H. U. Stauffer, J. R. Gord, and S. Roy, "Direct measurement of rotationally resolved H_2 Q-branch Raman coherence lifetimes using time-resolved picosecond coherent anti-Stokes Raman scattering," *Appl. Phys. Lett.* **97**, 081112 (2010).

33. C. J. Kliewer, Y. Gao, T. Seeger, J. Kiefer, B. D. Patterson, and T. B. Settersten, "Picosecond time-resolved pure-rotational coherent anti-Stokes Raman spectroscopy in sooting flames," *P. Combust. Inst.* **33**, 831–838 (2011).
34. M. Motzkus, T. Lang, and K. L. Kompa, "Femtosecond CARS on H_2," *Chem. Phys. Lett.* **310**, 65–72 (1999).
35. P. Beaud, H. M. Frey, T. Lang, and M. Motzkus, "Flame thermometry by femtosecond CARS," *Chem. Phys. Lett.* **344**, 407–412 (2001).
36. H. M. Frey, P. Beaud, T. Gerber, B. Mischler, P. P. Radi, and A. P. Tzannis, "Femtosecond nonresonant degenerate four-wave mixing at atmospheric pressure and in a free jet," *Appl. Phys. B* **68**, 735–739 (1999).
37. G. Knopp, P. Beaud, P. Radi, M. Tulej, B. Bougie, D. Cannavo, and T. Gerber, "Pressure-dependent N_2 Q-branch fs-CARS measurements," *J. Raman Spectrosc.* **33**, 861–865 (2002).
38. G. Knopp, P. Radi, M. Tulej, T. Gerber, and P. Beaud, "Collision induced rotational energy transfer probed by time-resolved coherent anti-Stokes Raman scattering," *J. Chem. Phys.* **118**, 8223–8233 (2003).
39. T. Lang and M. Motzkus, "Determination of line shift coefficients with femtosecond time resolved CARS," *J. Raman Spectrosc.* **31**, 65–70 (2000).
40. T. Lang, M. Motzkus, H. M. Frey, and P. Beaud, "High resolution femtosecond coherent anti-Stokes Raman scattering: determination of rotational constants, molecular anharmonicity, collisional line shifts, and temperature," *J. Chem. Phys.* **115**, 5418–5426 (2001).
41. T. Lang and M. Motzkus, "Single-shot femtosecond coherent anti-Stokes Raman-scattering thermometry," *J. Opt. Soc. Am. B* **19**, 340–344 (2002).
42. R. P. Lucht, S. Roy, T. R. Meyer, and J. R. Gord, "Femtosecond coherent anti-Stokes Raman scattering measurement of gas temperatures from frequency-spread dephasing of the Raman coherence," *Appl. Phys. Lett.* **89**, 251112 (2006).
43. S. Roy, D. Richardson, P. J. Kinnius, R. P. Lucht, and J. R. Gord, "Effects of N_2-CO polarization beating on femtosecond coherent anti-Stokes Raman scattering spectroscopy of N_2," *Appl. Phys. Lett.* **94**, 144101 (2009).
44. W. D. Kulatilaka, J. R. Gord, and S. Roy, "Effects of O_2-CO_2 polarization beating on femtosecond coherent anti-Stokes Raman scattering (fs-CARS) spectroscopy of O_2," *Appl. Phys. B* **102**, 141–147 (2011).
45. S. Roy, W. D. Kulatilaka, D. R. Richardson, R. P. Lucht, and J. R. Gord, "Gas-phase single-shot thermometry at 1 kHz using fs-CARS spectroscopy," *Opt. Lett.* **34**, 3857–3859 (2009).
46. W. D. Kulatilaka, H. U. Stauffer, J. R. Gord, and S. Roy, "One-dimensional single-shot thermometry in flames using femtosecond-CARS line imaging," *Opt. Lett.* **36**, 4182–4184 (2011).
47. B. D. Prince, A. Chakraborty, B. M. Prince, and H. U. Stauffer, "Development of simultaneous frequency- and time-resolved coherent anti-Stokes Raman scattering for ultrafast detection of molecular Raman spectra," *J. Chem. Phys.* **125**, 044502 (2006).
48. B. D. Prince, "Development and application of a hybrid femtosecond/picosecond coherent Raman probe designed for study of excited state systems," (Iowa State University, 2008).

49. D. Pestov, R. K. Murawski, G. O. Ariunbold, X. Wang, M. C. Zhi, A. V. Sokolov, V. A. Sautenkov, Y. V. Rostovtsev, A. Dogariu, Y. Huang, and M. O. Scully, "Optimizing the laser-pulse configuration for coherent Raman spectroscopy," *Science* **316**, 265–268 (2007).
50. D. Pestov, R. K. Murawski, A. Gombojav, X. Wang, M. C. Zhi, A. V. Sokolov, V. A. Sautenkov, Y. V. Rostovtsev, and M. O. Scully, "Hybrid of Frequency and Time Resolved CARS," *2007 Conference on Lasers & Electro-Optics* **1–5**, 1361–1362 (2007).
51. D. Pestov, R. K. Murawski, A. Gombojav, X. Wang, M. C. Zhi, A. V. Sokolov, V. A. Sautenkov, Y. V. Rostovtsev, and M. O. Scully, "Detection of B-subtilis spores via Hybrid CARS," *2007 Conference on Lasers & Electro-Optics* **1–5**, 2764–2764 (2007).
52. A. Dogariu, A. Goltsov, D. Pestov, A. V. Sokolov, and M. O. Scully, "Real-time detection of bacterial spores using coherent anti-Stokes Raman spectroscopy," *J. Appl. Phys.* **103**, 036103 (2008).
53. J. H. Peng, D. Pestov, M. O. Scully, and A. V. Sokolov, "Simple setup for hybrid coherent Raman microspectroscopy," *J. Raman Spectrosc.* **40**, 795–799 (2009).
54. D. Pestov, X. Wang, G. O. Ariunbold, R. K. Murawski, V. A. Sautenkov, A. Dogariu, A. V. Sokolov, and M. O. Scully, "Single-shot detection of bacterial endospores via coherent Raman spectroscopy," *P. Natl. Acad. Sci. USA* **105**, 422–427 (2008).
55. S. D. McGrane, R. J. Scharff, M. Greenfield, and D. S. Moore, "Coherent control of multiple vibrational excitations for optimal detection," *New J. Phys.* **11**, 105047 (2009).
56. D. Pestov, X. Wang, D. Cristancho, K. R. Hall, A. V. Sokolov, and M. O. Scully, "Real-Time Sensing of Gas Phase Mixtures via Coherent Raman Spectroscopy," *2008 Conference on Lasers & Electro-Optics* **1–9**, 1471–1472 (2008).
57. T. Polack, D. Oron, and Y. Silberberg, "Control and measurement of a non-resonant Raman wavepacket using a single ultrashort pulse," *Chem. Phys.* **318**, 163–169 (2005).
58. B. von Vacano, W. Wohlleben, and M. Motzkus, "Single-beam CARS spectroscopy applied to low-wavenumber vibrational modes," *J. Raman Spectrosc.* **37**, 404–410 (2006).
59. S. F. Wolf, P. J. Wrzesinski, and M. Dantus, "Standoff Chemical Detection Using Single-Beam CARS," *2009 Conference on Lasers & Electro-Optics* **1–5**, 253–254 (2009).
60. S. Roy, P. Wrzesinski, D. Pestov, T. Gunaratne, M. Dantus, and J. R. Gord, "Single-beam coherent anti-Stokes Raman scattering spectroscopy of N_2 using a shaped 7 fs laser pulse," *Appl. Phys. Lett.* **95**, 074102 (2009).
61. S. Roy, P. J. Wrzesinski, D. Pestov, M. Dantus, and J. R. Gord, "Single-beam coherent anti-Stokes Raman scattering (CARS) spectroscopy of gas-phase CO_2 via phase and polarization shaping of a broadband continuum," *J. Raman Spectrosc.* **41**, 1194–1199 (2010).
62. P. J. Wrzesinski, D. Pestov, V. V. Lozovoy, J. R. Gord, M. Dantus, and S. Roy, "Group-velocity-dispersion measurements of atmospheric and combustion-related gases using an ultrabroadband-laser source," *Opt. Express* **19**, 5163–5171 (2011).

CHAPTER 3. THEORETICAL AND EXPERIMENTAL DESCRIPTION

In this chapter, both the fundamental theory and experimental implementation of the hybrid fs/ps CARS technique are described in detail. Beginning with an introduction to the quantum mechanical nature of molecular motion, the time-resolved Raman response is derived and molecular parameters are described. The chapter ends with a detailed analysis of the experimental setup including pulse-shaping strategies and high-temperature and high-pressure hardware.

3.1 A Quantum-Mechanical Description of Gas-Phase Diatomics

The spectroscopy of gas-phase diatomic species requires an introductory understanding of the quantum mechanical nature of molecular motion described in this section. Whereas efficient absorption-based spectroscopy requires a permanent dipole moment and is typically limited to heterogeneous diatomic species such as NO, OH, and CH, Raman spectroscopies are highly effective for investigations of symmetric stretches or rotational transitions in symmetric molecules such as N_2, O_2, and CO_2 [1]. Therefore, the motion and structure of homogeneous diatomic species are of particular importance in this work.

The Schrödinger Equation describes the fundamental motion of atomic and molecular compounds which is given in the time-independent form

$$-\frac{\hbar^2}{2m}\frac{d^2\psi(x)}{dx^2}+V(x)\psi(x)=E\psi(x) \tag{3.1}$$

where m is the mass of the particle, x is the position of the particle, $\hbar$ is Planck's constant, V is the potential energy field in terms of position, E is the total energy, and ψ is the wave

function which describes the motion of the particle [2]. The Schrödinger Equation is formulated by replacing the wavelength of the wave equation with the de Broglie relationship between the momentum and wave nature of a particle, $\lambda = h/p$. In Eq. 3.1, we can group the wave function operators and define them as the Hamiltonian operator

$$\hat{H} = -\frac{\hbar^2}{2m}\frac{d^2}{dx^2} + V(x) = [KE] + [PE] \tag{3.2}$$

where the first term represents the kinetic energy of the particle and the second term represents the potential energy of the particle. The time-independent Scrödinger Equation can then be rewritten in terms of the Hamiltonian operator

$$\hat{H}\psi_n(x) = E_n\psi_n(x) \tag{3.3}$$

formulated as an eigenvalue problem with operator H, eigenvalues E_n, and eigenfunction $\psi_n(x)$. For the Hamiltonian operator, the eigenvalues represent the total energy of the system with frequency, v, associated with the total energy

$$E = hv \tag{3.4}$$

The normalized wavefunction can be understood in a probabilistic nature where the probability, P, of finding a particle at location x is given by

$$P_n(x) = |\psi_n(x)|^2 \tag{3.5}$$

Additionally, the expectation value of a given property can be determined using the wavefunction probability description. For example, the expectation value of the position, x, is given by

$$\langle x \rangle = \int_0^a \psi_n^*(x)\, x \psi_n(x)\, dx \tag{3.6}$$

where the wavefunction is defined from 0 to a. The probabilistic picture is also significant since effective transitions from one state m to a second state n are a strong function of the overlap of wavefunctions ψ_m and ψ_n.

3.1.1 The Harmonic Oscillator and Rigid Rotor

The time-independent Schrödinger Equation can be used to solve for the energy states of both the rigid rotor and harmonic oscillator approximations for simple diatomic species. In the harmonic oscillator approximation, it is assumed that the two nuclei are connected by a spring with equilibrium length, R, as shown in Fig. 3.1. Assuming a simplified analysis with one shared electron, the total energy of the system can be described in terms of the kinetic energy of the electron, the attractive potential of the electron and positively charged nuclei A and B, and the repulsion potential of A and B. Typically the Born–Oppenheimer Approximation is invoked to discuss molecular motion (translation, vibration, and rotation) since the motion of the electron (~10^{-18} s) is significantly faster than that of the nuclei (10^{-16} – 10^{-11} s) [2, 3]. In this case, we can treat the motion of the molecule using the Born–Oppenheimer Hamiltonian.

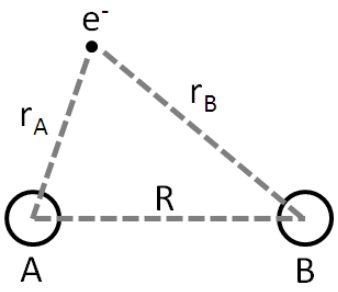

Figure 3.1. Illustration of a simple homogeneous diatomic.

We can assume that the bond acts as a spring with force constant, k, and therefore exhibits a potential energy associated with the vibration of

$$V(x) = \frac{1}{2}k(x - x_o)^2 \tag{3.7}$$

where $x - x_o$ describes the displacement from equilibrium. The harmonic oscillator potential is given as a function of displacement for H_2 in Fig. 3.2 on the next page. We can solve the Schrödinger Equation with the harmonic oscillator potential resulting in energy eigenvalues

$$E_v = hv_o\left(v + \frac{1}{2}\right) \tag{3.8}$$

where v is the vibrational quantum number with integer values (v = 0, 1, 2, 3, …) and v_o is the vibrational frequency

$$v_o = \frac{1}{2}\pi\sqrt{\frac{k}{m}} \tag{3.9}$$

with mass of a single atom, m, in the case of homonuclear diatomic molecules. As indicated by the energy eigenvalues, the harmonic oscillator can occupy only discrete vibrational energy levels associated with the vibrational quantum number. Transitions can occur between these energy levels but must obey the selection rule of $\Delta v = \pm 1$ [2]. This yields constant transition energy for the harmonic oscillator

$$E_{v+1,v} = hv_o \tag{3.10}$$

While the wavefunctions which take on discrete values associated with the vibrational quantum number can be computed either analytically or numerically, these are not explicitly derived in this work and are accounted for using the Plazcek–Teller coefficients as described below.

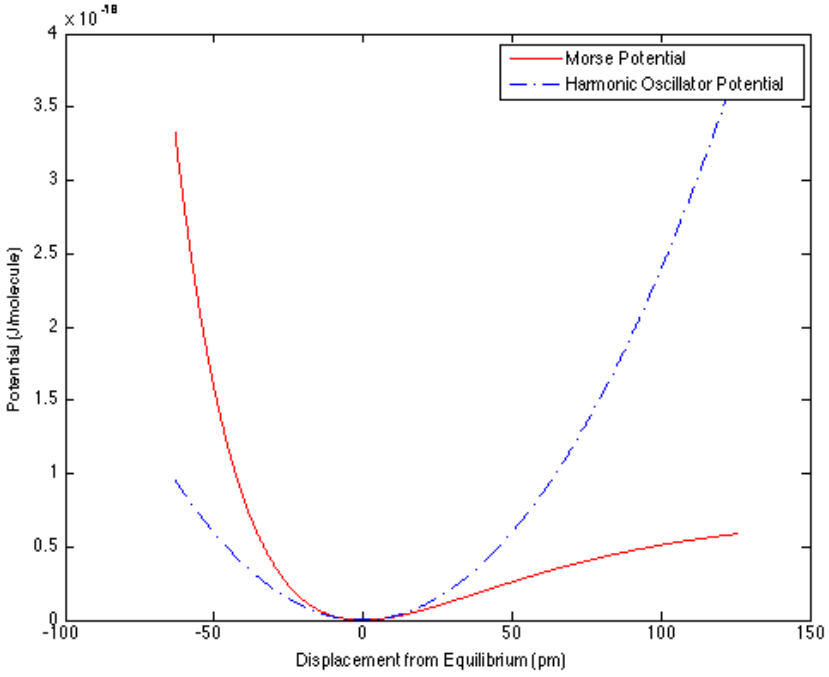

Figure 3.2. Comparison of the harmonic oscillator and an-harmonic Morse potential as a function of displacement for H_2.

In the rigid rotor approximation, the diatomic molecule is considered as two atoms attached via a rigid rod of length R as shown in Fig. 3.1 where vibrations are neglected. In this case, the Schrödinger Equation can be reduced to include only the kinetic energy associated with the rotation of the two nuclei about the center of mass. The center of mass is simply $R/2$ for homonuclear diatomics and the equilibrium distance R_{eq} is assumed ("0" in Fig. 3.2). Solving for the energy eigenvalues yields

$$E_J = B_e J(J+1) \tag{3.11}$$

where J is the rotational quantum number representing the total angular momentum ($J = N+S = 0, 1, 2, 3, \ldots$) comprised of the rotation (N) and spin (S). The rotation constant is defined as

$$B_e = \left(\frac{8}{h\pi^2 m \mathrm{R}_e^2} \right) \tag{3.12}$$

The rotational energy levels are, therefore, also discrete values dependent on the rotational quantum number J. For Raman scattering, the allowed transitions are ΔJ = -2 (O-branch), ΔJ = 0 (Q-branch), and ΔJ = +2 (S-branch). This yields an S-branch transition energy

$$E_{J+2,J} = B_e \left(4J + 6 \right) \tag{3.13}$$

Finally, the total energy of the molecule is determined from the summation of the electronic, vibrational, rotational, and translational energy. If thermodynamic equilibrium is reached in the molecule, macro-scale temperature based on the translational energy is equal to the temperature associated with the rotational and vibrational transitions.

3.1.2 Vibration–Rotation Interaction

As described in the previous section, the rigid rotor produces transition frequencies that are functions of the initial rotational energy state, J. In this case, the purely rotational transitions are well separated. In contrast, the harmonic oscillator produces vibrational transitions that are degenerate and contradict experimental results which show well separated vibrational transitions. The discrepancy between the simplified harmonic oscillator and experimental results is due to vibration–rotation interactions and deviation of the harmonic oscillator from the actual potential, $V(x)$, shown in Eq. 3.7. Vibrations act to vary the distance, R, between the nuclei which is also influenced by the anharmonicity of the potential due to angular momentum.

In general, the harmonic oscillator is a good approximation for small displacements from equilibrium, but better agreement with experiments is achieved using a modified Morse

potential. As shown in Fig. 3.2, the harmonic oscillator and Morse potential are nearly identical at equilibrium but vary dramatically as the displacement is increased. To correct for the vibration–rotation interactions, the vibrational and rotational energy terms are extended using a series expansion

$$E_{v,J} = v_e\left(v+\frac{1}{2}\right) - \chi_e v_e\left(v+\frac{1}{2}\right)^2 + B_v J(J+1) - DJ^2(J+1)^2 \tag{3.14}$$

where v_e is the vibrational constant, χ_e is the anharmonicity constant, B_v is the rotation constant, and D is the centrifugal distortion term. Further expansions can be used to provide higher orders of accuracy as described in the next section [4].

3.2 Hybrid fs/ps Coherent Anti-Stokes Raman Scattering Theory

In this section the time-dependent nature of the fs/ps CARS technique is described in depth including treatment of the time-varying Raman coherence, phenomenological molecular response function, and collision energy transfer.

3.2.1 Ultrafast Pulses and BOXCARS Phase-Matching

One of the primary advantages of using mode-locked ultrafast laser pulses for CARS thermometry is the temporal coherence exhibited by the pulses. Unlike ns sources, the 100-fs laser pulses are generated by actively mode-locking an oscillator with a broad bandwidth such that all frequencies oscillate in phase. This produces a large coherence when the pulses are temporally overlapped and all frequencies are in phase, followed quickly by destructive interference. For a transform-limited pulse, the spectral bandwidth is related to the temporal pulse width through the Fourier Transform where a function is transformed from frequency, ω, to time, t,

$$F(t) = \int_{-\infty}^{\infty} f(\omega)\exp[-2\pi i\omega t]d\omega \tag{3.15}$$

where $f(\omega)$ is the spectral pulse shape, $F(t)$ is the transform limited temporal pulse shape, and the integration is performed over the entire frequency domain. For transform-limited pulses, the time-bandwidth product, $TBP = \Delta t\Delta\omega$, can be computed for different pulse shapes as given in Table 3.1 [5]. For example, a Gaussian pulse shape with 100-fs temporal bandwidth exhibits a spectral bandwidth of 146.7 cm^{-1}.

Table 3.1. Time-bandwidth product for common pulse shapes

Pulse Shape	TBP	Δt (fs)	Δω (cm^{-1})
Gaussian	0.44	100	146.7
$Sinc^2$	0.88	100	293.3

While broad spectral bandwidths can be produced using modeless dye lasers with custom dye mixtures [6], the advantage of using transform limited pulse shapes is the coherent and impulsive interaction with the molecules [7]. Since all frequencies coherently interact with the molecule over a very short temporal duration, multiple photon pairs within the ~150-cm^{-1} bandwidth can combine to provide a significant increase in excitation efficiency over broadband ns and ps sources.

The CARS process is a four-wave mixing technique that utilizes three input pulses (E_1, E_2, and E_3) which must obey the conservation of energy and momentum in the generation of a fourth laser-like pulse. Each pulse can be described as a time-dependent electric field

$$E_i(\vec{r},t) = E_i(t)\exp\left[i\vec{k}\vec{r} - i\omega t\right] \tag{3.16}$$

where $\boldsymbol{k}$ is the wave vector along the propagation direction $\boldsymbol{r}$, ω is the frequency, and $E(t)$ is the pulse envelope of the electric field [5]. The frequency of the generated radiation, ω_4, is constrained by the conservation of energy

$$\omega_4 = \omega_1 - \omega_2 + \omega_3 \tag{3.17}$$

where a large increase in signal is observed if ω_1 - ω_2 is resonant with a vibrational or rotational transition in a sample molecule. When the energy difference of the four-wave mixing signal is generated at the positive anti-Stokes wavelength, the technique is considered coherent anti-Stokes Raman scattering (CARS) and the individual pulses are termed pump, Stokes, probe, and CARS respectively. The phase matching of the four-wave mixing process is constrained by the conservation of momentum

$$\vec{k}_4 = \vec{k}_1 - \vec{k}_2 + \vec{k}_3 \tag{3.18}$$

While several phase-matching configurations are possible, including collinear arrangements, many suffer from insufficient spatial resolution at the intersection point. As a result, the folded BOXCARS phase-matching configuration, illustrated in Fig. 3.3 on the next page, has become a frequently used scheme with the advantages of enhanced spatial resolution at the measurement volume and adequate spatial offset in the generated signal to allow filtering of the four-wave mixing signal from the input pulses [8].

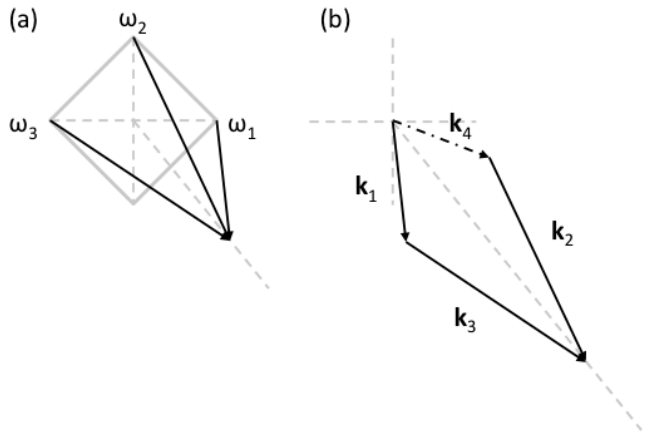

Figure 3.3. Schematic of (a) the BOXCARS phase-matching configuration, and (b) the resultant wave vector, $\mathbf{k}_4$, from the conservation of momentum.

3.2.2 CARS Intensity

The intensity of the CARS signal, I_{CARS}, is of primary interest in this dissertation and is described by

$$I_{CARS}(t,\tau_{12},\tau_{23}) \propto \left| P_{res}^{(3)}(t,\tau_{12},\tau_{23}) + P_{NR}^{(3)}(t,\tau_{12},\tau_{23}) \right|^2 \tag{3.19}$$

where $P_{res}^{(3)}$ and $P_{NR}^{(3)}$ are the resonant and nonresonant third-order polarizations written as functions of time, t, and the temporal spacing between the pump and Stokes pulses, τ_{12}, and Stokes and probe pulses, τ_{23}. The total polarization is described in terms of the third-order susceptibility of the molecule, $\chi^{(3)}$,

$$P^{(3)} \propto \chi^{(3)} E_1(t) E_2(t) E_3(t) \tag{3.20}$$

such that the CARS signal intensity is proportional to $I_1 I_2 I_3$. The third-order dependence on laser intensity leads to signal generation which is orders of magnitude larger than linear spectroscopies such as fluorescence and spontaneous Raman scattering [1]. This occurs

since transitions between energy states are induced coherently by the pump and Stokes pulses, in contrast to spontaneous Raman scattering which relies on low-probability transitions.

As given in Eq. 3.19, the third-order polarization has both a resonant and nonresonant component. The resonant component describes transitions within the molecule due to interaction with the pump and Stokes pulses and is a strong function of molecular parameters and thermodynamic properties such as pressure and temperature. In contrast, the nonresonant contribution is derived from interactions with the electrons of any molecule in the sample and variations in the frequency ordering of the four-wave mixing process. For instance, Fig. 3.4 displays energy diagrams for the resonant contribution and two different nonresonant schemes for vibrational CARS [9].

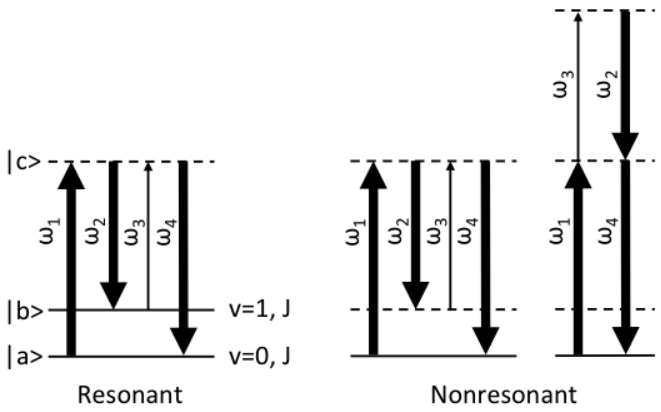

Figure 3.4. Resonant and nonresonant energy diagrams for vibrational CARS. The dashed lines represent virtual states while the solid lines represent resonant eigenstates. The letters correspond to molecular eigenstates. Two pulse orderings are shown for the nonresonant contribution.

3.2.3 Time-Resolved Treatment of the Third-Order Polarization

For most diatomic species of interest in combustion, the rotational and vibrational transition frequencies have characteristic oscillations of several picoseconds. Since the

duration of the pump and Stokes pulse is 100 fs and less than 10 ps for the probe, the pulse order and Raman coherence must be treated in a time-dependent manner. In general, the Raman coherence consists of an ensemble of rotors or vibrational oscillators impulsively excited by the pump–Stokes interaction which evolve in time as a rotational or vibrational wavepacket. The evolution of the wavepacket is described in terms of the time-dependent third-order polarization.

The nonresonant component of the third-order polarization is highly dependent on interactions from all three pulses and de-phases rapidly [9, 10]. As such, the nonresonant contribution is only significant during the overlap of the pump, Stokes, and probe pulses. To maximize excitation of the Raman coherence, the pump–Stokes delay is minimized, $\tau_{12} = 0$. In this case, the time-dependent third-order polarization is given by [5, 11, 12]

$$P^{(3)}(t,\tau_{23}) = \left(\frac{i}{\hbar}\right)^3 \int_0^\infty dt_3 \int_0^\infty dt_2 \int_0^\infty dt_1 \Big[R(t_3,t_2,t_1) E_3(t-t_3) e^{i(\omega_1-\omega_2+\omega_3)t_3} \times E_2^*(t+\tau_{23}-t_3-t_2) e^{i(\omega_1-\omega_2)t_2} E_1(t+\tau_{23}-t_3-t_2-t_1) e^{i\omega_1 t_1} \Big] \tag{3.21}$$

where t_1, t_2, and t_3 are the coherence time scales during the pump–Stokes, Stokes–probe, and probe–CARS interactions respectively, R is the molecular response function, E_1, E_2, and E_3 are the electric field envelopes, and ω_1, ω_2, and ω_3 are the frequencies of the pump, Stokes, and probe electric fields. The spatial component of the electric field is accounted for in the phase-matching configuration and not explicitly stated in Eq. 3.21. For purely nonresonant contributions, the molecular response function can be replaced by $\delta(t_3)\delta(t_2)\delta(t_1)$ since the dephasing rates of the electronic interactions are much faster than the resonant molecular response [13]. Applying the relationship

$$\int_{-\infty}^{\infty} f(t)\delta(t)dt = f(0) \tag{3.22}$$

results in a simplified form of the nonresonant contribution to the third-order polarization

$$P_{NR}^{(3)}(t,\tau_{23}) = \left(\frac{i}{\hbar}\right)^3 E_3(t)E_2^*(t+\tau_{23})E_1(t+\tau_{23}) \tag{3.23}$$

When the pump and Stokes pulses are of equal duration (100 fs) and much shorter than the duration of the probe pulse, the nonresonant contribution is essentially a cross-correlation allowing the characteristics of the probe pulse to be determined as a function of τ_{23} if the pump and Stokes characteristics are known. It should be noted, as was first demonstrated by Kamga and Sceats [10], that for $\tau_{23} >> E_{3,\,FWHM}$ the value of $P_{NR}^{(3)}$ approaches zero; and, therefore, the nonresonant component can be completely neglected. The regions for which this is a valid assumption will be further discussed in Chapter 5 for various pulse shapes, $E_3(t)$. However, when nonresonant contributions are significant, they must be modeled in quadrature ($\pi/2$ phase shift) with the resonant contribution [14].

Unlike the nonresonant contribution, the resonant molecular response is long lived for diatomic gas-phase species and is described by a phenomenological molecular response function, R. As shown in Fig 3.4 where a, b, and c are molecular eigenstates, during the first coherence timescale, t_1, the molecule undergoes pure ket transitions from initial state |a><a| to |c><a|. The ket evolution is understood in terms of the density matrix where |c><a| represents the probability that an ensemble of states |c> collapse into states <a| [15]. After excitation to the virtual state |c> which undergoes extremely fast dephasing such that it only exists during the duration of the pulses, the pure ket evolution continues from |c><a| to |b><a| during the second coherent timescale, t_2, and from |b><a| to |c><a| during the third coherence

timescale, t_3. During the final interaction, the molecule is returned to the initial |a><a| eigenstate.

Since the ket state |c> is a virtual state that is short lived, the molecular response during the first and third coherence timescales can be replaced with a delta function such that the molecular response function becomes $\delta(t_3)R(t_2)\delta(t_3)$ and the resonant third-order polarization is given by

$$P_{res}^{(3)}(t,\tau_{23}) = \left(\frac{i}{\hbar}\right)^3 \int_0^\infty dt_3 \int_0^\infty dt_2 \int_0^\infty dt_1 \left[\delta(t_3) R(t_2) \delta(t_1) E_3(t-t_3) e^{i(\omega_1-\omega_2+\omega_3)t_3} \times E_2^*(t+\tau_{23}-t_3-t_2) e^{i(\omega_1-\omega_2)t_2} E_1(t+\tau_{23}-t_3-t_2-t_1) e^{i\omega_1 t_1}\right] \tag{3.24}$$

where $R(t_2)$ is molecule specific and described in section 3.2.4. Applying the delta function during the first coherence timescale

$$P_{res}^{(3)}(t,\tau_{23}) = \left(\frac{i}{\hbar}\right)^3 \int_0^\infty dt_3 \int_0^\infty dt_2 \left[\delta(t_3) R(t_2) E_3(t-t_3) e^{i(\omega_1-\omega_2+\omega_3)t_3} \times E_2^*(t+\tau_{23}-t_3-t_2) e^{i(\omega_1-\omega_2)t_2} E_1(t+\tau_{23}-t_3-t_2)\right] \tag{3.25}$$

and during the third coherence timescale,

$$P_{res}^{(3)}(t,\tau_{23}) = \left(\frac{i}{\hbar}\right)^3 \int_0^\infty dt_2 \left[R(t_2) E_3(t) E_2^*(t+\tau_{23}-t_2) e^{i(\omega_1-\omega_2)t_2} E_1(t+\tau_{23}-t_2)\right] \tag{3.26}$$

the third-order resonant polarization can be rearranged in an intuitive manner as [11]

$$P_{res}^{(3)}(t,\tau_{23}) = \left(\frac{i}{\hbar}\right)^3 E_3(t) \int_0^\infty dt_2 \left[R(t_2) E_2^*(t+\tau_{23}-t_2) E_1(t+\tau_{23}-t_2) e^{i(\omega_1-\omega_2)t_2}\right] \tag{3.27}$$

Phenomenologically, the complex exponential term represents the phase and frequency associated with each resonant Raman transition, the $E_2^* E_1$ product is the spectral convolution of the pump and Stokes pulses during impulsive excitation, and the real part of the integral is

the temporal convolution of the pump–Stokes product with the molecular response. In general, the convolution of two functions $(f*g)(t)$ is defined as

$$(f*g)(t)=\int_{-\infty}^{\infty} f(\tau)g(t-\tau)d\tau \tag{3.28}$$

where f can be replaced by the molecular response function in Eq. 3.27, g with the pump–Stokes product, and τ with the second coherence timescale, t_2. If the pump, Stokes, and probe electric fields are well known and nonresonant contributions can be neglected, the temporal and spectral CARS signal, respectively, can be theoretically given by

$$I_{CARS}(t,\tau_{23})=\left|\left(\frac{i}{\hbar}\right)^3 E_3(t)\int_0^{\infty} dt_2\left[R(t_2)E_2^*(t+\tau_{23}-t_2)E_1(t+\tau_{23}-t_2)e^{i(\omega_1-\omega_2)t_2}\right]\right|^2 \tag{3.29}$$

$$\begin{aligned} I_{CARS}(\omega,\tau_{23})=\Bigg|F_t\Bigg\{\left(\frac{i}{\hbar}\right)^3 E_3(t)\int_0^{\infty} dt_2\Big[R(t_2)E_2^*(t+\tau_{23}-t_2)\times \\ E_1(t+\tau_{23}-t_2)e^{i(\omega_1-\omega_2)t_2}\Big]\Bigg\}(\omega)\Bigg|^2 \end{aligned} \tag{3.30}$$

3.2.4 The Molecular Response Function

Paramount to the fs/ps CARS process is the phenomenological treatment of the molecular response function, R, which includes the summation of all Raman-active transitions from initial state m to final state n [12],

$$R(t)=\sum_{n,m} I_{n,m}\exp\left[-i\omega_{n,m}t-\Gamma_{n,m}t\right] \tag{3.31}$$

with Raman transition strength $I_{n,m}$, transition frequency $\omega_{n,m}$, and transition linewidth $\Gamma_{n,m}$. The formulation of these terms differs for pure rotational and ro-vibrational transitions and each term is species specific.

3.2.4.1 Transition Frequency

The rotational and vibrational energy level, $E_{v,J}$, of a molecule in the v^{th} vibrational and J^{th} rotational state is determined from the Born-Oppenheimer approximation as described previously [16],

$$E_{v,J} = T_e + hc\omega_e\left(v+\frac{1}{2}\right) - hc\omega_e\chi_e\left(v+\frac{1}{2}\right)^2 + hc\omega_e y_e\left(v+\frac{1}{2}\right)^3 - hc\omega_e z_e\left(v+\frac{1}{2}\right)^4 + F(J) \tag{3.32}$$

$$F(J) = hc\left[B_e - \alpha_e\left(v+\frac{1}{2}\right) + \gamma_e\left(v+\frac{1}{2}\right)^2\right]J(J+1) - hc\left[D_e - \beta_e\left(v+\frac{1}{2}\right) + \delta_e\left(v+\frac{1}{2}\right)^2\right]J^2(J+1)^2 \tag{3.33}$$

where T_e is the minimum potential energy of the electronic state and is assumed to be zero for the ground electronic state (J) [2], h is Planck's constant (Js), c is the speed of light in a vacuum (cm/s), ω_e is the fundamental vibrational frequency of the oscillator (cm^{-1}), v is the vibrational quantum number, χ_e, y_e, and z_e are higher-order anharmonicity factors which account for unequal spacing of the vibrational states, and $F(J)$ is the rotational energy term. The two terms in $F(J)$ are the vibration-rotation interaction and the centrifugal distortion constant where B_e, α_e, γ_e, D_e, and β_e are standard Herzberg molecular parameters (cm^{-1}) [4]. In the current work, the Herzberg molecular constants are taken from the CARSFT spectroscopic code in order to conform to standards established by the community and listed in Table 3.2 [17].

Table 3.2. Molecular constants for rotational and vibrational CARS

Term	N_2 (vib)	N_2 (rot)	O_2 (rot)
T_e (J)	0	0	0
ω_e (cm^{-1})	2360	2360	1580
χ_e	14.3	14.3	11.98
y_e	–0.0059	–0.0059	0.0475
z_e	–2.4E-4	–2.4E-4	1.2E-5
B_e (cm^{-1})	2	2	1.4456
α_e (cm^{-1})	0.0173	0.0173	0.0159
γ_e (cm^{-1})	–3.15E-5	–3.15E-5	0
D_e (cm^{-1})	5.77E-6	5.77E-6	0
β_e (cm^{-1})	1.55E-8	1.55E-8	0
δ_e (cm^{-1})	0	0	0
m_n	1	1	0
g_J (even)	6	6	0
g_J (odd)	3	3	1
R_o (Å)	2.07	2.07	2.289
γ' (10^{-24} cm^3)	0.6775	0.6775	1.0724
a' (10^{-24} cm^3)	0.5810	0	0
m (amu)	28	28	32

The quantized energy eigenvalues are easily computed as a function of vibrational and rotational quantum numbers with v = 0, 1, 2, 3 … and J = 0, 1, 2, 3, … At flame temperatures up to 2500 K, vibrational states up to v = 4 and rotational states up to J = 70 are calculated. The transition frequency is governed by selection rules for the transitions of

states as given in Table 3.3 for both vibrational and rotational CARS. The transition frequency (cm^{-1}) is calculated from the energy difference between the two states

$$\omega_{n,m} = \frac{2\pi}{hc}\left(E_n - E_m\right) \tag{3.34}$$

Table 3.3. Raman selection rules

Transition	Δv	ΔJ	Branch
Vibrational	±1	0	Q
Rotational	0	+2	S
Rotational	0	–2	O

3.2.4.2 Transition Strength and Boltzmann Distribution of Energy States

Each Raman transition in the molecular response has an associated Raman transition strength dictated by the Franck-Condon principle. The Franck-Condon principle states that the strength of a given transition is proportional to the overlap of the ground and excited state molecular wavefunctions. The Raman transition strength, $I_{n,m}$, is given as a function of the population difference $\rho_m - \rho_n$, and the Raman cross section, $(\partial\sigma/\partial\Omega)_J$ [18-20].

$$I_{n,m} \propto \left(\frac{\partial\sigma}{\partial\Omega}\right)_J \Delta\rho_{n,m}(T) \tag{3.35}$$

The population distribution is a strong function of temperature described by the Boltzmann distribution [2]. The percentage of the total population in a single state, m, is given as an explicit function of temperature, T (K),

$$\rho_m = \frac{N_m}{N_{tot}} = \frac{g_m \exp\left[\frac{-E_m}{k_B T}\right]}{Z(T)} \tag{3.36}$$

$$Z(T) = \sum_m g_m \exp\left[\frac{-E_m}{k_B T}\right] \tag{3.37}$$

where $g_m = 2J+1$ is the degeneracy of the energy state, E_m is the energy as determined from Eqs. 3.32 and 3.33 (J), k_B is the Boltzmann constant (J/K), and $Z(T)$ is the partition function. The partition function is a normalizing factor for the Boltzmann distribution and is the sum of the population in all possible states. At a temperature of 2400 K, the first four vibrational and seventy rotational energy states include >99.2% of all populated states. The distribution of population among the vibrational and rotational energy states is given in Fig. 3.5 for N_2 at 2400 K highlighting the ability to neglect contributions from $v \geq 5$ and $J \geq 71$ energy states under typical combustion conditions.

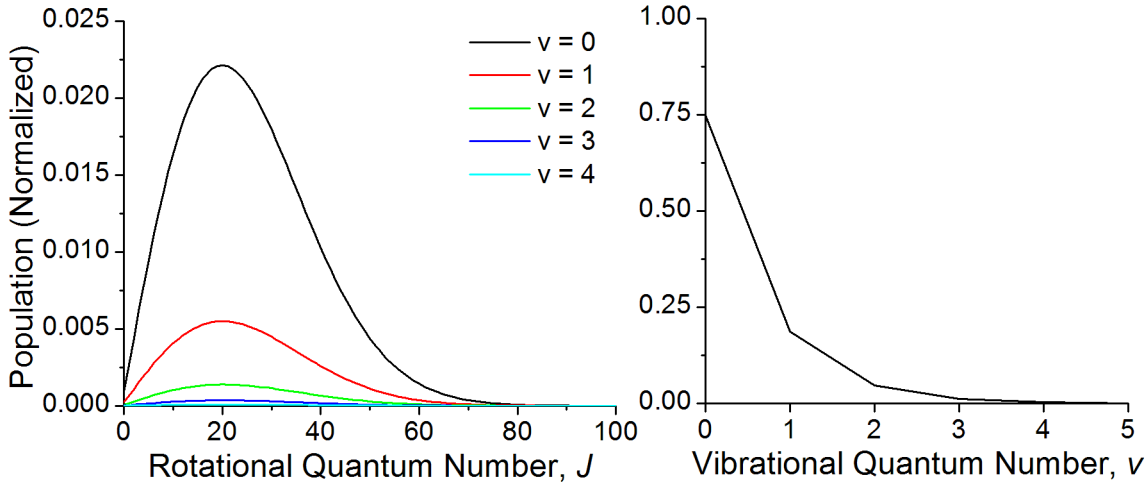

Figure 3.5. Population distribution for N_2 at 2400 K as a function of rotational and vibrational energy state.

Using Eq. 3.36, the population difference can be computed as [21]

$$\Delta\rho_{n,m} = \frac{g_J(2J+1)}{Z(T)}\left[\exp\left(\frac{-E_m}{k_B T}\right) - \exp\left(\frac{-E_n}{k_B T}\right)\right] \tag{3.38}$$

where the rotational-nuclear degeneracy, g_J, is included explicitly [22]. For a homonuclear diatomic with even mass number such as N_2 and O_2, the total wavefunction must be symmetric with respect to permutations in the nuclei. For N_2 with a symmetric electronic wavefunction and nuclear spin of $m_n = 1$, the rotational-nuclear degeneracy is given as

$$g_J = \left[\frac{g_m\left(g_m+1\right)}{2}\right]_{J=even} \tag{3.39}$$

$$g_J = \left[\frac{g_m\left(g_m-1\right)}{2}\right]_{J=odd} \tag{3.40}$$

where $g_m = 2m_n+1$ is the spin degeneracy. For N_2 this yields $g_m = 3$ and $g_J = 6$ for even J and $g_J = 3$ for odd J. This results in a 2:1 intensity ratio for the even to odd line strengths. For O_2 with nuclear spin $m_n = 0$, the electronic wavefunction is asymmetric and requires rotational-nuclear degeneracy [23]

$$g_J = \left[\frac{g_m\left(g_m-1\right)}{2}\right]_{J=even} \tag{3.41}$$

$$g_J = \left[\frac{g_m\left(g_m+1\right)}{2}\right]_{J=odd} \tag{3.42}$$

where $g_m = 1$ such that $g_J = 0$ for even J and $g_J = 1$ for odd J. This leads to the absence of even rotational transitions for O_2.

The Raman scattering cross section differs for rotational and vibrational transitions and must be computed independently for the Q, S, and O branches. For S-branch rotational transitions, the cross section is proportional to [19, 21]

$$\left(\frac{\partial\sigma}{\partial\Omega}\right)_J \propto \frac{4}{45} b_{J,J+2}\left(\gamma'\right)^2 F_{rot}\left(J\right) \tag{3.43}$$

where $b_{J+2,J}$ is the Placzek–Teller coefficient, γ'^2 is the polarization anisotropy, and $F_{rot}(J)$ is the Herman–Wallis factor. The Placzek–Teller coefficient represents the wavefunction overlap of the initial and final state and depends on J number and rotational transition [1]

$$b_{J,J} = \frac{J(J+1)}{(2J-1)(2J+3)}, \quad \text{Q-Branch} \tag{3.44}$$

$$b_{J+2,J} = \frac{(3J+1)(J+2)}{2(2J+1)(2J+3)}, \quad \text{S-Branch} \tag{3.45}$$

$$b_{J-2,J} = \frac{3J(J-1)}{2(2J+1)(2J-1)}, \quad \text{O-Branch} \tag{3.46}$$

The Herman–Wallis factor is a correction term for vibration–rotation interaction. For *S*-branch rotational transitions, it is not significant; however, the formulation of Tipping and Ogilvie [18] is used in this work

$$F_{rot}(J) = \left[1 + \frac{p_1}{p_0}\left(\frac{2B_e}{\omega_e}\right)^2 \left(J^2 + 3J + 3\right)\right]^2 \tag{3.47}$$

where p_1 and p_0 are the first two coefficients of the anisotropic polarizability expansion with values listed in Table 3.4 [18, 24].

Table 3.4. Values for *S*-branch Herman–Wallis factors

Molecule	B_e (cm^{-1})	ω_e (cm^{-1})	(p_1/p_0)
N_2	2.00	2360	3.168
O_2	1.4456	1580	4.348

For *Q*-branch vibrational CARS, the Raman cross section is given by

$$\left(\frac{\partial\sigma}{\partial\Omega}\right)_J \propto (v+1)\left[a'^2 F_a(J) + \frac{4}{45} b_{J,J}\gamma'^2 F_\gamma(J)\right] \tag{3.48}$$

where *a'* is the polarization isotropy with associated Herman–Wallis factor $F_a(J)$, $b_{J,J}$ is the *Q*-branch Placzek-Teller coefficient, and γ' is the polarization anisotropy with associated Herman–Wallis factor, $F_\gamma(J)$ [25]. Although many works consider $F_a(J) = F_\gamma(J) = 1$, recent work by Marrocco has shown that this factor influences vibrational CARS thermometry significantly. The Herman–Wallis factor has been formulated by Tipping and Bouanich [25] as

$$F_i(J) = 1 - \left[\frac{3}{2}(a_1 + 1) - 4\left(\frac{p_2}{p_1}\right)_i\right]\left(\frac{2B_e}{\omega_e}\right)^2 J(J+1) \tag{3.49}$$

where *i* is equal to *a* or γ for the isotropic or anisotropic Herman–Wallis factors respectively. The first Durham coefficient, a_1, is constant for both terms, and p_2 and p_1 are coefficients of the polarizability expansion. These values are taken from Marrocco [25] and listed in Table 3.5.

Table 3.5. Values for *Q*-branch Herman–Wallis factors

Molecule	B_e (cm^{-1})	ω_e (cm^{-1})	a_1	$(p_2/p_1)_a$	$(p_2/p_1)_\gamma$
N_2	2.00	2360	–2.7	0.31	0.57
O_2	1.4456	1580	–3.0	0.96	1.22

3.2.4.3 Transition Linewidth

The final term in the molecular response function (Eq. 3.31) is the Raman linewidth. The linewidth is a function of both Doppler-broadened and *J*-dependent collision-broadened terms where the total linewidth is defined as

$$\Gamma_J = \Gamma_{Doppler,J} + \Gamma_{Collision,J} \tag{3.50}$$

Doppler broadening originates from the distribution of translational energy of an ensemble of particles and the direction of the motion. Scatter from particles moving towards the detector is positively Doppler shifted, while scatter from particles moving away from the detector is negatively Doppler shifted. As such, it is highly temperature dependent as shown in Eq. 3.51. The purely Doppler broadened linewidth results in a Gaussian lineshape with a full-width at half-maximum (FWHM) of [22]

$$\Gamma_{Doppler,J} = \frac{2}{c}\left[2\ln(2)\frac{k_B T}{m_{mol}}\right]^{0.5}\frac{E_n - E_m}{hc} \tag{3.51}$$

where c is the speed of light (m/s), k_B is the Boltzmann constant (J/K), T is the temperature (K), m_{mol} is the molecular mass (kg), and E is the energy (J) associated with the initial, m, and final, n, states. At atmospheric pressure, most molecules exhibit significant collision linewidth broadening and the Doppler broadened contribution can be ignored. For instance, for N_2 at 1 atm and 300 K the ratio between the Doppler and S-branch (J = 8) collision-broadened linewidth terms, $(\Gamma_{Doppler}/\Gamma_{Collision})_{J=8}$ = 2.7E-5, such that the Doppler contribution is <0.005% of the total linewidth and can be neglected.

The collision-broadened term occurs as a result of energy transfer induced by inelastic collisions between molecules. Because the energy gaps between adjacent vibrational states and electronic states are large, the collision energy transfer is primarily rotational. There are various ways to model the rate of rotational energy transfer, although the most common model is the energy band gap model [26]. In general, the collision-broadened term is computed as [27],

$$\Gamma_{Collision,J} = P\sum_i 2\gamma_J^i \tag{3.52}$$

where γ_J is the half-width of the J-dependent collisional broadening coefficient (cm^{-1}/atm) of the probed species with species i, and P is the pressure (atm). The linewidth term causes an exponential decay in the intensity of a specific transition, initial state J, which is species specific as shown in Fig. 7.1.

As shown in Eq. 3.53, the total linewidth is a function of interactions between the measured species and all other species in the measurement volume. For example, in air the linewidth term is primarily comprised of N_2–N_2 and N_2–O_2 broadening terms for N_2. While the composition of air is well known, in practical combustion systems, the local species concentration may not be known and assumptions must be made based on expected concentrations. Additionally, in turbulent flames, the sample composition can change rapidly between single-laser-shot measurements so time-averaged assumptions may not capture the actual local composition. As a result, the ability to ignore collision line broadening allows the linewidth to be computed easily and without a detailed understanding of the colliding species. The ability to ignore composition-dependent error (including nonresonant contributions) is termed interference-free CARS in this work.

With the recent availability of ultrafast lasers, the ability to ignore the collision-broadening component by probing the system before it interacts with other molecules has been the focus of investigation. The collision-free assumption has been proposed stating that $\Gamma_{Collision}$ can be ignored at short times. However, these time scales have not been quantified outside of our own work in Chapter 7. For example, at standard temperature and pressure (298 K and 1 atm), it has been found that the influence of the $\Gamma_{Collision}$ term on fs/ps CARS signals can be neglected for times less than 25 ps [28]; however, it is obvious from Fig. 7.1 that collisions occur during that time frame. Hence, it is clear that the error term is not

primarily dependent on the number of collisions but on the degree to which the relative collisional dephasing rates of the rotational transitions, $\Delta\Gamma_{Collision}$, perturb the Boltzmann distribution. While the influence of collisions can be neglected for most implementations of fs/ps CARS by selection of an appropriately short probe delay, extreme situations (low temperature and high pressure) require the calculation of the collision linewidth. Nonetheless, the use of fs/ps CARS can greatly reduce the sensitivity to collisions with other species by detection at short delay times (as short as 300 fs). In this case, self-broadened (N_2–N_2 and O_2–O_2) linewidths may be used to estimate the rate of collisions with a mixture of unknown composition. Based on the extensive use of energy band gap laws for computing linewidth [1, 26, 29, 30], the modified exponential gap (MEG) model is used to compute self-broadened linewidths when necessary for fs/ps CARS.

3.2.5 Modified Exponential Gap (MEG) Model for Raman Linewidth

The modified exponential gap model (MEG) is used to determine the collision-broadened Raman linewidth based on the work of Rahn and Palmer [26] as restated by Seeger *et al.* [29]. The rate of transition upwards from states i to j ($i < j$) is given by

$$\gamma_{ji} = \alpha P F(T) \left(\frac{T}{T_o}\right)^n \left(\frac{1+\dfrac{aE_i}{k_B T\delta}}{1+\dfrac{aE_i}{k_B T}}\right)^2 \exp\left[\frac{-\beta E_{ij}}{k_B T}\right] \tag{3.53}$$

$$F(T) = \frac{1-\exp[-m]}{1-\exp\left[\dfrac{-mT}{T_o}\right]}, \quad \text{for } N_2 - N_2 \tag{3.54}$$

$$F(T) = 1, \quad \text{for } O_2 - O_2 \tag{3.55}$$

where P is pressure (atm), T is temperature (K) with reference temperature T_o = 295 K, E_i is the rotational energy (J) [31] of initial state i, E_{ij} is the energy difference, $E_j - E_i$ (J), between rotational states i and j (positive value since $i < j$), k_B is the Boltzmann constant (J/K), and α, β, δ, a, m, and n are fitting parameters found in Rahn [26] and Seeger [29] and given in Table 3.6. It should be noted that E_{ij} represents the energy gap between any two states, and the rate of transitions, γ_{ji}, is proportional to $\exp[-E_{ij}]$ meaning that the rate of transition upward decreases with increasing energy gap. The transition rate downward from state j to i is given by microscopic reversibility as

$$\gamma_{ij} = \frac{2J_i + 1}{2J_j + 1} \gamma_{ji} \exp\left[\frac{E_{ij}}{k_B T}\right] \tag{3.56}$$

where γ_{ji} is previously determined. The rate of transition downwards is proportional to $\exp[-E_{ij}]$ which increases proportionally with energy gap although it is balanced by γ_{ji}. The total transition rate matrix can be separated into two parts: an upper triangle, γ_{ij}, which corresponds to transitions downward from all states $J(j)$ (column) to states less than J(j) (row), and a lower triangle, γ_{ji}, which corresponds to transitions upward from state $J(i)$ (column) to all states greater than $J(i)$ (row). The diagonal elements, $i = j$, of the matrix are zero since there can be no transitions within the same rotational state. Thus the total matrix, $\gamma_{kj} = \gamma_{ji} + \gamma_{ij}$, includes all transition rates for the transfer of energy from state j to states k, greater and less than j. This is illustrated in Fig. 3.6 where the transition rate matrix is given for N_2–N_2 collisions at 1000 K and 1 atm. The columns represent the initial state J and the rows represent the rate of transitions to the final state $J \pm \Delta J$. For low-rotational states, the rate of transition upwards is greater than downwards since the most populated state from the Boltzmann distribution is $J = 13$. Above this, the rate of transition downwards is greater.

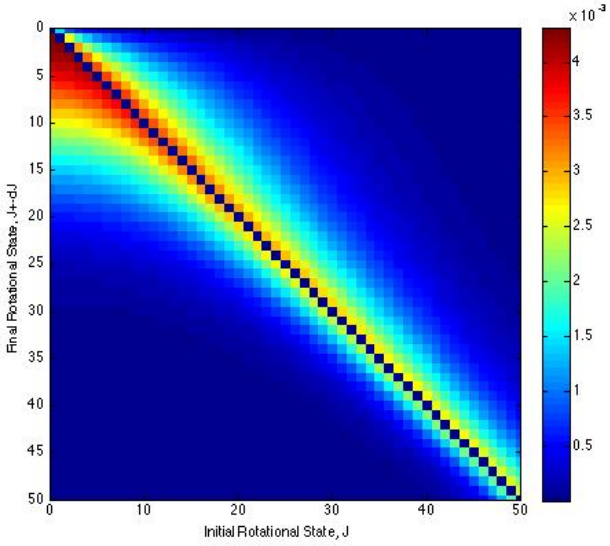

Figure 3.6. Rate of transition from initial (abscissa) to final (ordinate) rotational state for N_2–N_2 collisions at 100 K and 1 atm.

A summation of each column in Fig. 3.6 gives the total rate of collision energy transfer from state $J(j)$, both upwards and downwards on the rotational energy ladder, such that

$$\Gamma_{J,J} = \Gamma_J = \sum_{k \neq j} \gamma_{kj} \tag{3.57}$$

where $\Gamma_{J,J}$ is the collision-broadened Q-branch linewidth ($\Delta J = 0$) as a function of rotational quantum number $J(j)$. The S-branch linewidth ($\Delta J = +2$) can be approximated as the average of the Q-branch linewidths at J and $J + 2$ as [31]

$$\Gamma_{J+2,J} = \frac{1}{2}\left(\Gamma_{J,J} + \Gamma_{J+2,J+2}\right) \tag{3.58}$$

where collisions which change the direction, but not magnitude, of the angular momentum are neglected. $\Gamma_{J+2,J+2}$ is simply the value of $\Gamma_{J,J}$ with the J values shifted by 2. The Q-branch linewidths as calculated in this dissertation using the parameters in Table 3.6 are

compared to experimental results from Rahn and Palmer [26] and Millot *et al.* [23] in Fig. 3.7 and with our own time-domain measurements [32] in Fig. 9.2.

It is interesting to note that the linewidth decreases with increasing temperature (in contrast to the direct relationship with increasing pressure), and high-rotational states have smaller linewidths than low-rotational states. This is primarily due to the increase in energy gap at high-rotational states. At high temperature, the linewidth becomes nearly uniform

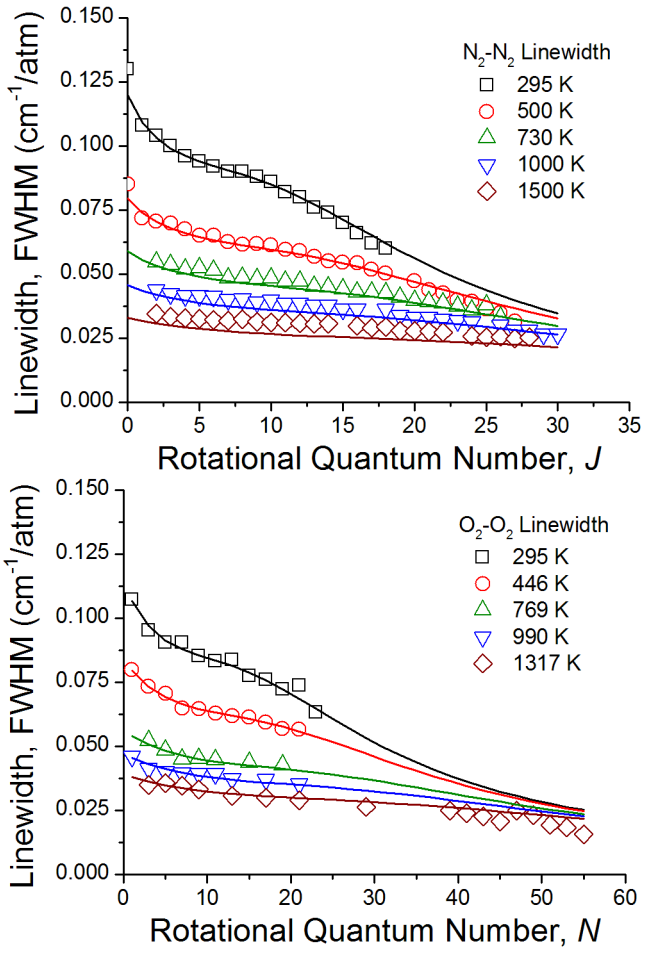

Figure 3.7. Experimental (symbols) from Ref. [23, 26] and calculated (line) self-broadened linewidths for N_2 and O_2 at atmospheric pressure. The linewidths are calculated using the MEG model as described in this dissertation.

across all rotational states. This feature will be considered in Chapter 7 and plays a crucial role in the influence of collisions on accurate thermometry for interference-free CARS.

Table 3.6. MEG fitting parameters from Rahn and Palmer [26] and Seeger *et al.* [29]

Parameter	N_2–N_2	O_2–O_2
α*	0.020	0.0146
β	1.67	1.45
δ	1.21	1.32
a	1.5	1.5
m	0.148	0
n	0.5	1.32

*Modified from [26] to match experimental data

3.3 Spectral Simulation

The numerical evaluation of Eq. 3.30 is performed in Matlab to compute the spectral CARS intensity as a function of probe delay, τ_{23}, and molecular response function, R. In this section, the "HyCARS" code is used to aid in a physical understanding of the hybrid fs/ps CARS process. This section concludes with a description of the fitting routine used for hybrid fs/ps CARS thermometry.

3.3.1 Physical Description of fs/ps CARS using the HyCARS Code

The equations in Section 3.2 can be modeled using the HyCARS code to yield increased understanding about the fs/ps CARS process. In particular, Eq. 3.30 can be better understood in terms of its components. Because the nonresonant contribution is temporally suppressed in all experimental cases, only the resonant polarization (Eq. 3.27) will be considered here. For fs/ps RCARS, the molecular preparation and molecular response

function are shown for N_2 (top) and O_2 (bottom) at 300 K and 1 atm in Fig. 3.8 on the next page. The green solid line is the temporal product of the pump and Stokes electric field envelopes, $E_1E_2^*$, which represents the spectral convolution of the pump and Stokes bandwidths. A unique property of the Fourier Transform is that the convolution (*) in the original domain is equal to multiplication (×) in the Fourier transformed domain

$$f(t) * g(t) = F(\omega) \times G(\omega) \tag{3.59}$$

Thus for temporal convolution of the molecular response function with the pump–Stokes product (red line), the convolution is performed using a Fourier transformation to the frequency domain, multiplying the two terms, and performing an inverse Fourier transformation to return to the time domain. This is particularly useful in the context of numerical calculations where the Fast Fourier Transform (FFT) is significantly faster than the convolution function.

The red line is the absolute value of the molecular response function representing the total magnitude (recurrence) of the ensemble of rotors (wavepacket), while the black line is the real part of the molecular response function representing the accumulated phase of the rotational wavepacket. For N_2, the intensity variation in the major and minor recurrences is due to the nuclear spin degeneracy which is different for even and odd transitions. The full recurrence, as observed in the phase, occurs at 8.392 ps and is $\sim[2cB_e]^{-1}$ = 8.33 ps. For O_2, only major recurrences are observed since only odd transitions are present. The full recurrence occurs at 11.59 ps and is $\sim[2cB_e]^{-1}$ = 11.53 ps.

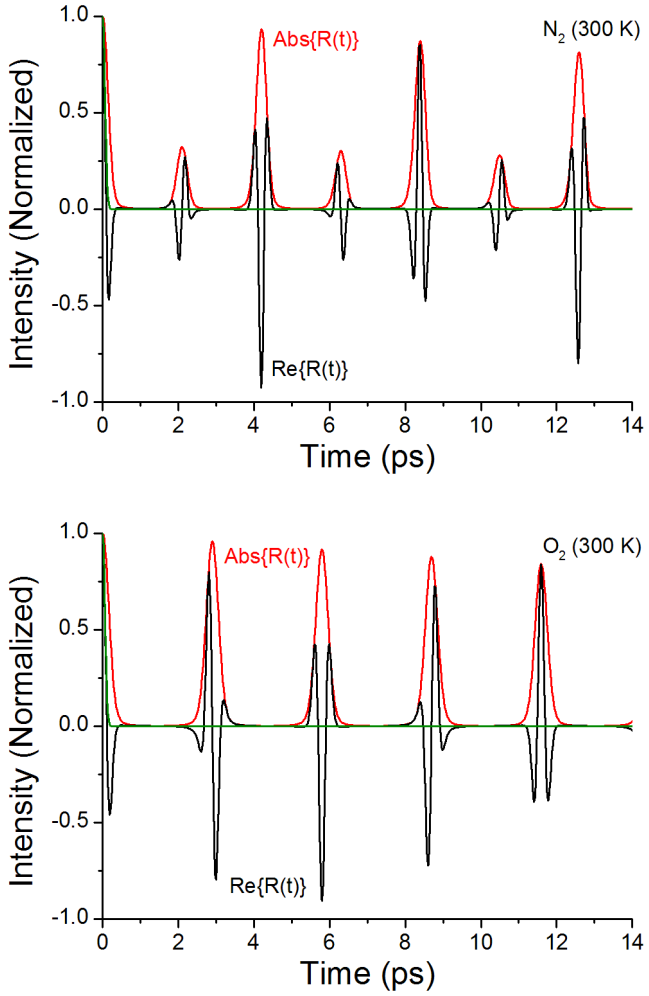

Figure 3.8. Pump–Stokes preparation (green) and rotational molecular response for N_2 (top) and O_2 (bottom) at 1 atm and 300 K. The solid red line represents the total magnitude of the rotor alignment while the solid black line represents the total acquired phase of the rotors.

The real part of the exponential molecular response can be neglected using the collision-free assumption by simply setting the linewidth term, $\Gamma = 0$. The complete (top) and collision-free (bottom) molecular response of N_2 at 300 K and 1 atm is shown in Fig. 3.9. The collision linewidth produces a nearly exponential decay in the molecular response which is a strong function of pressure. However, when the linewidth term is neglected there is still

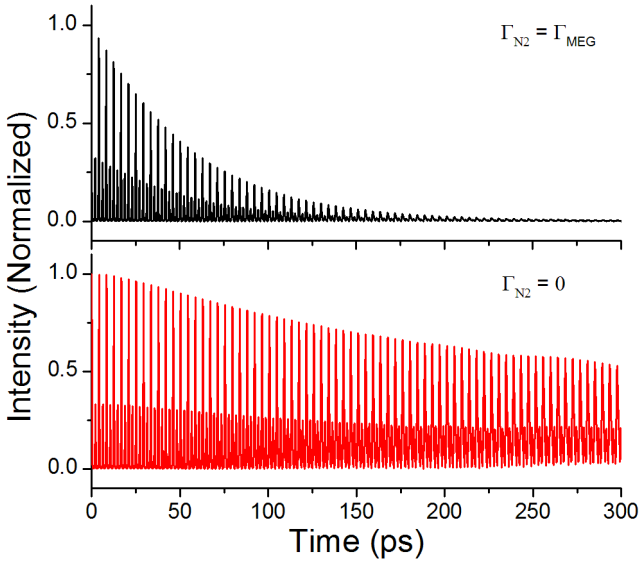

Figure 3.9. Molecular response, Abs[$R(t)$], of N_2 at 300 K and 1 atm with (top) and without (bottom) collisional linewidths.

a slow dephasing that is due to higher-order corrections for vibration–rotation interactions. This occurs at significantly longer times than are typically probed using fs/ps RCARS.

As is seen in Eq. 3.27, the probe pulse is simply multiplied by the molecular response in the time domain to generate the time-dependent third-order polarization. An 8.41-ps FWHM Gaussian probe pulse with 13.5-ps delay is shown in Fig. 3.10 along with the time-dependent third-order polarization for N_2. Fourier transformation of this signal and the multiplication by its complex conjugate produce the familiar frequency domain CARS signal. Both N_2 and O_2 fs/ps RCARS spectra are given in Fig. 3.11 at 300 K and 1 atm.

Vibrational fs/ps CARS exhibits dramatically different behavior from rotational fs/ps CARS and thus warrants its own investigation. Unlike the well resolved recurrent features associated with fs/ps RCARS, the vibrational wavepacket dephases rapidly due to frequency-spread dephasing [33] as shown in Fig. 3.12 (top) for N_2 at 1 atm and 300, 1000, 1500, and

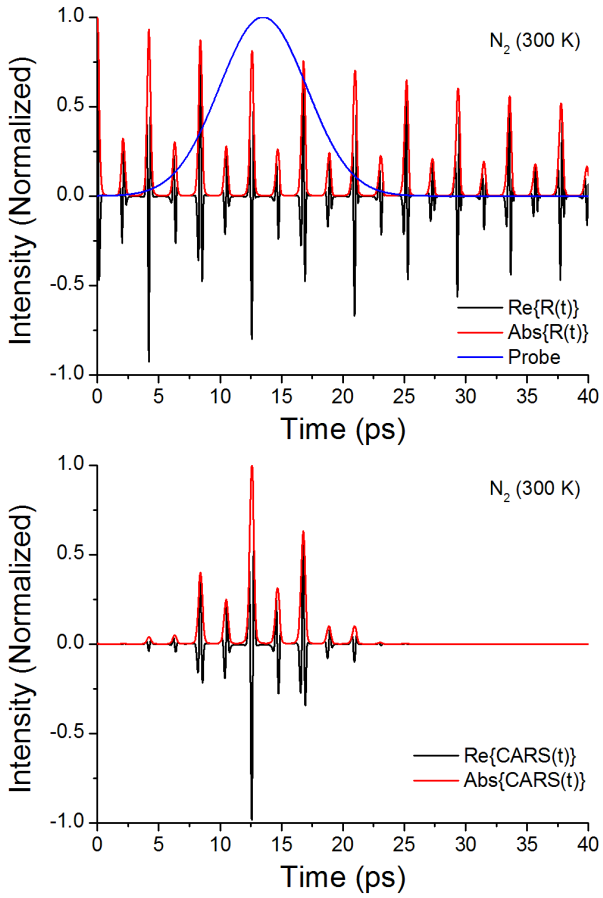

Figure 3.10. (top) Probe pulse with 8.41-ps duration (FWHM) and 13.5-ps delay to minimize nonresonant contributions. (bottom) Time-dependent third-order polarization.

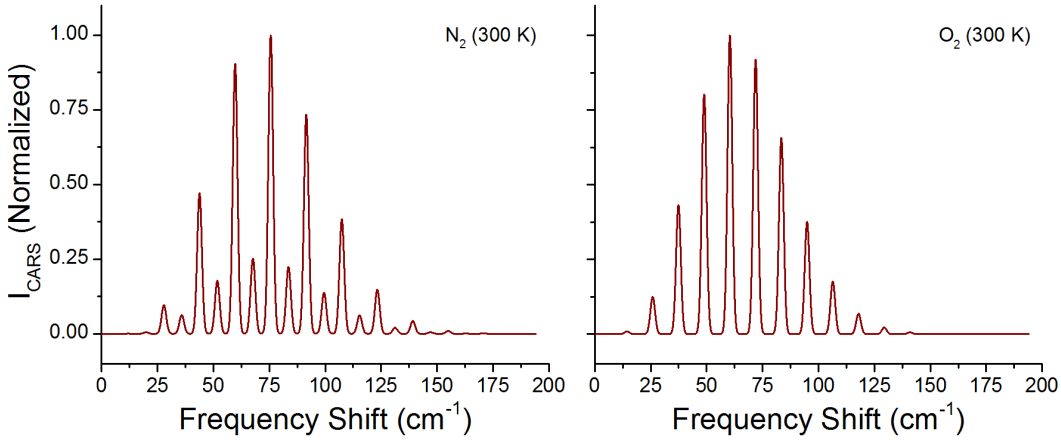

Figure 3.11. N_2 (left) and O_2 (right) fs/ps RCARS spectra at 1 atm, 300 K, and a delay of 13.5 ps.

2300 K. This initial decay results from destructive interference between the excited transitions. Since these are non-uniformly spaced transitions unlike fs/ps RCARS, the decay is slower than RCARS and increases as temperature increases due to the broadened distribution of populated energy states. The oscillations in the initial decay represent the frequency difference between the excited vibrational states; and, it is this feature that allows sensitive spectral thermometry during the initial decay. At low temperature, there is little spectral information in the frequency-spread dephasing and the application of fs/ps VCARS may be limited. However, after the initial frequency-spread dephasing complicated recurrent

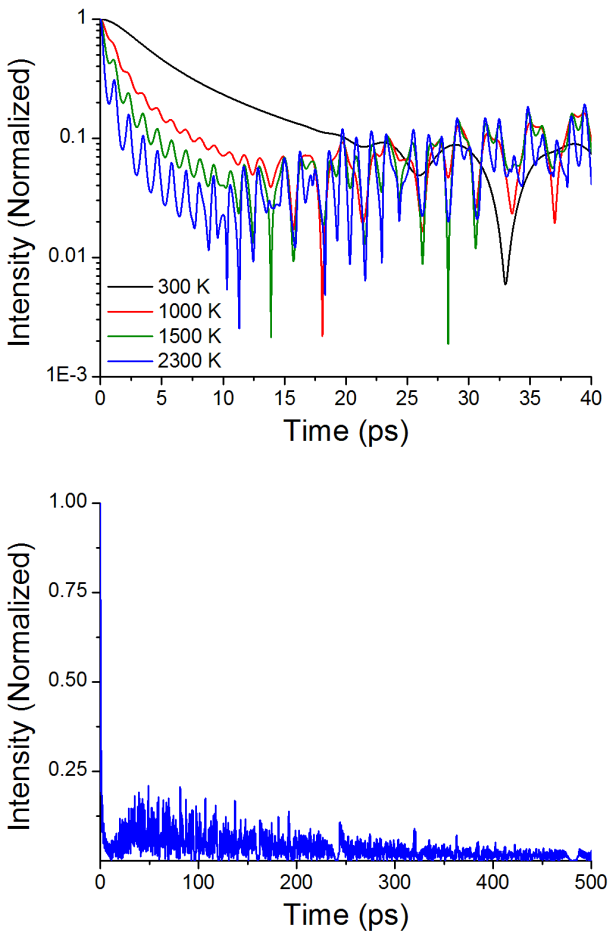

Figure 3.12. Molecular response for N_2 at 1 atm and 300, 1000, 1500, and 2300 K during frequency spread dephasing (top) and at longer times (bottom).

features are observed which may allow sensitive thermometry even at low temperature. Unfortunately, these decay in a nearly exponential fashion due to collision energy transfer as shown for 2300 K in Fig. 3.12 (bottom) making collision-free measurements impractical.

If collisions are neglected ($\Gamma_{Collisions} = 0$), then the molecular response is long lasting. Unlike the molecular response at low temperature, the decreased linewidths at high temperature and the linewidth uniformity greatly reduce the sensitivity to collision energy transfer at short times. The complete and collision-free molecular response for N_2 at 2300 K is given in Fig. 3.13. At short times there is little difference between the responses (bottom) and the ability to perform interference-free measurements using fs/ps VCARS should be possible even at high pressure.

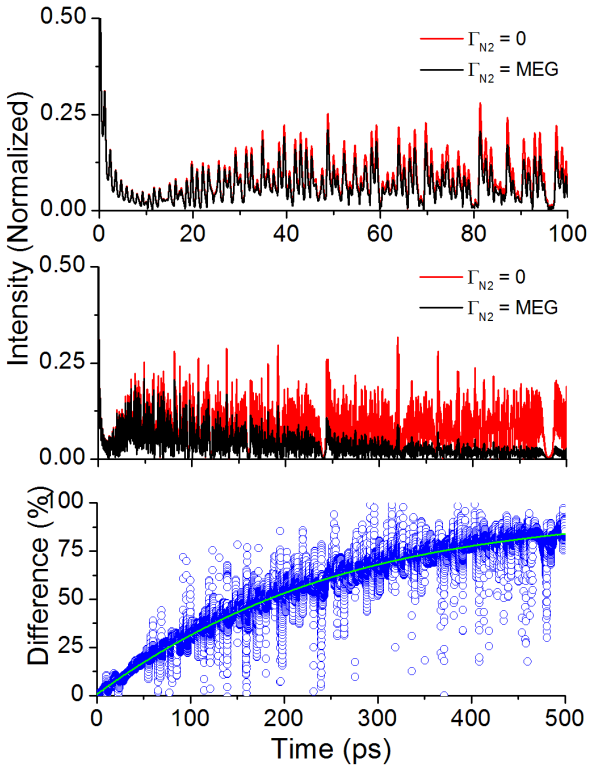

Figure 3.13. Molecular response of N_2 with and without collisions. Both frequency-spread dephasing (top) and collisional dephasing (middle) timescales are shown. The difference (bottom) highlights the ability to make collision-free measurements at short times.

The molecular response is sampled by the probe pulse with a familiar $sinc^2$ shape (from the rectangular slit in the 4-*f* pulse shaper explained elsewhere). In this simulation, a 12-cm^{-1} probe is employed with a delay of 2.36 ps in order to emulate experimental conditions [14]. Fig. 3.14 displays the probe and generated time-dependent third-order polarization. As stated above, the oscillations sampled by the probe allow for simple frequency domain thermometry as shown in Fig. 3.15, which displays the CARS spectra under the given conditions.

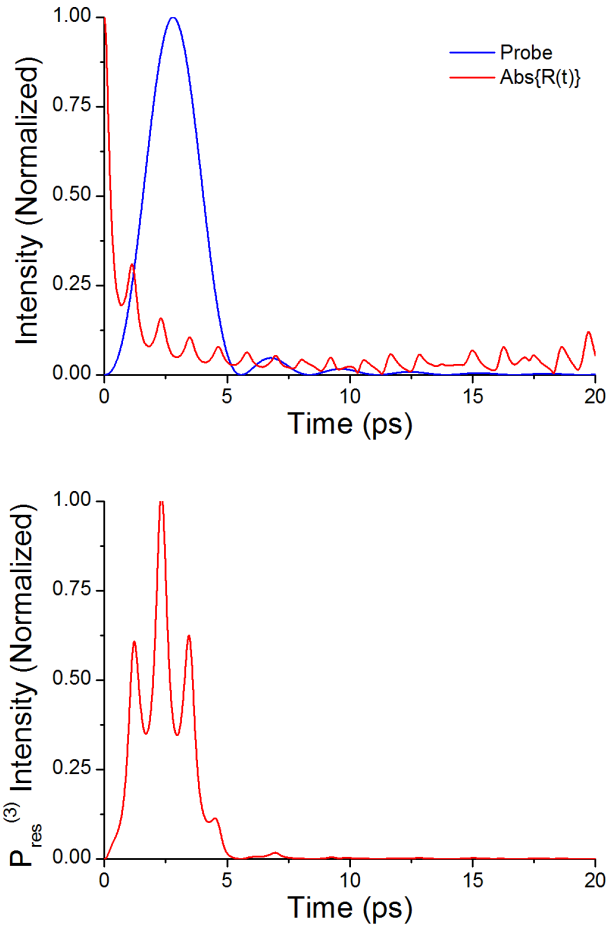

Figure 3.14. Probe interaction with the molecular response (top) and the generated third-order polarization (bottom) at 2300 K.

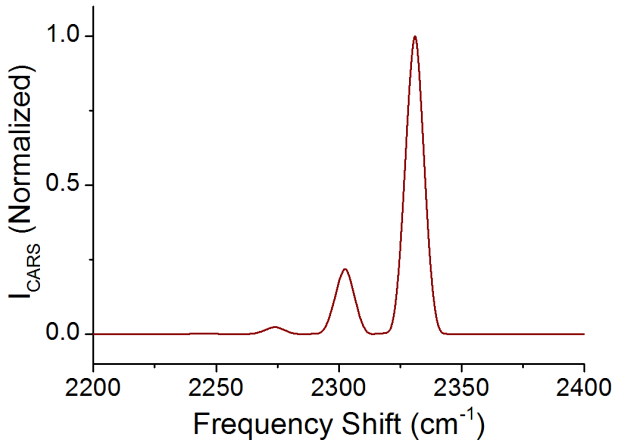

Figure 3.15. Frequency-domain N_2 fs/ps VCARS spectra at 2300 K and 1 atm.

In addition to generating CARS spectra at a single probe delay, the probe delay can be changed to create a time- and frequency-resolved spectrograph. While this is not necessary for single-shot thermometry, analysis of the temporal and spectral dependence of

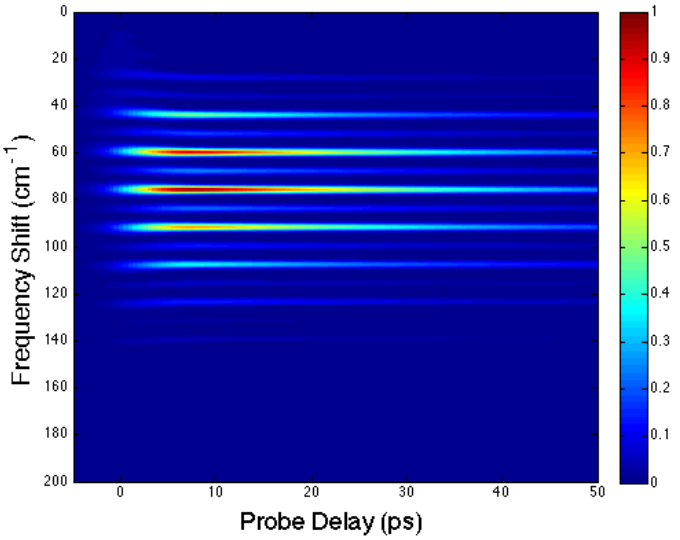

Figure 3.16. Spectrograph of N_2 fs/ps RCARS (I_{CARS}) at 300 K with an 8.41-ps Gaussian probe pulse.

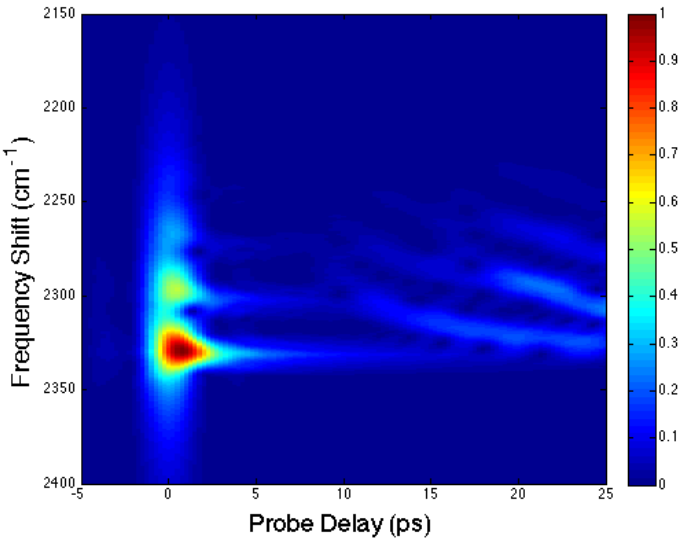

Figure 3.17. Spectrograph of N_2 fs/ps VCARS (sqrt[I_{CARS}]) at 2300 K with a 12-cm^{-1} sinc^2 probe pulse.

the CARS signal may be advantageous for measuring collisional properties such as Raman linewidth as discussed in Chapter 9. Fig. 3.16 and Fig. 3.17 display spectrographs of N_2 fs/ps RCARS at 300 K and N_2 fs/ps VCARS at 2300 K respectively.

3.3.2 Fitting Routine for fs/ps CARS Thermometry

The theoretical CARS spectrum can be computed using the HyCARS model as a function of temperature (T), pressure (P), species (χ_i), and probe pulse characteristics (E_3). While this is the first step in fs/ps CARS thermometry, the theoretical spectra must be accurately fit to the experimental spectra in order to perform high-accuracy thermometry. In general, the process is given in Fig. 3.18 along with the names of specific Matlab files used in the process and included in the Appendix.

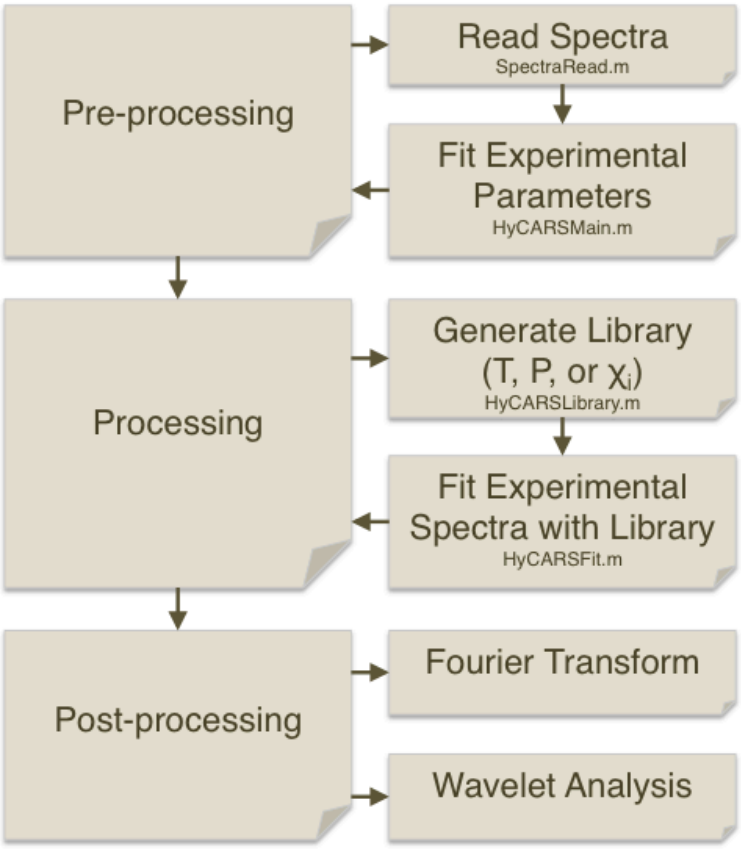

Figure 3.18. Processing flowchart for fs/ps CARS thermometry.

In the pre-processing steps, an average spectrum obtained under known conditions is read into the Matlab program. Using the HyCARS code, the experimental parameters are determined based on the known thermodynamic parameters (T, P, and χ_i) and probe delay, τ_{23}. These parameters primarily consist of the bandwidth and shape of the pump–Stokes interaction and probe pulse. For fs/ps RCARS, the pump–Stokes interaction is determined by fitting the spectra at room temperature where the nonresonant background is suppressed. For fs/ps VCARS, the pump–Stokes interaction is determined by fitting the spectral shape of the nonresonant contribution at time τ_{23} = 0 ps and room temperature. In both cases, the

probe pulse shape is determined by fitting the temporal profile of the nonresonant signal since this interaction is simply a cross-correlation of the pump–Stokes and probe pulses.

Once the experimental parameters are determined, the HyCARS code is used to generate a library of spectra with independent thermodynamic variables. Although only one variable can be changed in the current code (temperature), extension to two or three variables is straightforward. The library is generated in increments of 1 K, and the spectra, $I_{CARS}(T)$, are compared to experimental spectra using the Differential Evolution (DE) algorithm [34]. Differential Evolution is a robust global optimization algorithm which can be used to determine a minimum solution for a series of variables. In this case, the residual between the theoretical spectra at temperature, T, and the experimental spectrum is computed and minimized using DE. In DE, a random population of 20 theoretical spectra are chosen and compared to the experimental spectrum. The fittest member, the spectrum with the lowest residual, is chosen as the parent of the next generation of 20 spectra. These spectra are then compared to the experimental spectrum and the fittest theoretical spectrum survives. This continues for 100 generations producing a theoretical spectrum that is the best-fit solution to the experimental spectrum. The temperature used to simulate the best-fit theoretical spectrum is recorded as the best-fit temperature. This is performed rapidly and 1000 spectra can be fit in ~10 seconds using a 2.8 GHz Intel Core i7 with 4 GB 1333 MHz DDR3 memory on a MacBook Pro running Mac OS X (10.7.3) and Matlab R2011b.

For single-shot thermometry performed at 1 kHz (1 ms between measurements), the best-fit temperature vector can be used to determine linear or non-linear spectral characteristics of the investigated flow. For instance, a Fourier Transformation of the series produces information on dominant frequencies associated with the temperature fluctuations,

while non-linear methods such as wavelet analysis provide temporally-localized information of the dominant frequencies. While beyond the scope of this dissertation, such statistical methods are available and applicable within the limits of the thermometry measurements presented in Chapter 4.

3.4 CARS Experimental Description

This section describes the experimental details of the ultrafast laser source, optical layout for fs/ps CARS, and the hardware used for high-temperature and high-pressure validation experiments.

3.4.1 Ultrafast Laser Source

In fs/ps CARS, a 2.5-W regeneratively-amplified ultrafast laser (Solstice, Spectra Physics) is used to provide 2.5 mJ per pulse at 1 kHz with a nominal pulse width of 100 fs FWHM. The central output wavelength is tunable from ~790–800 nm. The Solstice is a one-box amplified system consisting of an oscillator (MaiTai, Spectra Physics) and regenerative amplifier (Spitfire Pro XP, Spectra Physics). The oscillator provides ~1 W average power at 80 MHz (12.5 nJ) which is used to seed the regenerative amplifier ("regen"). The seed is spectrally chirped to ~1 ps using a grating-based stretcher and injected into the regen using a Pockels cell which also acts as a pulse picker to reduce the repetition rate to 1 kHz. The seed is amplified in a Ti:Sapphire rod which is pumped by a continuous wave (CW) diode-pumped solid state Nd:YAG laser (Millenia, Spectra Physics) with 15-W average power. After a sufficient number of oscillations corresponding to the peak of the gain curve, the amplified output is dumped from the regen cavity using a Pockels cell. The

output is compressed back to 100 fs using a grating-based compressor and exits the laser as a 10-mm diameter beam with 2.5 mJ per pulse (2.5-W average power). As a consequence of the coherently amplified pulse, the output is nearly transform limited with a pulse duration of ~100 fs and spectral bandwidth of ~150 cm^{-1}.

3.4.2 Vibrational fs/ps CARS

In the vibrational fs/ps CARS (fs/ps VCARS) configuration, the amplified output from the Solstice is split using a ½ waveplate (WP) and thin-film polarizer (TFP) combination as shown in Fig. 3.19 [14]. The reflected component (1.5 mJ) is spectrally shaped using a 4-*f* pulse shaper or a Lorentzian filter as discussed in Section 3.4.4, while the remaining 1 mJ which passes through the TFP is used to pump an ultrafast optical parametric amplifier (TOPAS-C, Spectra Physics). The OPA signal is broadly tunable from 1140–2600 nm with ~150 μJ per pulse. The signal is frequency doubled to 667 nm using a 200-μm Type I β-Barium Borate (BBO) crystal resulting in ~50 μJ per pulse. An additional 500 μJ of residual pump light at 795 nm is also available.

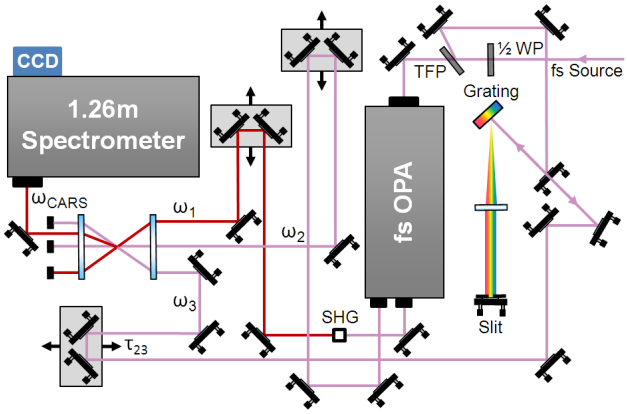

Figure 3.19. Experimental schematic for fs/ps VCARS.

The pump (ω_1) and Stokes (ω_2) pulses are the frequency-doubled OPA signal and residual fundamental OPA pump respectively with FWHM of ~150 cm^{-1}. The frequency difference between these two pulses is chosen to correspond to a vibrational Raman resonance in a target molecule.

$$\omega_1 - \omega_2 = \omega_{vib} \tag{3.60}$$

While this dissertation is primarily concerned with the vibrational Raman resonances of N_2 near 2330 cm^{-1}, several other molecules exhibit vibrational resonances accessible with the current system (O_2 at 1556 cm^{-1}, CO at 2145 cm^{-1}, and CO_2 at 1388 and 1285 cm^{-1}) [7, 35]. Because of the broadband nature of the fs pulses, the entire rovibrational manifold of N_2 is excited by the pump-Stokes interaction. The energy level diagram showing relative pulse bandwidth is given as Fig. 3.20(a) for fs/ps VCARS [36].

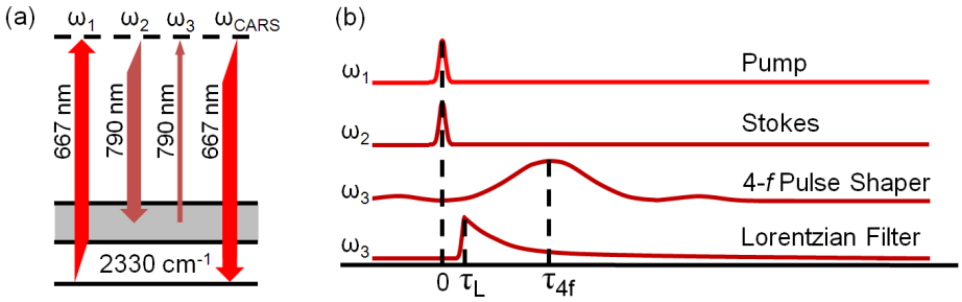

Figure 3.20. (a) Energy and (b) timing diagram for fs/ps VCARS.

The output of the pulse shaper is used to probe the excited Raman coherence induced by the pump and Stokes pulses with ~40 μJ per pulse. For fs/ps VCARS, a spectral bandwidth of ~13 cm^{-1} is utilized with sufficient spectral resolution to resolve the ground and excited state rovibrational transitions [36]. The probe pulse is delayed in time (Fig. 3.20(b))

using a high-resolution delay stage (ILS150PP, Newport) with 5 μm accuracy corresponding to 33 fs in the double-pass configuration, and a total travel of 150 mm corresponding to 1 ns.

The pump, Stokes, and probe pulses are focused using a 2-inch diameter 300-mm plano-convex lens with parallel polarizations (p-oriented). The beams are arranged in a folded BOXCARS phase-matching configuration as given in Fig. 3.3 [8] and discussed in Section 3.2.1. The resultant anti-Stokes shifted beam has frequency $\omega_{CARS} = \omega_1 - \omega_2 + \omega_3$ and propagates with wave vector $\mathbf{k_{CARS}} = \mathbf{k_1} - \mathbf{k_2} + \mathbf{k_3}$. In this configuration, the pump and CARS beams are degenerate (667 nm) and the BOXCARS phase-matching configuration allows for spatial separation of the two beams. The CARS beam is collimated using a 300-mm plano-convex spherical lens, spatially filtered using two irises, and focused to a point at the entrance slit of either a 1.26-m (SPEX) or 0.303-m (Shamrock SR-303i, Andor) spectrometer.

The 1.26-m spectrometer incorporates a 600 line/mm grating yielding an instrument resolution of 1.14 cm^{-1} with a 1600×200 pixel electron-multiplied charge-coupled device (EMCCD) camera (DU-970P-UVB, Newton). The 0.303-m spectrometer uses a 1200 line/mm grating with an instrument resolution of 2.4 cm^{-1} with the Newton EMCCD camera. Two different EMCCD cameras are compatible with the 0.303-m spectrometer. The Newton DU-970P-UVB is capable of 1-kHz operation in standard mode and 0.5-kHz operation in EM mode. The pixel size is 16×16 μm with a 100% fill factor and thermoelectric cooling (TEC) to -50° C is utilized to reduce detector noise. The UVB (back-illuminated with ultraviolet coating) yields a quantum efficiency (QE) of nearly 95% at 667 nm. For 1-kHz EM operation, a second 512×512 pixel EMCCD camera (Princeton Instruments ProEM) is used with 16×16 μm pixel size. The back-illuminated EMCCD has a QE of nearly 95% at 667

nm. Each camera is operated using a PC and individual spectra are stored in a 16-bit format for storage and processing.

3.4.3 Rotational fs/ps CARS

The rotational fs/ps CARS (fs/ps RCARS) configuration is similar to the fs/ps VCARS scheme but requires no frequency conversion. As shown in Fig. 3.21 [11], the output of the Solstice laser is split using a ½ WP/TFP combination with ~100 μJ in the transmitted component and the remainder in the reflected component. The pump and Stokes pulses are evenly split using a 50/50 ultrafast beam splitter resulting in ~45 μJ per pulse. This pulse energy is chosen to increase the energy available for the probe pulse, and to avoid Raman pumping, Stark shifting, and interference from sustained molecular alignment.

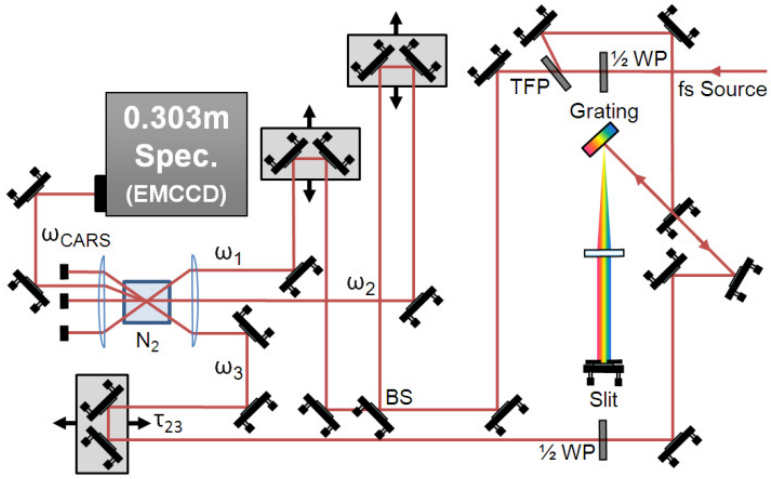

Figure 3.21. Experimental schematic for fs/ps RCARS.

The remainder of the energy (up to 1.5 mJ) is used to produce the spectrally-narrowed probe pulse via a 4-*f* pulse shaper (as shown in Fig. 3.21) or a Fabry-Pérot etalon. The narrowed output (2–5 cm^{-1}) is used to probe the induced rotational coherence with up to 20

μJ per pulse. Unlike fs/ps VCARS, the pump and Stokes pulses are degenerate at the fundamental laser wavelength (795 nm), exciting rotational transitions within a bandwidth of ~200 cm^{-1} as shown in the energy diagram of Fig. 3.22(a). The pump, Stokes, and probe pulses are degenerate and are focused using a 300-mm plano-convex spherical lens in the BOXCARS phase-matching configuration.

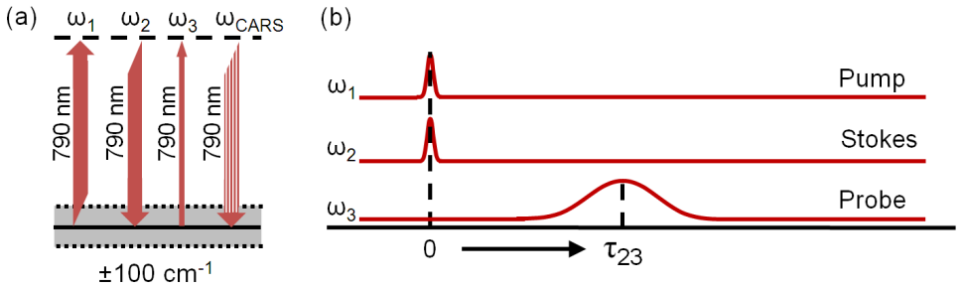

Figure 3.22. (a) Energy and (b) timing diagram for fs/ps RCARS.

Because fs/ps RCARS is operated in a fully degenerate configuration, the CARS beam is generated at 795 nm and must be collimated and spatially filtered using two irises before being focused to the slit of a 0.303-m spectrometer. The spectrometer incorporates a 1200 line/mm grating resulting in an instrument resolution of 2.4 cm^{-1} when operated with the Newton EMCCD camera (DU-970P-UVB, Newton). The camera is operated using a PC and the spectra are stored in a 16-bit format.

3.4.4 Spatial Resolution

The spatial resolution of the measurement volume is an important parameter in CARS measurements since the CARS signal is proportional to the energy per volume and the measurement resolution is dictated by the volumetric overlap of the three pulses. The focal volume can be considered an ellipsoid with major axis along the length of the focus and

minor axes along the diameter of the focus. For an ellipsoid with equal semi-minor axes such as experienced in the CARS focal volume, the volume in cm^3 is computed

$$V = \frac{4}{3}\pi a^2 b \tag{3.61}$$

where a is the radius of the focal point in cm and b is half the interaction length in cm. The minor radius, a, was measured as ~25 μm by placing a thin sheet of aluminum into the focal point and measuring the radius of the hole using a microscope. The interaction length was determined by passing thin glass axially along the interaction length and recording the nonresonant signal generated form the glass. The major radius, b, was defined as half the interaction length where the nonresonant signal was greater than $1/e$ of the maximum signal with a value of 550 μm. Since the density of glass is much larger than the density of combustion products, the measured interaction length represents the maximum, and shorter interaction lengths are expected in the gas-phase. Using Eq. 3.61, the focal volume is calculated to be 1.44×10^{-6} cm^3.

3.4.5 Pulse-Shaping Strategies

The primary innovation of fs/ps CARS is the inclusion of a simple pulse shaper to create a transform-limited probe pulse with sufficient spectral resolution to resolve rotational or rovibrational transitions. In this work, three different pulse shapers are utilized to produce a spectrally-narrowed probe with bandwidth of 2–13 cm^{-1} and time symmetric and asymmetric temporal shapes from 1–10 ps. The first is a simple 4-*f* pulse shaper as depicted in Fig. 3.23(a), while the second and third are variations of a Fabry-Pérot etalon as shown in Fig. 3.23(b).

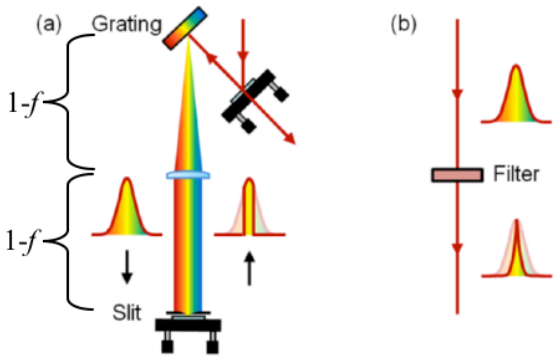

Figure 3.23. (a) Grating-based 4-*f* pulse shaper and (b) etalon-based pulse shaper.

The custom built 4-*f* pulse shaper incorporates an 1800 line/mm grating (10HG1800-500-1, Newport) to spectrally disperse the transform-limited 100-fs pulse. The dispersed pulse is collimated in the dispersion direction using a 300-mm plano-convex cylindrical lens placed 300 mm (1 focal length, *f*) from the grating. A broadband protected silver mirror is placed at the Fourier plane, one *f* from the cylindrical lens. The theoretical dispersion [cm^{-1}/mm] can be calculated for the grating/lens combination by first calculating the diffraction angle, $\beta_{\pm}$, for wavelengths $\lambda_{\pm} = \lambda_o \pm \Delta\lambda$ with center wavelength λ_o [37]

$$\beta_{\pm} = \sin^{-1}\left[\frac{m\lambda_{\pm}}{d} - \sin(\alpha)\right] \tag{3.62}$$

where m is the diffraction order, λ is the wavelength (mm), d is the inverse of the groove density (mm), and α is the input angle of 30°. As shown in Fig. 3.24, the dispersed distance, $D_{\pm}$, for $\lambda_{\pm} = \lambda_{center} \pm \Delta\lambda$ can be computed once the diffraction angle, $\beta_{\pm}$, is known by the relationship

$$D_{\pm} = f\tan(\beta_{\pm} - \beta_o) \tag{3.63}$$

where f is the focal length (mm) of the cylindrical lens. For first order diffraction from the 1800 line/mm grating with α = 30° and f = 300 mm, the theoretically calculated dispersion is 10.7 cm^{-1}/mm. The experimental value (12.5 cm^{-1}/mm) was measured using a spectrometer (HR4000, Ocean Optics) and falls within 17% of the theoretical value. The difference is due to uncertainty in the input angle, α, and the placement of the cylindrical lens, f.

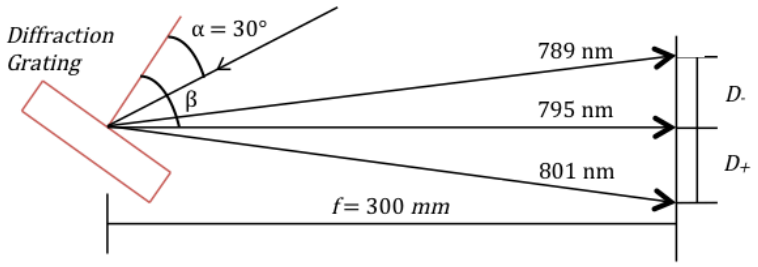

Figure 3.24. Schematic of the diffraction grating with m = 1 and input angle α = 30°.

An adjustable rectangular slit (VA100, Thorlabs) is placed on the surface of the high-reflector and allows a selectable portion of the total bandwidth to be reflected back to the grating. The mirror is vertically tilted to position the reflected beam above the input beam on the grating, thus allowing separation of the pulse-shaped beam. The slit has a minimum resolvable width of ~100 μm and maximum width of 5 mm which corresponds to 1.2 cm^{-1} and 60 cm^{-1} respectively given the measured dispersion of 12.5 cm^{-1}/mm. For fs/ps VCARS, the slit is typically set to ~850 μm which roughly corresponds to $\Delta\nu$ = ~12 cm^{-1} [36]. For fs/ps RCARS, the slit width is reduced to ~200 μm to produce a pulse with $\Delta\nu$ = ~2.1 cm^{-1} as shown in Fig. 3.25(a) [11].

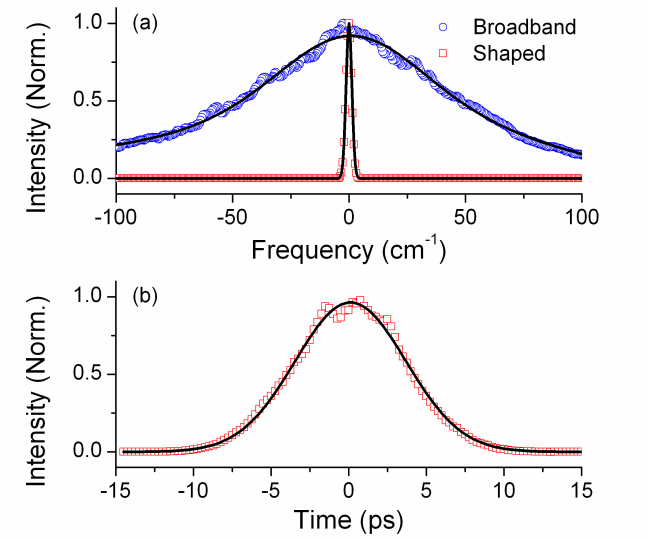

Figure 3.25. (a) Broadband input and spectrally-narrowed output of the 4-*f* pulse shaper and (b) corresponding temporally-stretched pulse.

Since the fs source is mode locked, meaning all frequencies oscillate in phase, the pulse-shaped output is both spectrally and temporally altered, related through the Fourier Transform. For a rectangular function, $\Pi(\Gamma)$, the Fourier Transform is given as

$$F_\omega\left[\Pi(\Gamma)\right](t) = \frac{\sin\left[2\pi\left(\frac{\Gamma c}{2}\right)t\right]}{2\pi\left(\frac{\Gamma c}{2}\right)t} = \operatorname{sinc}(\pi c \Gamma t) \tag{3.64}$$

$$\Pi(\Gamma) = \begin{cases} 0 & \text{if } |\omega - \omega_o| > 0.5\Gamma \\ 0.5 & \text{if } |\omega - \omega_o| = 0.5\Gamma \\ 1 & \text{if } |\omega - \omega_o| < 0.5\Gamma \end{cases} \tag{3.65}$$

where c is the speed of light (cm/s) and Γ is the full width of the rectangular function (cm^{-1}). Since the absolute value of the electric field is measured, the temporal shape of the output is a $sinc^2$ function as shown in Fig. 3.26.

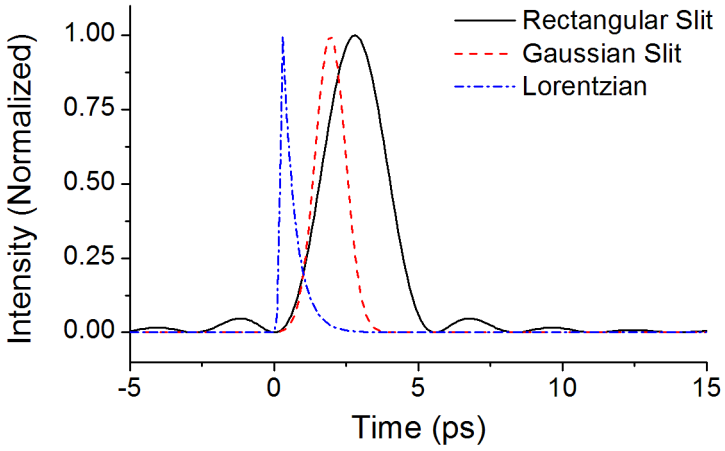

Figure 3.26. Pulse shapes for Γ = 12 cm^{-1} for rectangular slit, Gaussian slit, and etalon shown delayed for nonresonant suppression. The profile falls to 10^{-3} at 2.8 ps, 1.95 ps, and 0.3 ps respectively.

In the limiting case of fs/ps RCARS where very small slit widths are required (Fig. 3.25(b)), the resolution of the grating and slight rotation of the slit can cause the slit to act as a Gaussian function. In this case, the Fourier Transform is given as

$$F_\omega\left[\exp\left(-a\left(\omega-\omega_o\right)^2\right)\right](t)=\exp\left[-\frac{(2\pi)^2\left(t-t_o\right)^2}{a}\right] \tag{3.66}$$

$$a=\frac{4\ln(2)}{\Gamma^2c^2} \tag{3.67}$$

where ω_o is the central frequency (cm^{-1}), t_o is the center time (s), c is the speed of light (cm/s), and Γ is the full width at half maximum (cm^{-1}). The transform-limited Gaussian pulse has a time bandwidth product $\Gamma\Delta t$ = 0.44 and therefore falls to 10^{-3} significantly faster than the rectangular slit for the same spectral bandwidth as shown in Fig. 3.26.

In addition to the 4-*f* pulse shaper, two different etalon-based methods are used to greatly simplify the CARS configuration and reduce the probe delay necessary for 10^3

nonresonant suppression [36]. The first method uses a dielectric-coated interference filter with 13-cm^{-1} FWHM Lorentzian spectral profile (OS004308, Chroma) with a total throughput of 1.5% at 795 nm and is angle tunable. The second method uses an air-spaced Fabry-Pérot etalon (TecOptics) with free spectral range of 250 cm^{-1} and finesse of 45. The bandwidth, $\Delta\omega$, can be determined given the free spectral range, FSR (cm^{-1}), and finesse, f, by the relationship

$$f = \frac{FSR}{\Delta\omega} \tag{3.68}$$

where $\Delta\omega$ = 5.6 cm^{-1} centered at 795 nm and is angle tunable. The first method is used for fs/ps VCARS where only the broad vibrational transitions are resolved and the latter is used for fs/ps RCARS where individual rotational transitions are resolved.

Both methods behave as a Fabry-Pérot etalon in the small gap limit [38]. The etalon consists of two parallel mirrors with partial reflection, R, separated by an air-gap with spacing, d. The reflectivity is computed from the finesse

$$f = \frac{\pi\sqrt{R}}{1-R} \tag{3.69}$$

where R is ~93% for a finesse of 45. The etalon spacing is computed from the FSR

$$d = \frac{1}{2FSR} \tag{3.70}$$

where d is 20 μm for FSR = 250 cm^{-1}. As shown in the inset of Fig. 3.27(top) assuming a normalized input into the etalon after the first mirror, the first pass through the etalon allows (1-R) = 7% transmission, T. The second pass allows T = (R)(R)(1-R) = 6.1%. This can be computed using the series

$$T(p) = (1-R)(R)^{2(p-1)} \tag{3.71}$$

where p is the number of passes as shown in Fig. 3.27(top). If the etalon is in the small gap limit where the coherence length, l_c, is greater than the gap, d, then the temporal profile of each pass overlaps producing a nearly continuous output with a characteristic exponential decay. For a 100-fs pulse the coherence length $l_c = c\Delta t$ = 30 μm and the gap distance is computed as 20 μm for FSR = 250 cm^{-1} so $l_c > d$ and the etalon operates in the small gap limit as shown in Fig. 3.27(bottom).

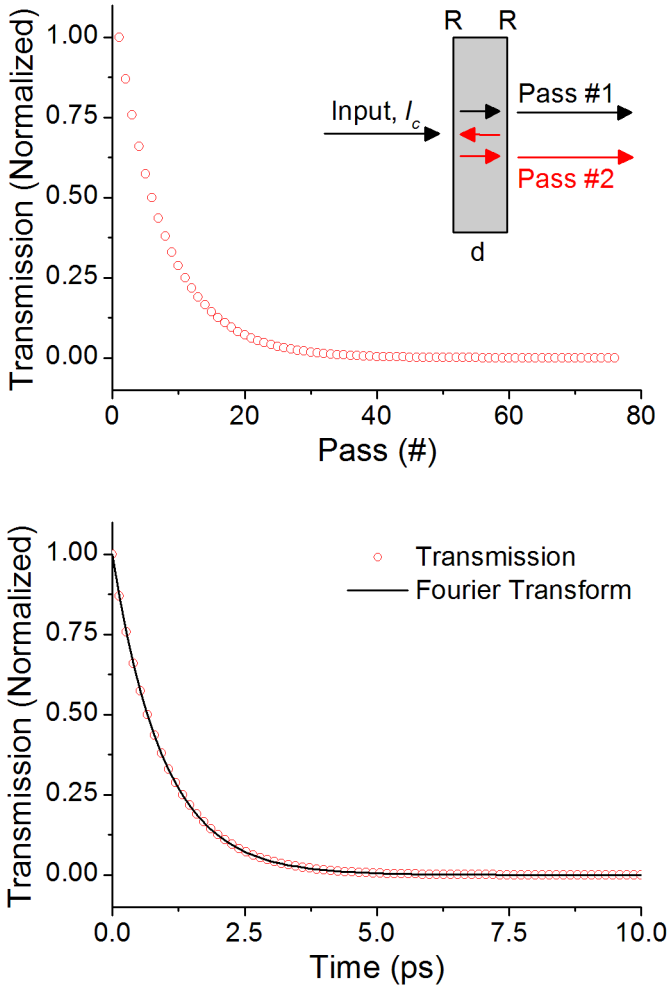

Figure 3.27. (top) Diagram of etalon (inset) and output as a function of pass, and (bottom) computed output as a function of time (symbols) and FFT (line) of the TecOptics etalon.

Because the etalon operates in the small gap limit, the output pulse train can be considered continuous and compared to the Fourier Transform of a Lorentzian spectral profile

$$F_{\omega}\left[\frac{\frac{1}{2}\Gamma}{(\omega-\omega_o)^2+\left(\frac{1}{2}\Gamma\right)^2}\right](t)=\exp(-2\pi c\Gamma t) \tag{3.72}$$

where Γ is the FWHM (cm^{-1}), ω_o is the central frequency (cm^{-1}), and c is the speed of light (cm/s). In this case, the Fourier Transform is not defined for $t < 0$. Instead, the pulse rises with a FWHM similar to the initial input pulse, 100 fs in this case. This creates a time-asymmetric pulse with a fast rise time and singly exponential decay as shown in Fig. 3.26.

3.4.6 Atmospheric-Pressure Combustion Hardware and Theory

The fs/ps VCARS technique was validated using a well-characterized H_2–air laminar diffusion flame stabilized over a Hencken burner. The Hencken burner consists of a 1"×1" honeycomb with fuel and oxidizer jets interspersed throughout. This is surrounded by a 1.5"×1.5" co-flow shroud. The co-flow acts as a barrier to prevent O_2 from the surrounding air from diffusing into the reaction. The burner has been the subject of detailed investigations with CARS temperature probes and provides nearly uniform and adiabatic temperatures [39]. The validation measurements were taken 20 mm above the center of the burner surface where the temperature is accurately predicted by equilibrium theory using STANJAN combustion software.

The temperature was varied by adjusting the fuel-air ratio of the fuel and oxidizer supplies. For the complete combustion of hydrogen in air,

$$H_2 + a\left(O_2 + 3.76N_2\right) \rightarrow H_2O + \left(a - \tfrac{1}{2}\right)O_2 + 3.76aN_2 \tag{3.73}$$

where a = ½ for stoichiometric conditions. The equivalence ratio, defined as the local fuel-air ratio divided by the stoichiometric fuel-air ratio, can be rewritten in terms of a as

$$\Phi = \frac{\left(F/A\right)}{\left(F/A\right)_{stoich}} = \frac{\left(1/4.76a\right)}{\left(1/4.76a_{stoich}\right)} = \frac{a_{stoich}}{a} = \frac{1}{2a} \tag{3.74}$$

and the fuel-air ratio is written as a function of Φ

$$\frac{F}{A} = \frac{1}{4.76a} = \frac{2\Phi}{4.76} = 0.420\Phi \tag{3.75}$$

For standard temperature and pressure (298.15 K and 1 atm), the molar volume of all molecules is equal to 22.4 L, so the molar and volumetric flow rates are equal. The temperature is calculated from the First Law of Thermodynamics

$$n_r \sum_i \chi_{i,r} h_{i,r} = n_p \sum_i \chi_{i,p} h_{i,p} + Q_{out} \tag{3.76}$$

where n_r and n_p are the total moles of reactants and products respectively (kmol), $\chi_{i,r}$ and $\chi_{i,p}$ are the mole fraction of reactant and products respectively, $h_{i,r}$ and $h_{i,p}$ are the molar enthalpies of reactant and products respectively (kJ/kmol), and Q_{out} is the heat extracted from the products (kJ). The molar enthalpies are composed of two parts

$$h_{i,tot} = \Delta h^o_{f,i} + h_i\left(T_p\right) - h_i\left(T_{ref}\right) \tag{3.77}$$

where $\Delta h_{f,i}^o$ is the enthalpy of formation and $h_i(T_p)$ - $h_i(T_{ref})$ is the sensible enthalpy needed to raise the temperature of the component to the product temperature, T_p. For adiabatic conditions, Q_{out} = 0, the First Law can be written as $H_{r,tot}(T_r) = H_{p,tot}(T_p)$ and the product temperature can be calculated. The adiabatic flame temperature and mole fraction of the

major species of H_2-air combustion are plotted as a function of Φ in Fig. 3.28. The values were computed using STANJAN equilibrium software.

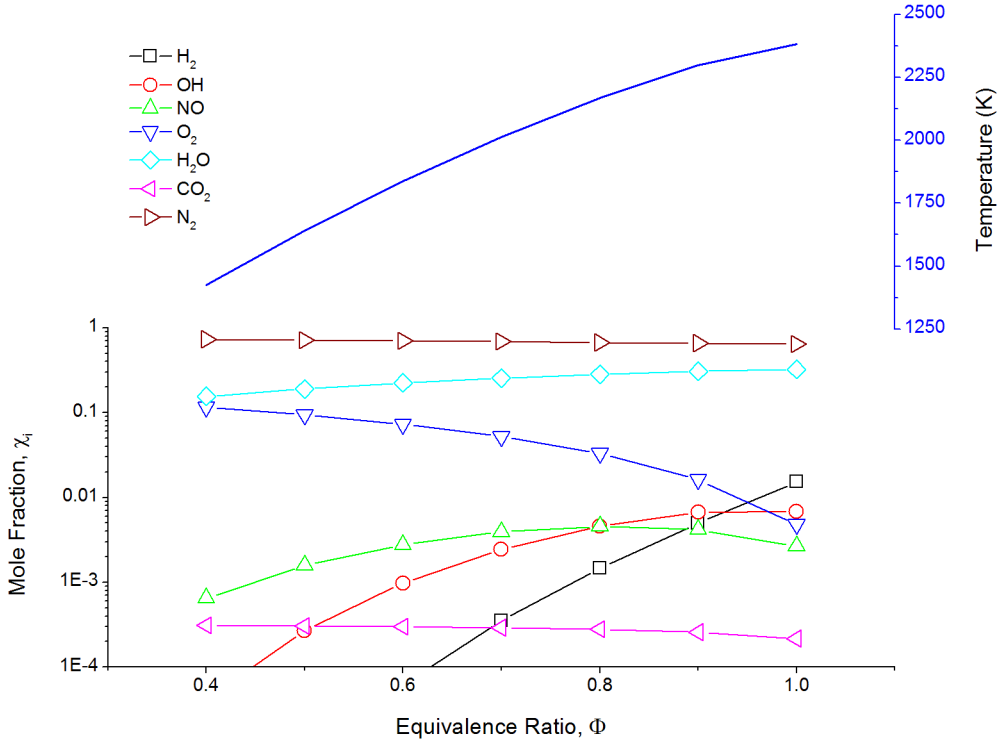

Figure 3.28. Calculated adiabatic flame temperature and mole fraction of major product species for H_2-air combustion.

The equivalence ratio was varied from 0.4–1.0 by controlling the mass flow rate of the fuel and oxidizer. The air flow rate was held constant using a 0–100 standard liter per minute (SLPM) mass flow controller (Alicat Scientific) with an accuracy of ±(0.8% of the reading + 0.2% of full scale). This results in an uncertainty of 0.52 SLPM at a 40 SLPM flow rate. The fuel flow rate was varied from ~7–17 SLPM corresponding to Φ = 0.4–1.0, using a 0–50 SLPM mass flow controller (Alicat Scientific). The mass flow rate uncertainty yields a maximum equivalence ratio uncertainty $\Delta\Phi = \pm 0.03$ and temperature uncertainty ΔT

= ±15 K at Φ = 1.0. This is well within the experimental uncertainty associated with the fs/ps CARS temperature measurement.

3.4.7 Atmospheric-Pressure Low-Temperature Flow Cell

The fs/ps RCARS technique was validated in low-temperature flow from 298–700 K using a heated jet. A 1.5-kW inline resistance heater was placed in a 1-inch diameter pipe with a N_2 flow rate of 15 SLPM using a 0–50 SLPM mass flow controller (Alicat Scientific). The heater element current was varied to control the gas temperature. The output was routed to a 0.75-inch diameter windowless cell allowing the CARS beams to focus in the jet while minimizing heat loss and mixing of the heated gas with ambient air. A 0.0625" K-type thermocouple was inserted into the cell and the temperature measurements were corrected for convection and radiation heat-transfer losses.

3.4.8 High-Pressure Room-Temperature Cell

The pressure-dependence of the fs/ps RCARS signal and associated pressure-broadened Raman linewidth measurements were investigated in a room-temperature windowed cell. The stainless steel cell has line-of-sight optical access with 0.375-inch thick 1-inch diameter windows on each end. Both N_2 and O_2 were supplied to the cell from high-pressure gas cylinders (~2000 psi) at room temperature and controlled by pressure regulators (Concoa). The cell pressure was measured with a digital pressure gauge (0–500 psi) with accuracy of 0.25% of full scale (1.25 psi). A 0.0625-inch K-type thermocouple was placed inside the cell to measure temperature. Although the cell is rated to 50 atm, only pressures as high as 20 atm were investigated in the current work.

3.5 References

1. A. C. Eckbreth, *Laser diagnostics for combustion temperature and species*, (Gordon and Breach Publishers, 1996).
2. D. A. McQuarrie and J. D. Simon, *Physical chemistry: a molecular approach*, (University Science Books, Sausalito, Calif., 1997).
3. E. Goulielmakis, Z.-H. Loh, A. Wirth, R. Santra, N. Rohringer, V. S. Yakovlev, S. Zherebtsov, T. Pfeifer, A. M. Azzeer, M. F. Kling, S. R. Leone, and F. Krausz, "Real-time observation of valence electron motion," *Nature* **466**, 739–743 (2010).
4. G. Herzberg, *Molecular spectra and molecular structure,* 2nd ed., (R.E. Krieger Pub. Co., Malabar, Fla., 1989).
5. S. Mukamel, *Principles of nonlinear optical spectroscopy*, (Oxford University Press, New York, 1995).
6. S. A. Tedder, J. L. Wheeler, A. D. Cutler, and P. M. Danehy, "Width-increased dual-pump enhanced coherent anti-Stokes Raman spectroscopy," *Appl. Opt.* **49**, 1305–1313 (2010).
7. S. Roy, D. Richardson, P. J. Kinnius, R. P. Lucht, and J. R. Gord, "Effects of N_2-CO polarization beating on femtosecond coherent anti-Stokes Raman scattering spectroscopy of N_2," *Appl. Phys. Lett.* **94**, 144101 (2009).
8. A. C. Eckbreth, "Boxcars: crossed-beam phase-matched CARS generation in gases," *Appl. Phys. Lett.* **32**, 421–423 (1978).
9. S. Roy, T. R. Meyer, and J. R. Gord, "Time-resolved dynamics of resonant and nonresonant broadband picosecond coherent anti-Stokes Raman scattering signals," *Appl. Phys. Lett.* **87**, 264103 (2005).
10. F. M. Kamga and M. G. Sceats, "Pulse-sequenced coherent anti-Stokes Raman-scattering spectroscopy: method for suppression of the non-resonant background," *Opt. Lett.* **5**, 126–128 (1980).
11. J. D. Miller, S. Roy, M. N. Slipchenko, J. R. Gord, and T. R. Meyer, "Single-shot gas-phase thermometry using pure-rotational hybrid femtosecond/picosecond coherent anti-Stokes Raman scattering," *Opt. Express* **19**, 15627–15640 (2011).
12. B. D. Prince, A. Chakraborty, B. M. Prince, and H. U. Stauffer, "Development of simultaneous frequency- and time-resolved coherent anti-Stokes Raman scattering for ultrafast detection of molecular Raman spectra," *J. Chem. Phys.* **125**, 044502 (2006).
13. D. Richardson, R. Lucht, W. Kulatilaka, S. Roy, and J. Gord, "Theoretical modeling of single-laser-shot, chirped-probe-pulse femtosecond coherent anti-Stokes Raman scattering thermometry," *Appl. Phys. B* **104**, 699–714 (2011).
14. J. D. Miller, M. N. Slipchenko, T. R. Meyer, H. U. Stauffer, and J. R. Gord, "Hybrid femtosecond/picosecond coherent anti-Stokes Raman scattering for high-speed gas-phase thermometry," *Opt. Lett.* **35**, 2430–2432 (2010).
15. I. N. Levine, *Quantum chemistry,* 6th ed., (Pearson Prentice Hall, Upper Saddle River, N.J., 2009).
16. G. Herzberg and J. W. T. Spinks, *Molecular spectra and molecular structure*, (Prentice-Hall, New York,, 1939).
17. R. E. Palmer, "The CARSFT computer code calculating coherent anti-Stokes Raman spectra: User and programmer information," SAND-89-8206 (1989).

18. A. Bohlin, P.-E. Bengtsson, and M. Marrocco, "On the sensitivity of rotational CARS N_2 thermometry to the Herman–Wallis factor," *J. Raman Spectrosc.* **42**, 1843–1847 (2011).
19. K. E. Bertagnolli and R. P. Lucht, "Temperature profile measurements in stagnation-flow, diamond-forming flames using hydrogen cars spectroscopy," *Symp. (Int.) Comb.* **26**, 1825–1833 (1996).
20. G. Knopp, P. Beaud, P. Radi, M. Tulej, B. Bougie, D. Cannavo, and T. Gerber, "Pressure-dependent N_2 Q-branch fs-CARS measurements," *J. Raman Spectrosc.* **33**, 861–865 (2002).
21. F. Vestin, K. Nilsson, and P. E. Bengtsson, "Validation of a rotational coherent anti-Stokes Raman spectroscopy model for carbon dioxide using high-resolution detection in the temperature range 294-1143 K," *Appl. Opt.* **47**, 1893–1901 (2008).
22. D. M. Mosbacher, "Temperature measurements using UV-induced vibrational hydrogen Raman bandshape spectroscopy," (Vanderbilt University, Nashville, TN, 2004).
23. G. Millot, R. Saintloup, J. Santos, R. Chaux, H. Berger, and J. Bonamy, "Collisional Effects in the Stimulated Raman-Q Branch of O_2 and O_2-N_2," *J. Chem. Phys.* **96**, 961–971 (1992).
24. A. Bohlin, E. Nordström, P.-E. Bengtsson, and M. Marrocco, "On the sensitivity of rotational O_2 CARS thermometry to the Herman–Wallis factor," *J. Raman Spectrosc.,* DOI 10.1002/jrs.3147 (2012).
25. M. Marrocco, "Comparative analysis of Herman-Wallis factors for uses in coherent anti-Stokes Raman spectra of light molecules," *J. Raman Spectrosc.* **40**, 741–747 (2009).
26. L. A. Rahn and R. E. Palmer, "Studies of nitrogen self-broadening at high-temperature with inverse Raman spectroscopy," *J. Opt. Soc. Am. B* **3**, 1164–1169 (1986).
27. W. D. Kulatilaka, P. S. Hsu, H. U. Stauffer, J. R. Gord, and S. Roy, "Direct measurement of rotationally resolved H_2 Q-branch Raman coherence lifetimes using time-resolved picosecond coherent anti-Stokes Raman scattering," *Appl. Phys. Lett.* **97**, 081112 (2010).
28. J. D. Miller, C. E. Dedic, S. Roy, J. R. Gord, and T. R. Meyer, "Interference-free gas-phase thermometry at elevated pressure using hybrid femtosecond/picosecond rotational coherent anti-Stokes Raman scattering," *Opt. Express* **20**, 5003–5010 (2012).
29. T. Seeger, F. Beyrau, A. Brauer, and A. Leipertz, "High-pressure pure rotational CARS: comparison of temperature measurements with O_2, N_2 and synthetic air," *J. Raman Spectrosc.* **34**, 932–939 (2003).
30. J. M. Hartmann, C. Boulet, and D. Robert, *Collisional effects on molecular spectra,* 1 ed., (Elsevier Science, 2008).
31. L. Martinsson, P. E. Bengtsson, M. Alden, S. Kroll, and J. Bonamy, "A test of different rotational Raman linewidth models: accuracy of rotational coherent anti-Stokes Raman scattering thermometry in nitrogen from 295 K to 1850 K," *J. Chem. Phys.* **99**, 2466–2477 (1993).
32. J. D. Miller, S. Roy, J. R. Gord, and T. R. Meyer, "Communication: Time-domain measurement of high-pressure N_2 and O_2 self-broadened linewidths using hybrid

femtosecond/picosecond coherent anti-Stokes Raman scattering," *J. Chem. Phys.* **135**, 201104 (2011).
33. R. P. Lucht, S. Roy, T. R. Meyer, and J. R. Gord, "Femtosecond coherent anti-Stokes Raman scattering measurement of gas temperatures from frequency-spread dephasing of the Raman coherence," *Appl. Phys. Lett.* **89**, 251112 (2006).
34. K. V. Price, R. M. Storn, and J. A. Lampinen, *Differential evolution: a practical approach to global optimization*, (Springer, Berlin ; New York, 2005).
35. W. D. Kulatilaka, J. R. Gord, and S. Roy, "Effects of O_2-CO_2 polarization beating on femtosecond coherent anti-Stokes Raman scattering (fs-CARS) spectroscopy of O_2," *Appl. Phys. B* **102**, 141–147 (2011).
36. J. D. Miller, M. N. Slipchenko, and T. R. Meyer, "Probe-pulse optimization for nonresonant suppression in hybrid fs/ps coherent anti-Stokes Raman scattering at high temperature," *Opt. Express* **19**, 13326–13333 (2011).
37. J. D. Ingle and S. R. Crouch, *Spectrochemical Analysis*, (Prentice Hall, Englewood Cliffs, NJ, 1988).
38. A. Lagutchev, S. A. Hambir, and D. D. Dlott, "Nonresonant background suppression in broadband vibrational sum-frequency generation spectroscopy," *J. Phys. Chem. C* **111**, 13645–13647 (2007).
39. R. D. Hancock, K. E. Bertagnolli, and R. P. Lucht, "Nitrogen and hydrogen CARS temperature measurements in a hydrogen/air flame using a near-adiabatic flat-flame burner," *Combust. Flame* **109**, 323–331 (1997).

CHAPTER 4. HYBRID FEMTOSECOND/PICOSECOND COHERENT ANTI-STOKES RAMAN SCATTERING FOR HIGH-SPEED GAS-PHASE THERMOMETRY

Modified from a paper published in *Optics Letters* **35**, 2430–2432 (2010).

Joseph D. Miller,[1] Mikhail N. Slipchenko,[2] Terrence R. Meyer,[1,3] Hans U. Stauffer,[4] and James R. Gord[5]

Hybrid femtosecond/picosecond (fs/ps) coherent anti-Stokes Raman scattering (CARS) is demonstrated for high-speed thermometry in unsteady high-temperature flames, including successful comparisons with a time- and frequency-resolved theoretical model. After excitation of the N_2 vibrational manifold with 100-fs broadband pump and Stokes beams, the Raman coherence is probed using a frequency-narrowed 2.5-ps probe beam that is time delayed to suppress nonresonant background by two orders of magnitude. Experimental spectra were obtained at 500 Hz in steady and pulsed H_2–air flames and exhibit a temperature precision of 2.2% and an accuracy of 3.3% up to 2400 K. Strategies for real-time gas-phase thermometry in high-temperature flames are also discussed, along with implications for kHz-rate measurements in practical combustion systems.

[1] Department of Mechanical Engineering, Iowa State University, Ames, IA
[2] Weldon School of Biomedical Engineering, Purdue University, West Lafayette, IN
[3] SAOT, Erlangen Graduate School in Advanced Optical Technologies, University of Erlangen-Nuremberg, Erlangen, Germany
[4] Spectral Energies, LLC, Dayton, OH
[5] Air Force Research Laboratory, Propulsion Directorate, WPAFB, OH

4.1 Introduction

Time-domain coherent anti-Stokes Raman scattering (CARS) thermometry for kHz-rate detection of combustion instabilities has recently been demonstrated using a femtosecond (fs) laser source [1]. If a chirped probe pulse is employed, the time decay of the CARS signal caused by frequency-spread dephasing can be detected with a spectrometer and related to the gas-phase temperature on each laser shot. This approach produces tremendous signal levels, but the measured time decay is sensitive to the temporal and spectral shapes of the probe pulse and the ratio of the resonant to nonresonant signals. In practical combustion systems, these may be perturbed by the presence of thick test-cell windows and by varying pressure, species concentrations, and temperature within the reacting medium [2]. These challenges, along with interference from more abundant species that may be excited simultaneously by the broadband fs pulses, will ultimately require advanced pulse shaping strategies. As one alternative to time-domain fs CARS, we demonstrate the use of a hybrid fs/ps-CARS technique for high-speed thermometry that exceeds previous frequency-domain measurement rates by one to two orders of magnitude [3]. The measurement precision is on the same order as that reported using fs time-domain spectroscopy [1], while the high-speed measurement accuracy is improved and potential uncertainties due to nonresonant background [4], sensitivity to characteristics of the probe pulse, and interferences in multicomponent mixtures [5] are reduced. Whereas previous work on hybrid fs/ps-CARS has been focused primarily on bio-chemical sensing in the condensed phase [6] or on gas phase speciation at low temperature [5], the potential of this technique for accurate, real-time, high-speed thermometry in high-temperature gases is demonstrated here, along with successful implementation of a time- and frequency-resolved theoretical model.

As shown in Fig. 1, a 100-fs pulse at the fundamental wavelength (790 nm) of a regeneratively amplified Ti:sapphire laser is used to pump an optical parametric amplifier (OPA) to produce a frequency-doubled signal at 668 nm for the pump beam, ω_1, with $\Delta\omega \approx 150$ cm^{-1}. Residual 790-nm energy from the OPA is used for the Stokes pulse, ω_2, with $\Delta\omega \approx 150$ cm^{-1}, and is temporally overlapped with the pump to generate an oscillating coherence covering the full rovibrational spectrum of N_2 near 2330 cm^{-1}. A transform-limited narrowband probe pulse, ω_3, with $\Delta\omega \approx 12$ cm^{-1} is selected from a small spectral portion of the high-energy 790-nm laser pulse using a grating-based, folded, 4-*f* pulse-shaping system [6]. The probe-pulse delay, τ_{23}, is selected to minimize the nonresonant background by setting the first minima of the sinc^2 probe pulse coincident with the pump and Stokes pulses. The spectrally resolved CARS signal, ω_{CARS}, is degenerate with the pump beam, but can be spatially separated using the folded-BOXCARS phase-matching configuration ($\mathbf{k_{CARS}} = \mathbf{k_1} - \mathbf{k_2} + \mathbf{k_3}$). The pump, Stokes, and probe beams have parallel polarizations and are focused to a 75-μm probe diameter with a 300-mm lens. The energies of the pump, Stokes, and probe pulses are 20 μJ, 450 μJ, and 25 μJ, respectively. The CARS process is performed in the unsaturated regime, as verified by the linear dependence of the CARS signal on the Stokes power. The CARS signal is spatially filtered with an iris, re-collimated, and directed to a 1.26-m spectrometer with a 600-line/mm grating and an electron-multiplying charge-coupled-device (EMCCD) detector. The EMCCD is configured to acquire CARS spectra at 500 Hz, although newer commercially available lasers and cameras can exceed 1 kHz. The EMCCD camera is binned by five pixels for a resolution of 1.14 cm^{-1} per spectral element, which is sufficient to resolve the broad vibrational features of the CARS signal.

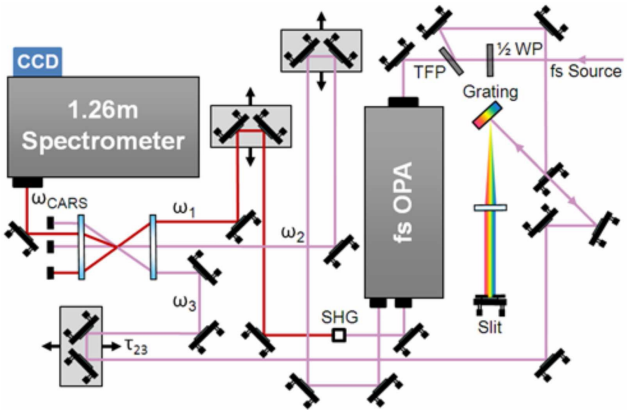

Figure 4.1. fs/ps hybrid CARS system with pump (ω_1), Stokes (ω_2), probe (ω_3), and CARS (ω_{CARS}) beams and probe delay, τ_{23}. ½ WP: half-wave plate; TFP: thin film polarizer; SHG: second harmonic generation crystal.

4.2 Comparison with Theoretical Model

A spectrally and temporally resolved theoretical model for N_2 CARS is used to simulate the experimental data. In this model, the frequency-domain CARS signal is treated as the sum of nonresonant and resonant third-order complex polarizations, $P^{(3)}$, as follows [6]:

$$I_{\mathrm{CARS}}(\omega,\tau_{12},\tau_{23}) = \left| P_{\mathrm{NR}}^{(3)}(\omega,\tau_{12},\tau_{23}) + P_{\mathrm{Res}}^{(3)}(\omega,\tau_{12},\tau_{23}) \right|^2 \tag{4.1}$$

where τ_{12} and τ_{23} denote the delays between pulses 1 (pump) and 2 (Stokes), and pulses 2 and 3 (probe), respectively. The resonant contributions to the third-order polarization are first treated in the time domain assuming a phenomenological time-domain molecular response function [6]:

$$R(t) = \sum_{m,n} \kappa_{nm} P(m) e^{-i\omega_{nm}t - \Gamma_{nm}t} \tag{4.2}$$

which accounts for the temperature-dependent populations, $P(m)$, of the Boltzmann-distributed initial states, m, of N_2. In Eq. (4.2), ω_{nm} and Γ_{nm} are the frequency and dephasing rate, respectively, associated with the N_2 Q-branch transitions ($\Delta v = +1$; $\Delta J = 0$) to final state,

n, whereas κ_{nm} represents the corresponding Raman transition strengths. An analogous response function is used to account for nonresonant contributions, but the dephasing rate is assumed to be rapid relative to the pulse durations, and a $\pi/2$ phase shift is introduced. The third-order polarizations are:

$$P^{(3)}(t,\tau_{12},\tau_{23}) = \left(\frac{i}{\hbar}\right)^3 \int_0^\infty dt_3 \int_0^\infty dt_2 \int_0^\infty dt_1 \left\{ R(t_2)\delta(t_1)\delta(t_3) E_3(t-t_3) E_2^*(t+\tau_{23}-t_3-t_2) \right. \\ \left. \times E_1(t+\tau_{23}+\tau_{12}-t_3-t_2-t_1) e^{i(\omega_1-\omega_2+\omega_3)t_3} e^{i(\omega_1-\omega_2)t_2} e^{i\omega_1 t_1} \right\} \quad (4.3)$$

where E_1, E_2, and E_3 represent, respectively, the complex time-domain electric fields associated with the pump, Stokes, and probe pulses with respective carrier frequencies ω_1, ω_2, and ω_3; t_1, t_2, and t_3 represent integration variables associated with coherence timescales separating field interactions. The $\delta(t_1)\delta(t_3)$ product arises from an assumption that the electronic dephasing timescales are fast compared to variations in pulses 1 and 2 during the first electronic coherence timescale, t_1, as well as the variations in pulse 3 and the outgoing CARS pulse during the final electronic coherence timescale, t_3. This expression is evaluated numerically for the delay τ_{23} assuming temporally-overlapped (τ_{12} = 0) transform-limited Gaussian electric fields E_1 and E_2 and an $E_3(t)$ pulse that represents the Fourier transform of a square-pulse amplitude-shaped frequency-domain electric field. Subsequent Fourier transformation of $P^{(3)}(t)$ into the frequency domain allows determination of $I_{\mathrm{CARS}}(\omega,\tau_{12}=0,\tau_{23})$ via Eq. (1).

4.3 Experimental Results

CARS measurements are performed 20 mm above the burner surface of a lifted H_2–air, nearly adiabatic, atmospheric-pressure diffusion flame stabilized over a Hencken burner (40-

slpm air flow rate). Under these conditions the flame temperature is uniformly distributed and accurately predicted by equilibrium theory [7]. The equivalence ratio of the burner (Φ), defined as the fuel–air ratio divided by the stoichiometric fuel-air ratio, is varied from 0.5–1.0, resulting in flame temperatures of 1500–2400 K. The precision of the mass flow controllers yields an uncertainty in Φ of ± 0.03 or equivalently ± 15 K at Φ = 1.0.

As is evident from Eq. 4.1 and Fig. 4.2(a), the nonresonant background contributes significantly to the CARS signal and can distort the spectral shape when the input beams are aligned in time. In contrast, the experimental spectrum in Fig. 4.2(b) corresponds to a probe delay of 2.36 ps from the pump and Stokes. This delay reduces the nonresonant background by two orders of magnitude while maintaining a sufficient signal-to-noise ratio (SNR) for

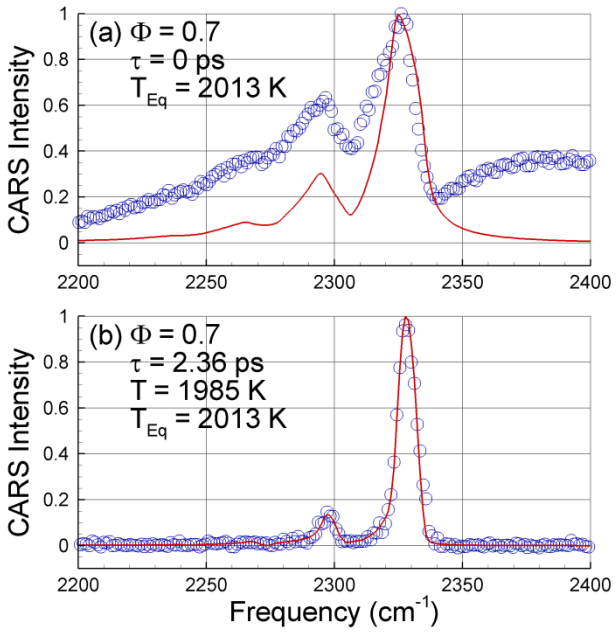

Figure 4.2. Normalized 500-Hz CARS spectra for Φ = 0.7 and probe delay of (a) 0 ps and (b) 2.36 ps. Solid line is best-fit theoretical simulation with suppressed nonresonant interference, and open symbols are experimental data. T_{Eq} is theoretical equilibrium prediction.

computing the accurate best-fit temperature using a differential evolution optimization algorithm to minimize the residual.

As displayed in Fig. 4.3, the probability density functions follow a normal distribution and broaden as temperature increases due to a decrease in SNR. The best-fit temperatures exhibit a precision of greater than 2.2% and are within 3.3% of the temperatures predicted from equilibrium theory [7]. The precision is dominated by uncertainty in spectral fitting due to spectral noise since the flame is relatively steady. This represents an improvement in accuracy over previous high-speed fs-time-domain CARS measurements [1] with potentially less sensitivity to nonresonant variations, probe-pulse perturbations, and multispecies interferences.

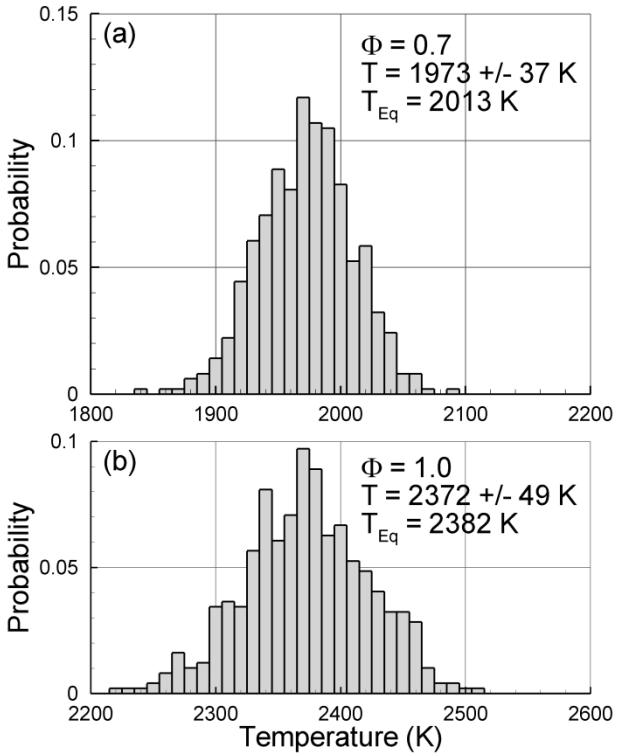

Figure 4.3. Probability density functions of best-fit flame temperature for Φ of (a) 0.7 and (b) 1.0, compared with temperatures from equilibrium theory, T_{Eq}.

4.4 High-Speed Measurements

For real-time thermometry, we explore the utilization of the relative populations in the fundamental and first three hot bands of the vibrational manifold, which are temperature dependent following the Boltzmann distribution. At a probe delay of 2.36 ps, nonresonant background suppression enables the use of a simple correlation function, derived from the CARS model, between the fundamental-to-hot-band area ratio and the theoretical temperature. Experimental temperatures are measured using CARS spectra collected at 500 Hz over a duration of one second in a steady flame and plotted in Fig. 4.4(a) for Φ = 0.7, 0.9, and 1.0. Standard deviations are better than 1.8%, which is comparable to the precision of the best-fit spectra presented earlier, with temperature accuracies of 2.9% or better. To demonstrate the ability to resolve transient phenomena, the steady flame is pulsed from Φ = 0.6 to 0.8 as shown in Fig. 4.4(b). For these measurements, the temperature is computed ~1000 times faster than the full spectral simulation routine, and appears suitable for real-time applications.

4.5 Single-Shot Accuracy and Precision as a Function of Temperature

Unlike nanosecond and picosecond CARS where rovibrational transitions in the ground vibrational state allow thermometry to 1000 K and lower, fs/ps CARS thermometry is highly dependent on the ratio of the v = 0–1 and v = 1–2 vibrational transitions. At low temperature, the population in the first excited vibrational energy state is significantly less than the population in the ground vibrational state, shown previously in Fig. 3.5, and the temperature

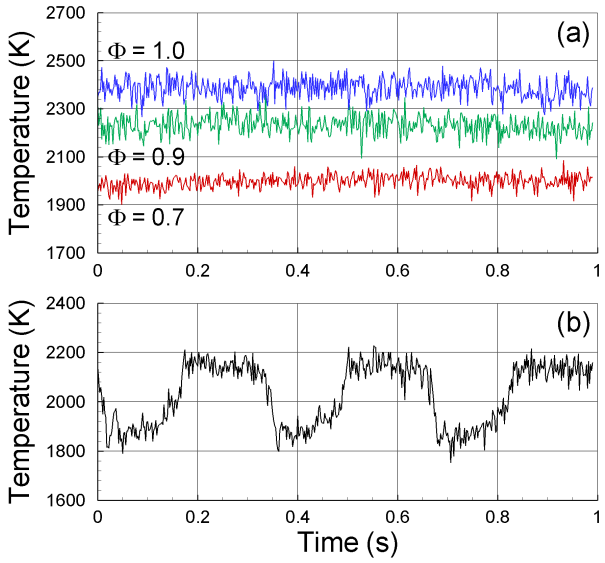

Figure 4.4. Temperature time series from fundamental-to-hot-band ratio correlation for 500-Hz hybrid CARS spectra (a) at various Φ and (b) in a pulsed flame.

sensitivity of fs/ps VCARS is greatly reduced. Using a Princeton Instruments ProEM EMCCD camera and 12-cm^{-1} bandwidth $sinc^2$ probe pulse with delay of 2.8 ps, single-shot N_2 vibrational CARS spectra were recorded at 1 kHz over a range of temperatures. The measurements were performed in a well-characterized Hencken burner from Φ = 0.28–1.0 representing an adiabatic temperature range of ~1137–2382 K. The average and standard deviation of 1000 single-shot best-fit temperature measurements were used to determine the accuracy and precision of the measurement respectively, under steady-state conditions. The results are summarized in Fig. 4.5 where the bars represent the standard deviation associated with the measurement. Measurements at 500 Hz from Section 4.3 are included to aid in comparison.

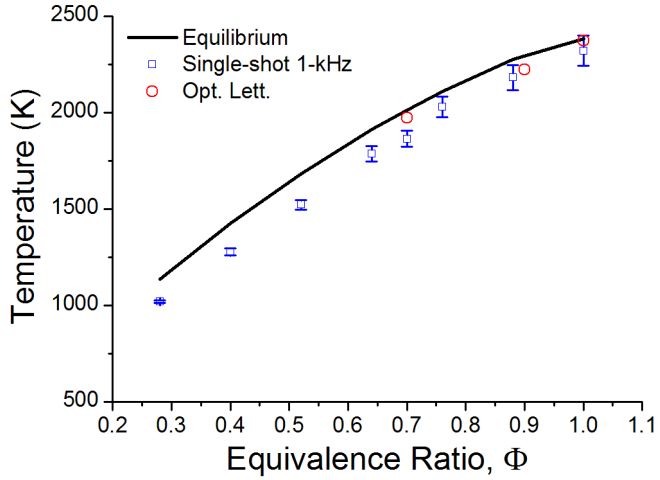

Figure 4.5. Average single-shot temperature as a function of equivalence ratio (open squares). The solid line is the calculated equilibrium temperature under adiabatic conditions, while the open circles are the data from Section 4.3 at 500 Hz. The error bars represent one standard deviation.

Two trends are apparent in Fig. 4.5. First, the accuracy of the measurements increases with temperature and, second, the precision decreases with temperature. This is highlighted in Fig. 4.6 which displays the accuracy and precision as a function of equilibrium temperature. Comparing these parameters with signal level and the ratio of the excited to ground state vibrational population, we find that the accuracy trends with the vibrational population in the excited vibrational state while precision trends with the signal-to-noise ratio (SNR).

This behavior is observed in the fs/ps VCARS spectra at 1425 K (Φ = 0.4) and 2382 K (Φ = 1.0) displayed in Fig. 4.7. At 1425 K, the ratio of the excited to ground vibrational transition signal is 1:55 with an SNR of 1742:1. In contrast, at 2382 K the ratio of the excited to ground vibrational transition signal is 1:4.5 with an SNR of 205:1. This represents

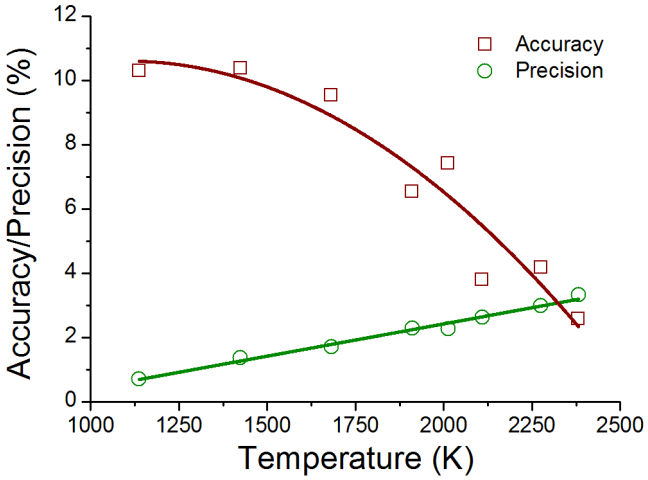

Figure 4.6. Accuracy and precision as a function of equilibrium temperature.

an increase in vibrational ratio of 12× and a decrease in SNR of 8.5× and corresponds to an increase in accuracy from 10.4% to 2.6% and decrease in precision from 1.4% to 3.3%. At low temperature, the small population in the excited vibrational state reduces the temperature sensitivity leading to decreased accuracy. Meanwhile, the signal-to-noise ratio increases at low temperature and therefore the precision increases. In contrast, at high temperature the excited state population increases thereby increasing temperature sensitivity and accuracy. However, the signal levels decrease with a corresponding decrease in precision.

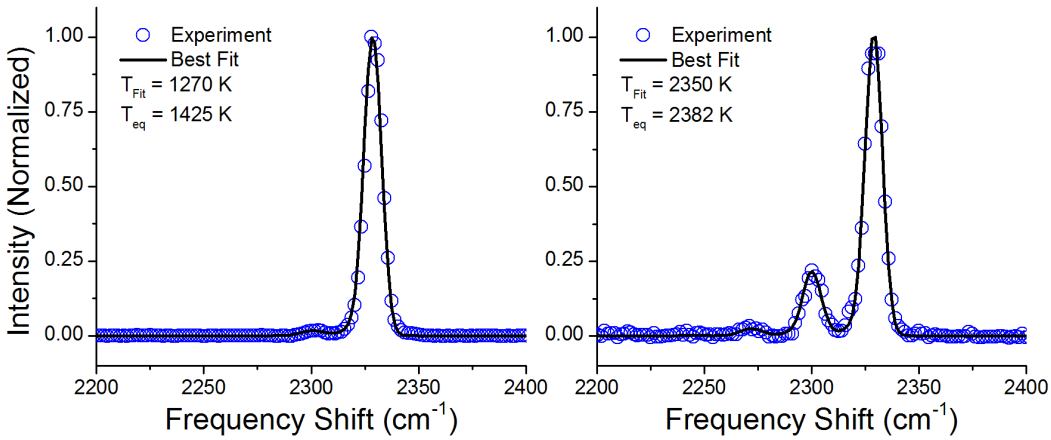

Figure 4.7. Single-shot N_2 fs/ps VCARS at 1425 K (left) and 2382 K (right).

In summary, we have demonstrated frequency-domain hybrid fs/ps CARS thermometry of N_2 at 500 Hz in high-temperature flames, enabling suppression of the nonresonant background by two orders of magnitude and an improvement in accuracy over previous high-speed fs CARS measurements. The high-speed CARS spectra exhibit temperature precision of better than 2.2% up to 2400 K, enabling real time detection of transients in unsteady flames. Additionally, the dependence of precision and accuracy on temperature was investigated from 1137–2382 K. The accuracy increases with increased temperature from 10.3–2.6% while precision decreases with increased temperature from 0.7–3.3%.

This work was supported, in part, by the National Research Council and the Air Force Office of Scientific Research. J. Miller was funded by the Department of Defense through the National Defense Science and Engineering Graduate Fellowship Program. The authors are grateful to S. Roy of Spectral Energies, LLC, to S. Danczyk and D. Talley of the Air Force Research Laboratory, and to C. Dedic and A. Vaidyanathan of Iowa State University for their assistance.

4.6 References

1. S. Roy, W. D. Kulatilaka, D. R. Richardson, R. P. Lucht, and J. R. Gord, "Gas-phase single-shot thermometry at 1 kHz using fs-CARS spectroscopy," *Opt. Lett.* **34**, 3857–3859 (2009).
2. T. X. Yi and E. J. Gutmark, "Combustion instabilities and control of a multiswirl atmospheric combustor," *J. Eng. Gas Turb. Power* **129**, 31–37 (2007).
3. S. Roy, J. R. Gord, and A. K. Patnaik, "Recent advances in coherent anti-Stokes Raman scattering spectroscopy: Fundamental developments and applications in reacting flows," *Prog. Energy Combust. Sci.* **36**, 280–306 (2010).

4. T. R. Meyer, S. Roy, and J. R. Gord, "Improving signal-to-interference ratio in rich hydrocarbon-air flames using picosecond coherent anti-stokes Raman scattering," *Appl. Spectrosc.* **61**, 1135–1140 (2007).
5. D. Pestov, X. Wang, D. Cristancho, K. R. Hall, A. V. Sokolov, and M. O. Scully, "Real-time sensing of gas phase mixtures via coherent Raman spectroscopy," Paper CTuI2, *Conference on Lasers & Electro-Optics*, May 4-9, 2008.
6. B. D. Prince, A. Chakraborty, B. M. Prince, and H. U. Stauffer, "Development of simultaneous frequency- and time-resolved coherent anti-Stokes Raman scattering for ultrafast detection of molecular Raman spectra," *J. Chem. Phys.* **125**, 044502 (2006).
7. R. D. Hancock, K. E. Bertagnolli, and R. P. Lucht, "Nitrogen and hydrogen CARS temperature measurements in a hydrogen/air flame using a near-adiabatic flat-flame burner," *Combust. and Flame* **109**, 323–331 (1997).

CHAPTER 5. PROBE PULSE OPTIMIZATION FOR NONRESONANT BACKGROUND SUPPRESSION IN HYBRID FEMTOSECOND/ PICOSECOND COHERENT ANTI-STOKES RAMAN SCATTERING AT HIGH TEMPERATURE

Modified from a paper published in *Optics Express* **19**, 13326–13333 (2011).

Joseph D. Miller,[1] Mikhail N. Slipchenko,[2] and Terrence R. Meyer[1,3]

Hybrid femtosecond/picosecond coherent anti-Stokes Raman scattering (fs/ps CARS) offers accurate thermometry at kHz rates for combustion diagnostics. In high-temperature flames, selection of probe-pulse characteristics is key to simultaneously optimizing signal-to-nonresonant-background ratio, signal strength, and spectral resolution. We demonstrate a simple method for enhancing signal-to-nonresonant-background ratio by using a narrowband Lorentzian filter to generate a time-asymmetric probe pulse with full-width-half-maximum (FWHM) pulse width of only 240 fs. This allows detection within just 310 fs after the Raman excitation for eliminating nonresonant background while retaining 45% of the resonant signal at 2000 K. The narrow linewidth is comparable to that of a time-symmetric $sinc^2$ probe pulse with a pulse width of ~2.4 ps generated with a conventional 4-*f* pulse shaper. This allows nonresonant-background-free, frequency-domain vibrational

[1] Department of Mechanical Engineering, Iowa State University, Ames, IA
[2] Weldon School of Biomedical Engineering, Purdue University, West Lafayette, IN
[3] SAOT, Erlangen Graduate School in Advanced Optical Technologies, University of Erlangen-Nuremberg, Erlangen, Germany

spectroscopy at high temperature, as verified using comparisons to a time-dependent theoretical fs/ps CARS model.

5.1 Introduction

Coherent anti-Stokes Raman scattering (CARS) spectroscopy has been widely employed for temperature and species concentration measurements in high-temperature combustion environments due to high signal collection efficiency, excellent chemical specificity, high spatial resolution, and noninvasive implementation [1-15]. Although CARS measurements have been obtained traditionally using nanosecond (ns) [1-7] and picosecond (ps) [8-15] laser sources, there is increased interest in the use of femtosecond (fs) laser pulses due to the availability of kHz-repetition-rate amplifiers with high peak power and the ability to monitor time-domain energy transfer phenomena [16-22].

One of the challenges of implementing CARS diagnostics in practical combustion systems is the high nonresonant susceptibility of hydrocarbon species that can lead to significant background interference, thus reducing accuracy and sensitivity [3-6]. Strategies for reducing nonresonant background using polarization discrimination have been successfully employed in ns CARS, but these strategies incur a large reduction in the CARS signal and pose challenges in high-pressure, windowed combustors due to polarization scrambling [1, 7]. In ps and fs CARS, an alternative, time-based discrimination technique can be used to separate the resonant and nonresonant CARS signals due to the long time decay of the resonant signal relative to the decay of the nonresonant contribution [8-12, 14-16, 18-29].

Recently, we have demonstrated kHz-rate CARS thermometry utilizing a hybrid fs/ps CARS technique [23], which allows effective elimination of nonresonant background by time discrimination and enhances accuracy over previous time-domain high-repetition-rate CARS measurements [22]. As shown in the energy-level diagram of Fig. 5.1(a), broadband fs pump (ω_1) and Stokes (ω_2) pulses are tuned to the N_2 vibrational band near 2330 cm^{-1}. A narrowband probe pulse (ω_3) is then used to generate the spectrally resolved vibrational CARS signal (ω_{CARS}). In the time domain, shown in Fig. 5.1(b), the probe pulse is delayed in time to avoid overlap with the pump and Stokes pulses and, therefore, avoid the generation of nonresonant background. Previously, the hybrid fs/ps CARS technique utilized a pulse-stretched probe pulse derived from the fs laser system by means of a 4-*f* pulse shaper [23, 25-27], which results in a spectrally narrowed flat-top profile. In the time domain, a spectrally narrowed flat-top profile corresponds to a temporally broadened $sinc^2$ profile, as shown schematically in Fig. 5.1(b). Because of the multiple maxima and minima in the $sinc^2$ temporal pulse shape, precise timing (τ_{4f} in Fig. 5.1(b)) between the pump, Stokes, and probe pulses is required for effective nonresonant background suppression. Recently, a high-precision narrow-spaced etalon was used to generate a Lorentzian spectral pulse profile to deeply suppress nonresonant background in broadband vibrational sum-frequency generation (SFG) spectroscopy [28]. A similar approach has been implemented for CARS of liquid and biological samples [29]. As shown in Fig. 5.1(b), this pulse profile produces an asymmetric temporal pulse shape with a step-rise and exponential decay and may be useful as a probe pulse for hybrid fs/ps CARS thermometry.

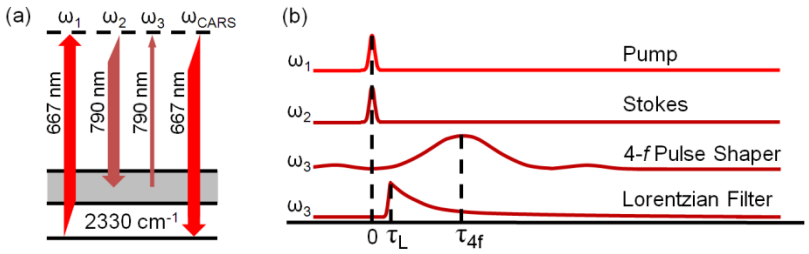

Figure 5.1. (a) Energy diagram for hybrid fs/ps CARS illustrating spectral characteristics of pump (ω_1), Stokes (ω_2), probe (ω_3), and CARS (ω_{CARS}) beams, and (b) timing diagram illustrating temporal lineshapes generated with 4-*f* pulse shaper and Lorentzian filter with respective delays of τ_{4f} and τ_L.

The goal of this work is to study the effects of probe-pulse lineshape and temporal profile on the time-resolved dynamics of nonresonant and resonant hybrid fs/ps CARS signals at high temperatures near 2000 K. Due to fast frequency-spread dephasing, the resonant N_2 CARS signal after the initial fs pump/Stokes excitation can decay much more quickly at high temperature [19, 20]. As shown in Fig. 5.1(b), a much smaller delay (τ_L) could be used with a Lorentzian lineshape to suppress nonresonant background while maximizing the resonant signal. The short time delay may also help avoid effects of collisional dephasing at higher pressures. Hence, the temporal characteristics of several probe pulses and their effects on nonresonant background suppression, signal strength, and spectral resolution are investigated. In particular, it is of interest to determine if a time-asymmetric probe pulse produced using a narrowband Lorentzian filter can improve nonresonant background suppression as compared to narrowband time-symmetric sinc^2 probe pulses generated using a conventional 4-*f* pulse shaper. Moreover, with recent advances in coating technology, a narrowband high-damage-threshold filter can become a cost-effective solution for the generation of a spectrally narrowband Lorentzian probe-pulse profile.

5.2 Comparison of Pulse-Shaping Strategies

In the hybrid fs/ps CARS system employed for the current work, a regeneratively amplified Ti:sapphire laser (Solstice, Spectra Physics) with a 100-fs output pulse at 790 nm is used to pump an optical parametric amplifier (OPA) (TOPAS, Spectra Physics) to produce frequency-doubled signal at 667 nm. The CARS 50-μJ pump (ω_1 = 14990 cm^{-1} with $\Delta\omega \approx$ 150 cm^{-1}) and 450-μJ Stokes (ω_2 = 12660 cm^{-1} with $\Delta\omega \approx$ 150 cm^{-1}) preparation pulses are temporally and spatially overlapped to excite ro-vibrational transitions in the N_2 molecule near 2330 cm^{-1}, as shown in Fig. 5.1(a). A pulse-shaped narrowband probe beam at 790 nm interacts with the vibrational coherence through the BOXCARS phase-matching configuration [30] and generates a CARS beam which carries the spectral signature of the N_2 ro-vibrational energy distribution. The probe pulse can be temporally delayed (τ in Fig. 5.1(b)) via a high-resolution motorized delay stage (ILS150PP, Newport). This allows the timing of the frequency-domain CARS spectrum to be varied with respect to the Raman excitation. The CARS spectra are recorded with a 0.303-m spectrometer (Shamrock SR-303i, Andor) utilizing a 1200 line/mm grating and an electron-multiplying, charge-coupled device (EMCCD) camera (ProEM, Princeton Instruments), resulting in an effective resolution of ~0.3 nm.

Three different probe pulses are employed to study the effects of pulse shape on the time- and frequency-domain dynamics of resonant and nonresonant CARS signals. The first two probe pulses are generated using a folded 4-*f* pulse shaper. As shown in Fig. 5.2(a), a broadband fundamental pulse at 790 nm, which exhibits a near Gaussian profile, is dispersed in space via an 1800 line/mm grating with a 500-nm blaze angle (10HG1800-500-1, Newport) and then focused onto a mirror by a 300-mm cylindrical lens. An adjustable square

slit placed on the surface of the mirror acts as a flat-top spectral filter in the frequency domain, allowing the linewidth to be arbitrarily selected. As the pulse is reflected back to the grating, it is recombined into a circular beam and used as the CARS probe pulse. In the current study, slit widths of 850 μm and 400 μm are used to generate FWHM spectral linewidths of Γ~12 cm^{-1} and ~6.5 cm^{-1}, respectively. The overall throughput of the 4-*f* pulse shaper at 790 nm is 3.2% for the 850-μm slit and 1.5% for the 400-μm slit.

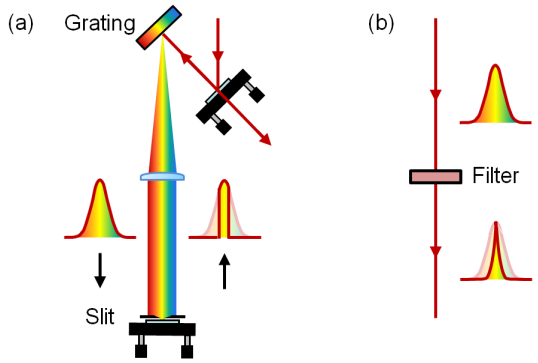

Figure 5.2. Schematic diagram of (a) folded 4-*f* pulse shaper utilizing square slit, and (b) drop-in filter producing Lorentzian lineshape.

The third probe lineshape is generated by a "drop-in" narrowband Lorentzian spectral filter (OS004308, Chroma), as shown in Fig. 5.2(b). This filter can be angle tuned with an overall throughput of 1.5% near 790 nm, resulting in a FWHM spectral linewidth of Γ ~13 cm^{-1}. The 850-μm slit was chosen to be identical to that used in our previous work [23], which showed sufficient resolution for high-temperature thermometry of N_2. The Lorentzian filter was then chosen to have a similar spectral bandwidth, and the 400-μm slit was used to study the effect of resolution enhancement by a factor of ~2.

5.3 Nonresonant Suppression

The measured spectral lineshapes are plotted in Fig. 5.3(a) for all three probe pulses. As is well known, the spectral lineshape is directly related to the time-domain lineshape by way of the Fourier Transform. For the 4-*f* pulse shaper with a square slit, the Fourier Transform is a sinc^2 function that exhibits several side bands of decreasing intensity in time. This time profile is shown in Fig. 5.3(b), which plots a cross-correlation of the 100-fs pump and Stokes pulses with the three ps probe pulses using nonresonant signals. Fourier Transforms of the sinc^2 time-domain cross-correlations in Fig. 5.3(b) result in spectral linewidths within 3.2% of the frequency-domain measurements. This slight disagreement can be expected since the frequency domain does not exhibit a true flat-top spectral profile but is distorted due to the spectral profile of the broadband fundamental beam.

The Lorentzian filter has a FWHM of 13 cm^{-1}, as shown in Fig. 5.3(a). This is close to the 12-cm^{-1} linewidth of the 850-μm slit used previously for kHz-rate thermometry [23], but with characteristic wings near the baseline. In the time-domain, shown in Fig. 5.3(b), this profile exhibits an asymmetric lineshape that rises quickly as the Gaussian convolution of the 100-fs pump and Stokes pulses [28], then decays exponentially with a time constant of ~0.43 ps.

The time-asymmetric profile results from the interference filter which (in its simplest form) acts as a Fabry-Pérot etalon in the small gap limit. In this case, the temporal train of pulses emitting from the filter as a result of multiple reflections overlap, producing a temporal output with a nearly exponential decay [28]. The Fourier Transform of this exponential decay results in the familiar Lorentzian lineshape. The time-domain Lorentzian pulse exhibits a FWHM of 240 fs, which is an order of magnitude shorter than the FWHM of

2.36 ps for the sinc^2 pulse generated with the 4-*f* pulse shaper using an 850-μm slit. The fast rise exhibits a half-width at half maximum (HWHM) of ~110 fs, which is the critical parameter for achieving nonresonant background suppression with a short time delay from the pump and Stokes pulses. Hence, it should be possible to improve the signal-to-nonresonant-background ratio while maintaining a bandwidth of only 13 cm^{-1} for resolving the vibrational N_2 CARS spectrum.

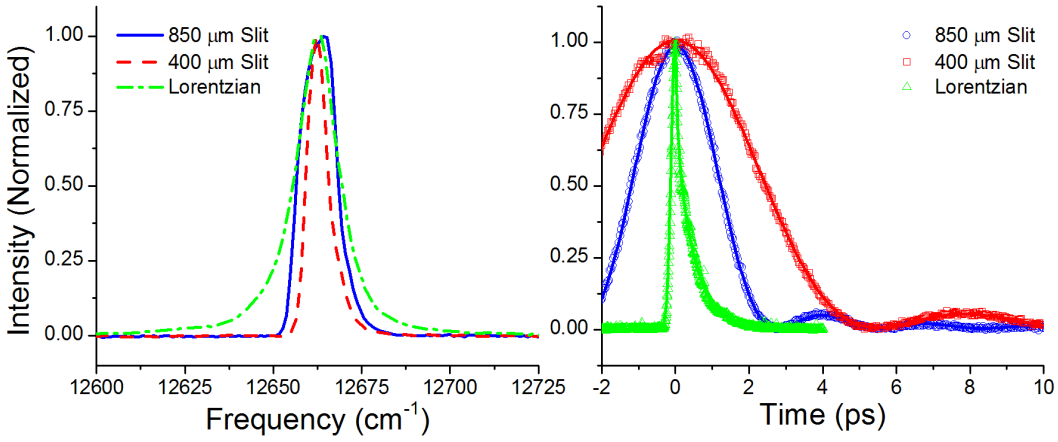

Figure 5.3. (a) Experimentally measured spectral lineshape and (b) normalized nonresonant background decay for 850-μm slit, 400-μm slit, and Lorentzian filter. Solid lines in (b) represent fits to the sinc^2 and exponential pulse profiles.

The resonant and nonresonant CARS signals at high temperature are compared in Fig. 5.4 as a function of probe delay for the sinc^2 probe pulses with slit widths of 850 μm and 400 μm and for the Lorentzian filter. The nonresonant background (time-reversed cross-correlation) was spectrally integrated from 2412 to 2432 cm^{-1} in an H_2–Air flame stabilized over a Hencken burner at 2000 K. The resonant CARS signal was spectrally integrated from 2310 to 2346 cm^{-1}, which represents the Δv = 0-1 vibrational band. The dashed lines in Fig. 5.4 represent the nearly-transform-limited best-fit sinc^2 and exponential functions for the

rectangular and Lorentzian spectral shapes respectively. Because of the asymmetric step rise and exponential time profile generated by the Lorentzian filter, a slight delay of ~310 fs in the probe timing results in a sharp drop in the nonresonant background signal to only 0.4% of the signal at time zero. This is essentially at the noise level of the current spectrally-resolved measurements. In contrast, the probes generated with the 4-*f* pulse shaper require delays of 2.77 ps and 5.5 ps to reach minimum nonresonant background levels of 0.39% and 0.65%, respectively, for the 850-μm and 400-μm slits.

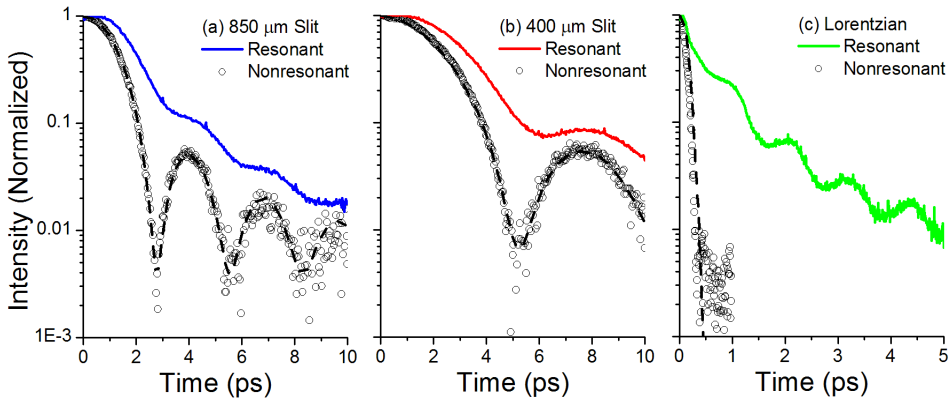

Figure 5.4. Comparison of resonant (v0 → v1) and nonresonant CARS intensity for 4-*f* pulse shaper with (a) 850-μm slit, (b) 400-μm slit, and (c) Lorentzian filter. Dashed lines are fit to experimental data (open symbols). Data are normalized to unity.

As noted earlier, the relatively short probe delay required for minimizing the nonresonant background signal for the asymmetric probe pulse is beneficial for maximizing the CARS signal at high-temperature conditions when the frequency-spread dephasing rate is highest. Hence, in addition to nonresonant background suppression, it is important to consider the signal-to-background ratio when optimizing the probe-pulse configuration. While the nonresonant background signal decays much faster for the Lorentzian probe pulse,

its short pulse width (~240 fs FWHM) also leads to a faster decay in the CARS signal as the probe is delayed in time. Overall there is an improvement in signal-to-background ratio as compared with the pulses generated using the 4-*f* pulse shaper. For the Lorentzian filter, the minimum nonresonant background at 310 fs corresponds to a resonant signal that is 44.6% of the signal at time zero, leading to a signal-to-background ratio of 112:1. This is in contrast to the 4-*f* pulse shaper with the 850-μm slit, which has a minimum nonresonant delay at 2.77 ps, where its resonant signal retains 19.4% of its value at time zero. This results in a signal-to-background ratio of 50:1. For the 4-*f* pulse shaper and the 400-μm slit, a minimum nonresonant background at 5.5 ps reduces the resonant signal to only 11.7% of the value at time zero, resulting in a signal-to-background ratio of 18:1.

5.4 Effect on Spectral Resolution

Note that the improved signal-to-background ratio of the Lorentzian filter compared with the 850-μm slit is achieved without sacrificing overall signal, as the reduced throughput from 3.2% to 1.5% noted earlier is outweighed by the increase in relative signal from 19.4% to 44.6%. Hence, the current Lorentzian filter may offer an optimal balance of nonresonant suppression, signal strength, and spectral resolution. Further improvement in signal-to-background ratio using a Lorentzian filter with a more narrowed spectral profile and a longer exponential time decay may be possible. However, further reduction in throughput is unlikely to be offset by an increase in relative resonant CARS signal, which is an important consideration for single-shot CARS measurements. The effects of nonresonant-background suppression and probe pulse shape on the spectrally-resolved CARS signals are shown in Fig. 5.5 at time zero and at probe delays required for minimum nonresonant background. As

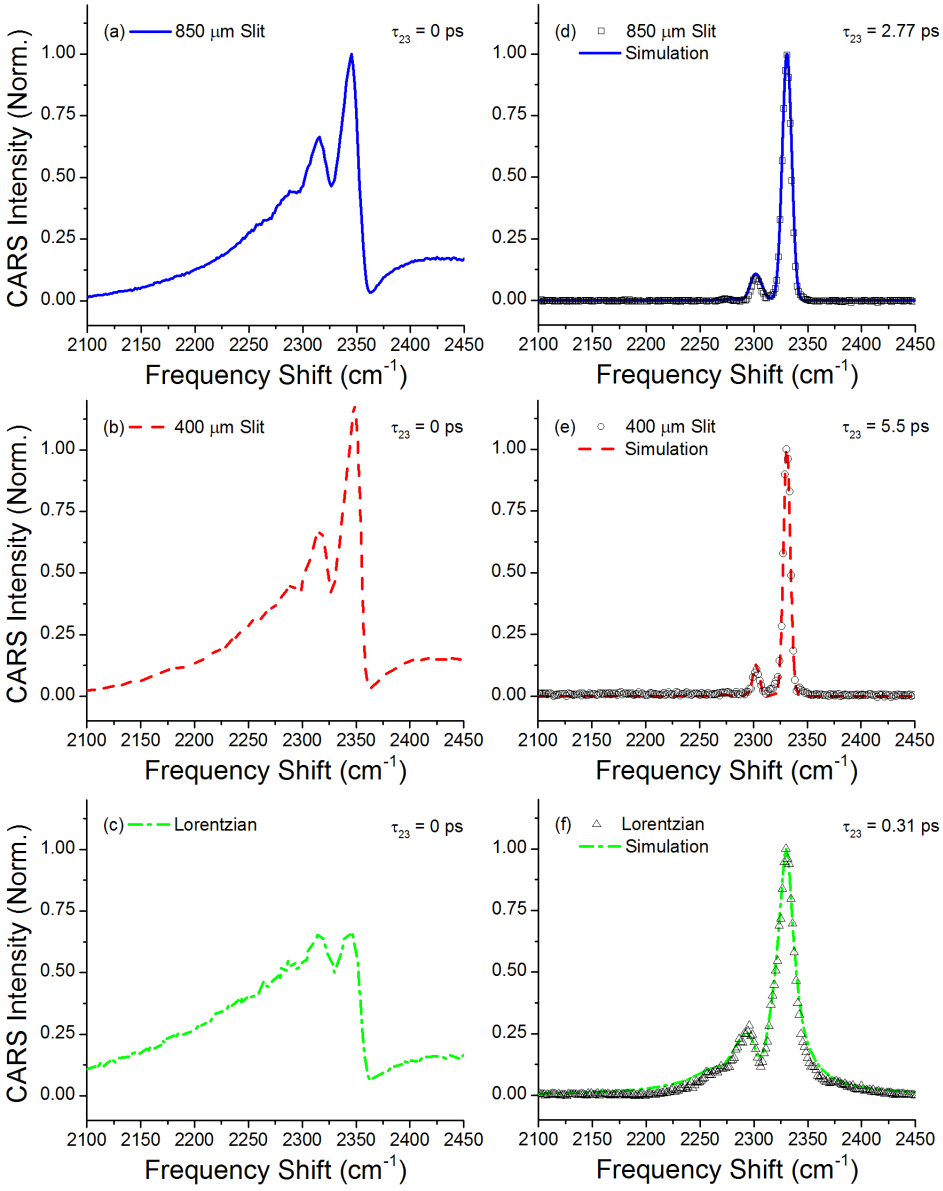

Figure 5.5. Comparison of spectrally resolved CARS signal for different probe pulse shapes. Left column represents experimental data collected at τ = 0 using (a) the 850-μm slit, (b) the 400-μm slit, and (c) the Lorentzian filter. Right column represents experimental data and simulations (2000 K) at (a) τ = 2.77 ps for the 850-μm slit, (b) τ = 5.5 ps for the 400-μm slit, and (c) τ = 0.31 ps for the Lorentzian filter. Data in (a-c) are normalized to unity and the nonresonant contribution of (a), while data and simulations in (d-f) are normalized to unity.

shown in Figs. 5.5(a-c), the relative effect of the nonresonant background is more severe for the 240-fs FWHM Lorentzian probe pulse due to strong overlap with the 100-fs pump and Stokes pulses. This background is nearly completely eliminated in the time delayed spectra of Figs. 5.5(d-f).

The ability to suppress the nonresonant contribution while still maintaining temperature sensitivity is an important consideration for probe-pulse optimization. Theoretical fits to experimental spectra obtained using $sinc^2$ probe pulses at high temperature were demonstrated in previous work [23]. In Fig. 5.5(f), it is shown that good agreement with the theoretical model can also be obtained with the time-asymmetric Lorentzian pulse shape while neglecting nonresonant contributions.

As noted earlier, the FWHM linewidth of the Lorentzian probe pulse (13 cm^{-1}) is similar to that of the $sinc^2$ probe pulse generated with the 850-μm slit (12 cm^{-1}). However, the wings of the Lorentzian lineshape, shown previously in Fig. 5.3(a), are quite broad and produce a 1.1-ps beat pattern in the time domain (see Fig. 5.4(c)) due to the ~30 cm^{-1} spacing of the vibrational transitions (see Fig. 5.5(a)). This interference seems to enhance the relatively weak signal in the hot band, potentially increasing sensitivity. A similar effect is produced by interference with the nonresonant background, as shown in Figs. 5.5(a-c). However, the nonresonant background can change from shot to shot in an unsteady gaseous flow field. In contrast, enhancement of the hot band from the wings of the Lorentzian probe pulse is achieved with an entirely predictable probe pulse lineshape. This enables reliable theoretical prediction of the time-dependent CARS spectrum, as shown in Fig. 5.5(f). Perhaps due to this signal enhancement, preliminary analyses near 2000 K using the current theoretical model suggests that the CARS signal generated with the Lorentzian probe pulse

exhibits the same temperature sensitivity as the fully-resolved, 6.5-cm^{-1} bandwidth probe pulse generated using the 400-μm slit. This is estimated from the change in the hot-band to fundamental-band ratio for a given change in temperature. Further increasing the slit width to 850 μm and beyond in an effort to improve the signal-to-background ratio progressively degrades sensitivity compared with the Lorentzian probe. Future work involves further analysis on whether this effect can enhance sensitivity over a broad range of temperatures by enhancing hot-band signal levels, particularly at lower temperature.

The time- and frequency-domain characteristics of resonant and nonresonant hybrid fs/ps N_2 CARS signals have been investigated as a function of probe-pulse characteristics. Time-symmetric probe pulses generated using a 4-*f* pulse shaper can be optimized for nonresonant background suppression with careful selection of timing and pulse width. However, improved signal-to-nonresonant-background ratio (~2.2×) is possible using a time-asymmetric probe pulse generated using an inexpensive, narrowband Lorentzian filter. Using a delay of just 310 fs, this approach can achieve nonresonant background suppression of ~250× while retaining 45% of the resonant CARS signal despite the high rate of frequency-spread dephasing at temperatures near 2000 K. The short time delay required for nonresonant suppression may also be advantageous for avoiding interferences and further signal decay at elevated pressure due to collisionally induced energy transfer. This is important for single-shot, kHz-rate detection and is achieved while preserving sufficient spectral sensitivity for thermometry in high-temperature flames. Comparison with a theoretical model demonstrates that it is possible to accurately model the experimental CARS spectra while assuming zero nonresonant background, thereby eliminating ad hoc correction procedures.

Funding was provided by the National Science Foundation (CBET-1056006, Dr. Arvind Atreya, Program Official) and the Air Force Office of Scientific Research (Dr. Mitat Birkan, Program Manager). Mr. Joseph Miller was supported by the National Science Foundation and National Defense Science and Engineering Graduate Fellowship Programs. The authors also thank Drs. Hans Stauffer and Sukesh Roy of Spectral Energies, LLC, and Drs. James Gord, Stephen Danczyk, and Douglas Talley of the Air Force Research Laboratory for helpful discussions.

5.5 References

1. A. C. Eckbreth, *Laser diagnostics for combustion temperature and species* (Abacus Press, 1988).
2. S. Roy, J. R. Gord, and A. Patnaik, "Recent advances in coherent anti-Stokes Raman scattering spectroscopy: Fundamental developements and applications in reacting flows," *Prog. Energ. Combust. Sci.* **36**, 280–306 (2010).
3. R. J. Hall, and L. R. Boedeker, "CARS thermometry in fuel-rich combustion zones," *Appl. Opt.* **23**, 1340–1346 (1984).
4. R. L. Farrow, R. P. Lucht, and L. A. Rahn, "Measurements of the nonresonant 3rd-order susceptibilities of gases using coherent anti-Stokes Raman spectroscopy," *J. Opt. Soc. Am. B* **4**, 1241–1246 (1987).
5. M. J. Cottereau, F. Grisch, and J. J. Marie, "CARS measurements of temperature and species concentrations in an IC engine," *Appl. Phys. B* **51**, 63–66 (1990).
6. A. C. Eckbreth, and R. J. Hall, "CARS concentration sensitivity with and without non-resonant background suppression," *Combust. Sci. Technol.* **25**, 175–192 (1981).
7. L. A. Rahn, L. J. Zych, and P. L. Mattern, "Background-free CARS studies of carbon monoxide in a flame," *Opt. Commun.* **30**, 249–252 (1979).
8. W. Zinth, "Transient coherent Raman-Scattering in the time and frequency domain," *Opt. Commun.* **34**, 479–482 (1980).
9. S. Roy, T. R. Meyer, and J. R. Gord, "Broadband coherent anti-Stokes Raman scattering spectroscopy of nitrogen using a picosecond modeless dye laser," *Opt. Lett.* **30**, 3222–3224 (2005).
10. S. Roy, T. R. Meyer, and J. R. Gord, "Time-resolved dynamics of resonant and nonresonant broadband picosecond coherent anti-Stokes Raman scattering signals," *Appl. Phys. Lett.* **87**, 264103 (2005).
11. T. R. Meyer, S. Roy, and J. R. Gord, "Improving signal-to-interference ratio in rich hydrocarbon-air flames using picosecond coherent anti-stokes Raman scattering," *Appl. Spectrosc.* **61**, 1135–1140 (2007).

12. H. U. Stauffer, W. D. Kulatilaka, P. S. Hsu, J. R. Gord, and S. Roy, "Gas-phase thermometry using delayed-probe-pulse picosecond coherent anti-Stokes Raman scattering spectra of H_2," *Appl. Opt.* **50**, A38–A48 (2011).
13. P. S. Hsu, A. K. Patnaik, J. R. Gord, T. R. Meyer, W. D. Kulatilaka, and S. Roy, "Investigation of optical fibers for coherent anti-Stokes Raman scattering (CARS) spectroscopy in reacting flows," *Exp. Fluids* **49**, 969–984 (2010).
14. T. Seeger, J. Kiefer, A. Leipertz, B. D. Patterson, C. J. Kliewer, and T. B. Settersten, "Picosecond time-resolved pure-rotational coherent anti-Stokes Raman spectroscopy for N_2 thermometry," *Opt. Lett.* **34**, 3755–3757 (2009).
15. T. Seeger, J. Kiefer, Y. Gao, B. D. Patterson, C. J. Kliewer, and T. B. Settersten, "Suppression of Raman-resonant interferences in rotational coherent anti-Stokes Raman spectroscopy using time-delayed picosecond probe pulses," *Opt. Lett.* **35**, 2040–2042 (2010).
16. P. Beaud, H. M. Frey, T. Lang, and M. Motzkus, "Flame thermometry by femtosecond CARS," *Chem. Phys. Lett.* **344**, 407–412 (2001).
17. T. Lang, M. Motzkus, H. M. Frey, and P. Beaud, "High resolution femtosecond coherent anti-Stokes Raman scattering: Determination of rotational constants, molecular anharmonicity, collisional line shifts, and temperature," *J. Chem. Phys.* **115**, 5418–5426 (2001).
18. M. O. Scully, G. W. Kattawar, R. P. Lucht, T. Opatrny, H. Pilloff, A. Rebane, A. V. Sokolov, and M. S. Zubairy, "FAST CARS: Engineering a laser spectroscopic technique for rapid identification of bacterial spores," *P. Natl. Acad. Sci. USA* **99**, 10994–11001 (2002).
19. R. P. Lucht, S. Roy, T. R. Meyer, and J. R. Gord, "Femtosecond coherent anti-Stokes Raman scattering measurement of gas temperatures from frequency-spread dephasing of the Raman coherence," *Appl. Phys. Lett.* **89**, 251112 (2006).
20. S. Roy, P. J. Kinnius, R. P. Lucht, and J. R. Gord, "Temperature measurements in reacting flows by time-resolved femtosecond coherent anti-Stokes Raman scattering (fs-CARS) spectroscopy," *Opt. Commun.* **281**, 319–325 (2008).
21. J. R. Gord, T. R. Meyer, and S. Roy, "Applications of ultrafast lasers for optical measurements in combusting flows," *Annu. Rev. Anal. Chem.* **1**, 663–687 (2008).
22. S. Roy, W. D. Kulatilaka, D. R. Richardson, R. P. Lucht, and J. R. Gord, "Gas-phase single-shot thermometry at 1 kHz using fs-CARS spectroscopy," *Opt. Lett.* **34**, 3857–3859 (2009).
23. J. D. Miller, M. N. Slipchenko, T. R. Meyer, H. U. Stauffer, and J. R. Gord, "Hybrid fs/ps coherent anti-Stokes Raman scattering for high-speed gas-phase thermometry," *Opt. Lett.* **35**, 2430–2432 (2010).
24. F. M. Kamga, and M. G. Sceats, "Pulse-sequenced coherent anti-Stokes Raman-scattering spectroscopy - method for suppression of the non-resonant background," *Opt. Lett.* **5**, 126–128 (1980).
25. B. D. Prince, A. Chakraborty, B. M. Prince, and H. U. Stauffer, "Development of simultaneous frequency- and time-resolved coherent anti-Stokes Raman scattering for ultrafast detection of molecular Raman spectra," *J. Chem. Phys.* **125**, 044502 (2006).

26. D. Pestov, X. Wang, D. Cristancho, K. R. Hall, A. V. Sokolov, and M. O. Scully, "Real-time sensing of gas phase mixtures via coherent Raman spectroscopy," *Conference on Lasers & Electro-Optics* **1-9**, 1471–1472 (2008).
27. D. Pestov, R. K. Murawski, G. O. Ariunbold, X. Wang, M. C. Zhi, A. V. Sokolov, V. A. Sautenkov, Y. V. Rostovtsev, A. Dogariu, Y. Huang, and M. O. Scully, "Optimizing the laser-pulse configuration for coherent Raman spectroscopy," *Science* **316**, 265–268 (2007).
28. A. Lagutchev, S. A. Hambir, and D. D. Dlott, "Nonresonant background suppression in broadband vibrational sum-frequency generation spectroscopy," *J. Phys. Chem. C* **111**, 13645–13647 (2007).
29. S. O. Konorov, M. W. Blades, and R. F. B. Turner, "Lorentzian amplitude and phase pulse shaping for nonresonant background suppression and enhanced spectral resolution in coherent anti-Stokes Raman scattering spectroscopy and microscopy," *Appl. Spectrosc.* **64**, 767–774 (2010).
30. A. C. Eckbreth, "BOXCARS: Crossed-beam phase-matched CARS generation in gases," *Appl. Phys. Lett.* **32**, 421–423 (1978).

CHAPTER 6. SINGLE-SHOT GAS-PHASE THERMOMETRY USING PURE-ROTATIONAL HYBRID FEMTOSECOND/PICOSECOND COHERENT ANTI-STOKES RAMAN SCATTERING

Modified from a paper published in *Optics Express* **19**, 15627–15640 (2011).

Joseph D. Miller,[1] Sukesh Roy,[2] Mikhail N. Slipchenko,[3] James R. Gord,[4]

and Terrence R. Meyer[1,5]

High-repetition-rate, single-laser-shot measurements are important for the investigation of unsteady flows where temperature and species concentrations can vary significantly. Here, we demonstrate single-shot, pure-rotational, hybrid femtosecond/picosecond coherent anti-Stokes Raman scattering (fs/ps RCARS) thermometry based on a kHz-rate fs laser source. Interferences that can affect nanosecond (ns) and ps CARS, such as nonresonant background and collisional dephasing, are eliminated by selecting an appropriate time delay between the 100-fs pump/Stokes pulses and the pulse-shaped 8.4-ps probe. A time- and frequency-domain theoretical model is introduced to account for rotational-level dependent collisional dephasing and indicates that the optimal probe-pulse time delay is 13.5 ps to 30 ps. This time delay allows for uncorrected best-fit N_2-RCARS temperature measurements with ~1%

[1] Department of Mechanical Engineering, Iowa State University, Ames, IA
[2] Spectral Energies, LLC, Dayton, OH
[3] Weldon School of Biomedical Engineering, Purdue University, West Lafayette, IN
[4] Air Force Research Laboratory, Propulsion Directorate, WPAFB, OH
[5] SAOT, Erlangen Graduate School in Advanced Optical Technologies, University of Erlangen-Nuremberg, Erlangen, Germany

accuracy. Hence, the hybrid fs/ps RCARS approach can be performed with kHz-rate laser sources while avoiding corrections that can be difficult to predict in unsteady flows.

6.1 Introduction

Coherent anti-Stokes Raman scattering (CARS) spectroscopy has found significant use in the measurement of gas-phase temperature and species concentration due to its ability to probe harsh environments and provide high spatio-temporal resolution in unsteady flows [1-3]. This technique utilizes a pump beam with frequency ω_1 and Stokes beam with frequency ω_2 to excite rotational or vibrational Raman resonances ($\omega_1 - \omega_2$) in a molecule. A probe pulse (ω_3) is then used to generate a coherent anti-Stokes signal ($\omega_1 - \omega_2 + \omega_3$) with a spectral fingerprint that is sensitive, in part, to temperature and species concentration. Excitation of high-energy vibrational resonances is often utilized for thermometry in combusting flows up to 3500 K [1]. In low-temperature unsteady flows, where physical probes would be ineffective, it is possible to excite well isolated hydrogen ro-vibrational transitions down to 300 K [4] or, more commonly, low-energy pure-rotational transitions of species such as oxygen and nitrogen. Examples of the latter include studies in turbulent boundary layers from 300 to 500 K [5] and pre-ignition in internal combustion engines from 400 to 700 K [6]. Other low-temperature applications that may benefit from the sensitivity of the rotational CARS technique include pyrolysis reactors from 600 to 800 K [7], biomass pretreatment systems from 500 to 600 K [8], and catalytic reformers from 400 to 700 K [9].

Unfortunately, high-power nanosecond (ns) laser sources required for single-shot detection are limited to ~10-30 Hz, a rate that is incapable of resolving the time-history of temperature or species concentrations in most unsteady flows. While offering excellent

spectral resolution for measuring multiple molecular species and temperature [4, 10], ns-CARS signals are also subject to interferences from nonresonant background [11] and molecular collisions [12] that can vary with temperature, density, and chemical composition. This is a source of uncertainty for single-shot measurements in unsteady flows.

Several developments in CARS spectroscopy in recent years have focused on alleviating these weaknesses. For example, picosecond (ps) CARS with ~100-ps pulses has been introduced to suppress nonresonant background [13-19]. This is achieved by temporally separating the probe pulse from the pump and Stokes preparation pulses during the sub-ns coherence lifetime of the Raman resonance. This allows nonresonant background suppression by three orders of magnitude while maintaining excellent CARS signal levels and spectral resolution for frequency-domain detection and analysis [13-19]. A potential weakness of this approach is that probe delays in excess of 100 ps are required to suppress nonresonant interferences, which allows sufficient time for the spectra to become sensitive to collisional energy transfer, especially at lower temperature [17-19]. These effects create an apparent shift in temperature due to rotational-level-dependent dephasing rates [17-19], which may be difficult to model in unsteady flows with time-varying species concentrations. In addition to sensitivity to collisions, high-power ps lasers for single-shot detection have low repetition rates (~10-30 Hz) similar to that of ns lasers.

In contrast to the high spectral resolution of ns- and ps-CARS systems, time-domain CARS signals can be acquired using kHz-rate ultrafast lasers with pulse widths on the order of 100 fs. Instead of frequency-domain detection of the molecular distribution, the time-dependent molecular response is resolved by temporally delaying the CARS probe from the initial Raman resonance induced by the pump and Stokes pulses [1, 20-26]. By utilizing the

slope of the initial decay of the CARS signal due to frequency-spread dephasing, it is possible to extract gas-phase temperatures without interferences from collisional energy transfer [23-26]. Initial measurements utilized a slow-scan mechanical delay stage to probe the ro-vibrational Raman coherence at various time delays relative to the initial impulsive excitation [23, 24]. Subsequent efforts employed a chirped probe pulse to instantaneously encode the time decay into the spectral domain for single-shot, time-domain thermometry using a spectrometer [25]. However, this approach is highly sensitive to the probe pulse shape and phase, which should be characterized in great detail for accurate measurements. Hence, spectral modeling for single-shot, chirped-probe fs CARS thermometry can be complicated by several factors, including nonresonant interferences (used to increase signal strength) [25], interferences from resonant modes of multiple species [26], and the presence of density gradients or test cell windows that may alter the characteristics of the probe pulse. Current research is attempting to address these challenges using advanced pulse shaping, calibration, and characterization techniques [27]. For pure rotational spectra, however, the complexity can increase significantly because many molecules are probed simultaneously [17].

In an effort to exploit the advantages of both time- and frequency-resolved spectroscopy and utilize the high (kHz) repetition rate of ultrafast amplifiers, Miller *et al.* [28] have investigated the use of hybrid fs/ps CARS for gas-phase thermometry. By using 100-fs pulses to excite multiple molecular transitions and then probing the molecular response in the frequency domain using a 1–10 ps probe pulse, nonresonant and collisional interferences can be avoided through time-delayed detection. However, sufficient spectral resolution is maintained in the transform-limited, ps probe pulse for detection of multiple

species with much reduced sensitivity to probe-pulse characteristics [29]. In the case of vibrational hybrid fs/ps CARS, the temperature sensitivity is derived from the relative ratio of the fundamental and first-excited vibrational transitions [28]. As a result, the technique is only sensitive at temperatures where there is appreciable population in the excited vibrational states, thus limiting the technique to ~1200 K and higher [1]. In contrast, rotational CARS derives its temperature sensitivity from the distribution of rotational energy states, primarily in the ground vibrational state, which are active even at very low temperatures near 300 K [17]. In addition, rotational CARS can potentially be used to detect multiple species due to the broadband nature of the fs pump and Stokes pulses.

Therefore, the primary goal of the current work is to demonstrate the first use of single-laser-shot, hybrid fs/ps, pure-rotational CARS (fs/ps RCARS) for spectrally-resolved, collision- and nonresonant-background-free measurements of gas-phase temperature. Single-shot signal-to-noise ratios (SNR) of RCARS spectra are evaluated from 300 to 800 K using individual pulses from a kHz-rate fs laser amplifier. This approach has the potential to provide accurate kHz-rate thermometry with reduced sensitivity to probe-pulse characteristics at temperatures that are lower than that accessible using vibrational fs/ps CARS. We also present, to our knowledge, the first demonstration and validation of a time- and frequency-resolved fs/ps RCARS model to account for rotational (*J*-level) dependent dephasing, as called for in the literature [18, 19]. Diatomic nitrogen is used as a sample molecule due to its abundance in air-breathing reactions and its wide use in gas-phase CARS thermometry. Direct measurement of *J*-level dependent collisional dephasing of N_2 in the range 13.5–100 ps is presented, which has not been feasible with previous ps-CARS measurements [16-19]. These are used to investigate the sensitivity of N_2-RCARS

temperature measurements to collisional energy transfer near 300 K, where *J*-level dependent dephasing is most prevalent.

6.2 Comparison with Theoretical Model

The fs/ps RCARS technique developed in the current work is a variation of degenerate four-wave mixing (DFWM), which utilizes both fs and ps laser pulses to generate frequency-resolved rotational CARS spectra. As shown in Fig. 6.1(a), the pump, ω_1, and Stokes, ω_2, pulses are degenerate and spectrally broad. When the pulses are temporally overlapped as in Fig. 6.1(b), the difference-frequency between the pump and Stokes results in a broad excitation bandwidth. The impulsive excitation of the Raman coherence is particularly effective due to the multiple photon pairs which can mix to form a single difference frequency [24]. The induced coherent Raman polarization decays in time according to the molecular response function and is detected using a spectrally-narrowed degenerate probe pulse, ω_3, which can be delayed in time, τ_{23}, from the pump and Stokes pulses. The RCARS signal with frequency $\omega_{CARS} = \omega_1 - \omega_2 + \omega_3$ is a function of both resonant and nonresonant contributions and propagates with wavevector $\mathbf{k_{CARS}} = \mathbf{k_1} - \mathbf{k_2} + \mathbf{k_3}$ dictated by conservation of momentum.

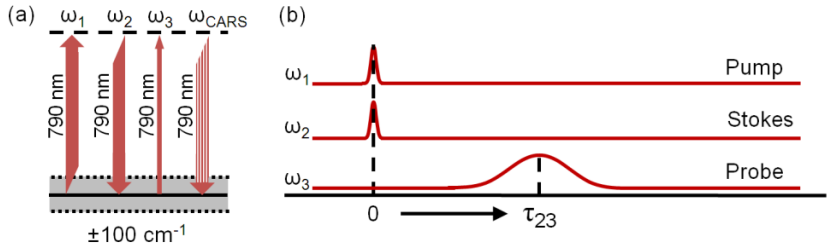

Figure 6.1. (a) Energy diagram for fs/ps RCARS illustrating spectral characteristics of pump (ω_1), Stokes (ω_2), probe (ω_3), and CARS (ω_{CARS}) beams, and (b) timing diagram of Gaussian probe-pulse generated by 4-*f* pulse shaper with time delay τ_{23} from pump and Stokes pulses.

A theoretical model for the pure-rotational hybrid fs/ps CARS spectra has been developed in accordance with the framework of Mukamel [30] based on previously published vibrational hybrid fs/ps CARS [28, 31] and fs/ps Raman induced Kerr effect spectroscopy (RIKES) models [32]. For a given probe delay, τ_{23}, the rotational CARS signal, I_{CARS}, is proportional to the absolute square of the summation of the resonant, P_{Res}, and nonresonant, P_{NR}, induced third-order polarization as given in Eq. (6.1),

$$I_{CARS}\left(t,\tau_{23}\right) \propto \left| P_{\mathrm{Res}}^{(3)}\left(t,\tau_{23}\right) + P_{N\mathrm{R}}^{(3)}\left(t,\tau_{23}\right)\right|^2 \tag{6.1}$$

where the CARS intensity is a function of time, t, and probe delay. The frequency-domain spectrum is recovered via a Fourier transform of $I_{CARS}(t)$ while the time dependence comes through τ_{23}. The nonresonant-induced third-order polarization is an important term during the temporal overlap of all three input beams, but may be neglected for delays τ_{23} > ~FWHM of the probe pulse [28, 29]. Neglecting the nonresonant term, the third-order polarization is given by Eq. (6.2),

$$\begin{aligned} P_{\mathrm{Res}}^{(3)}\left(t,\tau_{23}\right) = \left(\frac{i}{\hbar}\right)^3 \int_0^\infty dt_3 \int_0^\infty dt_2 \int_0^\infty dt_1 \Big[R\left(t_3,t_2,t_1\right) E_3\left(t-t_3\right) \\ \times E_2^*\left(t+\tau_{23}-t_3-t_2\right) E_1\left(t+\tau_{23}-t_3-t_2-t_1\right) e^{i(\omega_1-\omega_2+\omega_3)t_3} e^{i(\omega_1-\omega_2)t_2} e^{i\omega_1 t_1} \Big] \end{aligned} \tag{6.2}$$

where R is the molecular response function, E_1, E_2, and E_3 are the electric field envelopes for the pump, Stokes, and probe pulses, respectively, with carrier frequencies ω and associated coherence time scales t_1, t_2, and t_3. Because the individual pump, Stokes, probe, and CARS pulses are far from any resonant transitions, it can be assumed that the molecular response (electronic dephasing) is rapid with respect to variations in the pump and Stokes pulses during the integration of t_1 and the probe and CARS pulses during the integration of t_3 [28,

31]. In this case we can replace $R(t_3,t_2,t_1)$ with $\delta(t_3)R(t_2)\delta(t_1)$ and simplify the expression for the third-order polarization to Eq. (6.3),

$$P_{Res}^{(3)}(t,\tau_{23}) = \left(\frac{i}{\hbar}\right)^3 E_3(t)\int_0^\infty dt_2 \Big[R(t_2) E_2^*(t+\tau_{23}-t_2) \times E_1(t+\tau_{23}-t_2) e^{i(\omega_1-\omega_2)t_2} \Big] \tag{6.3}$$

where the integrated term is the convolution of the pump and Stokes pulses with the molecular response function. A phenomenological model is used to describe the molecular response function of nitrogen where each transition from state m to n is given a frequency, ω_{nm}, a collision-dominated Lorentzian linewidth, Γ_{nm}, and an intensity, I_{nm}, as in Eq. (6.4).

$$R(t) = \sum I_{nm}(T) e^{-i\omega_{nm}t - \Gamma_{nm}t} \tag{6.4}$$

For pure rotational S-branch transitions (Δv = 0 and ΔJ = +2), the frequency of each transition is defined as the difference between energy state $E_{v,J}$ and $E_{v,J+2}$. Each energy state is computed using fourth-order Herzberg molecular parameters accessible in the CARSFT molecular parameter files [33].

The intensity of each transition is calculated as a function of both the Raman transition cross-section, $(\partial\sigma/\partial\Omega)_J$, and the population difference, $\Delta\rho_{J,J+2}$, between the upper and lower energy states. The transition intensity and cross-section are given in Eq. (6.5) and Eq. (6.6),

$$I_{nm}(T) \propto \left(\frac{\partial\sigma}{\partial\Omega}\right)_J \Delta\rho_{J,J+2}(T) \tag{6.5}$$

$$\left(\frac{\partial\sigma}{\partial\Omega}\right)_J \propto \frac{4}{45} b_{J,J+2} (\gamma')^2 F(J) \tag{6.6}$$

where $b_{J,J+2}$ is the Placzek-Teller coefficient representing the overlap integral of the upper and lower energy state wavefunctions, γ' is the polarization anisotropy, and $F(J)$ is a correction term for centrifugal distortion [34]. This correction for vibrational-rotational interaction is the so-called Herman-Wallis factor [35] and is defined in the current model using the formulation of Martinsson as shown in Eq. (6.7),

$$F(J) = 1 + 4.448\left(\frac{2B_e}{\omega_e}\right)^2\left(J^2 + 3J + 3\right) \tag{6.7}$$

where B_e is the rotational constant, and ω_e is the vibrational frequency. Although this formulation has been recently questioned, the error associated with this assumption is minimal (<3 K) for the temperatures explored in the current work [35]. The population difference is a strong function of temperature, T, based on the Boltzmann distribution and also a function of the degeneracy of the lower energy state, J. For N_2, the rotational-nuclear degeneracy is dependent on J level and mass number and results in an intensity contrast between odd and even numbered rotational levels [36].

The linewidth term is theoretically a function of Doppler and collisional broadening. For pressures greater than 1 atm, N_2 linewidths are dominated by collisional broadening and thus the individual Q-branch linewidths are computed using the Modified Exponential Gap (MEG) model with parameters from Rahn and Palmer [37]. The approximation for the S-branch rotational transition linewidth [38] is shown in Eq. (6.8).

$$\Gamma_{J,J+2} \approx \frac{1}{2}\left(\Gamma_{J,J} + \Gamma_{J+2,J+2}\right) \tag{6.8}$$

The linewidth (FWHM) is inversely related to a temperature-dependent term which modifies the linewidth for low rotational levels and is linearly related to pressure. The linewidth of

each transition is especially important in temporally-resolved CARS techniques and it affects the decay in the CARS signal with increasing probe delay [16-19].

The optical Stark effect, which should be considered for ns CARS with high-intensity electric fields (~2 TW/cm^2·cm^{-1}) [39] is not included in the model. The total peak power used for single-shot measurements in the current work is ~0.5 TW/(cm^2·cm^{-1}). Also, for the nitrogen *S*-branch rotational transitions, Stark splitting can result in multiple lines with frequency shifts (~0.03 cm^{-1}) and beat frequencies (~1 ns) that are not detectable in the broadband, short-pulse arrangement of fs/ps RCARS.

The 1.6-W output of a regeneratively amplified ultrafast laser (Solstice, Spectra-Physics) with a nominal pulse width of 100 fs and diameter of 5 mm is divided into two beams using a thin-film polarizer with a 15:1 ratio, as shown in Fig. 6.2. The high-power beam is reserved for the probe pulse, while the low-power beam is used to produce the 45-μJ pump and Stokes pulses with an additional ultrafast 50/50 beam-splitter. A 2.1-cm^{-1} spectrally narrow probe pulse is generated using a folded 4-*f* pulse shaper with an adjustable square slit as previously reported by the authors [28, 29]. The overall throughput of the pulse shaper at this spectral resolution is less than 1% resulting in a probe pulse energy of 10 μJ.

The temporal delay between the pump and Stokes pulses is minimized and held constant, while the delay of the probe pulse is set using a high-resolution motorized delay stage (ILS-150-PP, Newport). The parallel-polarized pump, Stokes, and probe beams are focused into the heated probe volume using a BOXCARS phase-matching configuration [40] resulting in a cylindrical probe volume of 50-μm diameter and 1.1-mm length. To measure the diameter of the probe volume, a thin piece of aluminum is placed at the focal point and the hole produced by the beam is measured with a microscope. The interaction length is

measured by passing a thin glass slide (190 μm) along the length of the probe volume and recording the $1/e^2$ width of the resulting nonresonant signal. The CARS signal generated in N_2 is spatially filtered using an iris and focused into a 0.303-m spectrometer equipped with a 1200 line/mm grating (Shamrock SR-303i, Andor). The spectra are detected using an electron-multiplied charge-coupled device (EMCCD) camera capable of a 1-kHz non-EM acquisition rate and a 0.5-kHz rate in EM mode (DU-970P-UVB, Newton). The overall instrument resolution of the spectral detection system is measured to be 2.4 cm^{-1} at 790 nm.

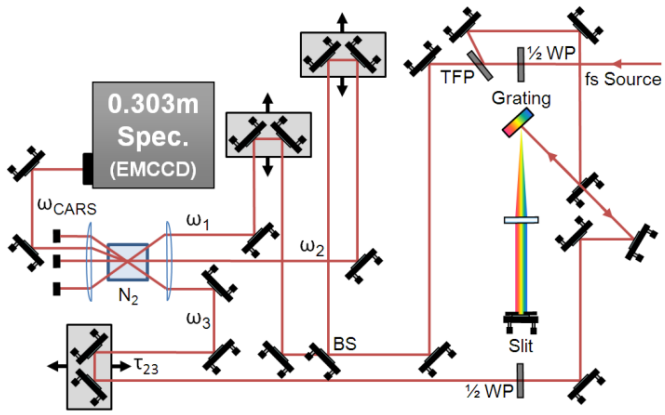

Figure 6.2. Experimental schematic of hybrid fs/ps RCARS system. WP: wave plate, TFP: thin-film polarizer, BS: ultrafast beam splitter, EMCCD: electron-multiplied charge-coupled device camera.

Nitrogen is heated using a 1500-W inline heating element and routed to a 0.75-inch diameter windowless cell. The flow rate for all conditions is 15 standard liters per minute to maximize heating and minimize flow disturbance. A K-type thermocouple (0.0625-inch-diameter) is inserted upstream of the cell and used to verify the nominal flow temperature after slight corrections for radiation heat transfer. Because the maximum heating

temperature is limited by cell design to 500 K, higher temperatures were measured in the exhaust of a stoichiometric H_2–air flame with N_2 dilution to control the temperature.

An important feature of hybrid fs/ps CARS is the generation of both fs and ps laser pulses using a single source. This setup is advantageous in that it ensures perfect synchronization between laser pulses and can be implemented in a straightforward manner. In the current work, a folded 4-*f* pulse shaper is used to produce a narrowed probe linewidth of ~2.1 cm^{-1} (FWHM) from the broadband fs source, as shown in Fig. 6.3(a). This resolution is sufficient for spectrally resolving individual rotational transitions of the N_2 molecule, which exhibit an average separation of ~8 cm^{-1}. The slightly asymmetric shape of the broadband source is accounted for in the theoretical modeling.

A cross-correlation of the probe pulse with the pump and Stokes pulses is recorded using nonresonant CARS signal in Argon. Unlike our previous work which used a $sinc^2$ lineshape, the current probe pulse exhibits a nearly transform-limited 8.4-ps Gaussian pulse shape in time, as shown in Fig. 6.3(b). A Gaussian pulse shape is advantageous over the $sinc^2$ profile since it does not exhibit the local minima and maxima associated with the $sinc^2$ pulse. Because of this, optimization of the probe-pulse delay for nonresonant suppression is simplified. To produce the nearly-Gaussian temporal pulse profile, the slit in the folded 4-*f* pulse shaper is slightly rotated such that the edges of the slit were no longer perpendicular to the direction of dispersion. At small slit widths, this acts to smooth the edges of the otherwise square spectral profile of the probe beam. The nearly Gaussian spectral profile is evident in Fig 6.3(a), which shows the convolution of the probe linewidth and instrument function.

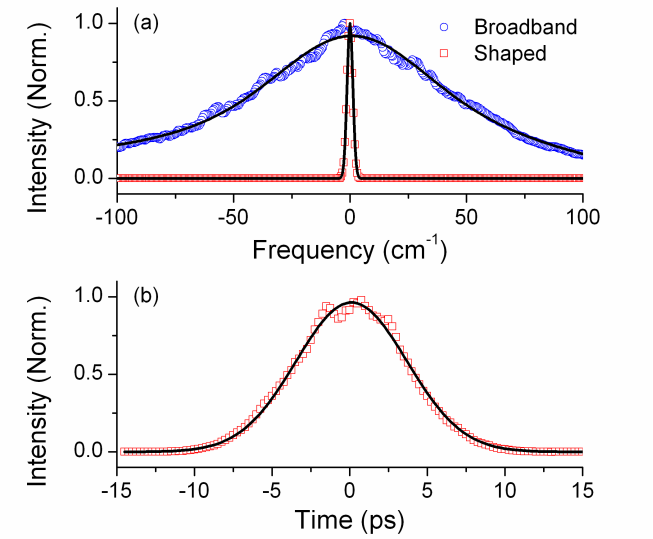

Figure 6.3. Experimentally measured (a) broadband pump/Stokes and narrowband probe lineshapes and (b) cross-correlation of nearly transform-limited shaped probe pulse. Solid lines are Gaussian fits to experimental data.

Experimental spectrally-resolved N_2 spectra at time zero and a delay τ_{23} = 13.5 ps are shown in Fig. 6.4 at 306 K. The spectrum at time zero is dominated by broad nonresonant background which must be modeled to accurately extract temperature and species concentration information. However, at a delay of 13.5 ps the nonresonant background has sufficiently decayed such that the spectrum is essentially nonresonant-background free. It is important to note that because the spacing between individual transitions is ~8 cm^{-1} for pure rotational *S*-branch transitions, the 2.1-cm^{-1} probe maintains sufficient spectral resolution to resolve individual transitions, thus spectral fitting is straightforward. The slight increase in the baseline of the delayed spectrum is due to a small overlap of the instrument function with adjacent transitions.

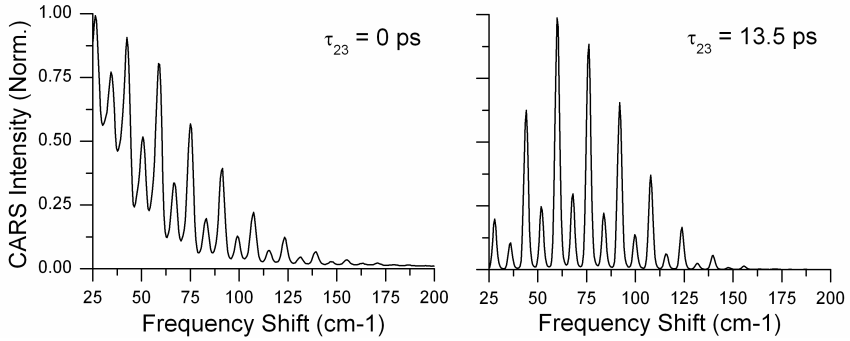

Figure 6.4. Experimental N_2 fs/ps RCARS spectra with 8.4-ps probe pulse delayed by 0 ps and 13.5 ps.

6.3 Influence of Collision Linewidth at Elevated Temperature

The time dynamics of the spectrally-integrated nonresonant signal from Argon and resonant signal from N_2 at 306 K and 500 K are given in Fig. 6.5. The open symbols represent experimental data points while the solid lines are simulations of the probe and resonant contributions as a function of time. Because the nonresonant contribution decays rapidly with respect to variations in the pump, Stokes and probe pulses, the nonresonant signal persists for only the duration of the probe pulse. The resonant signal in Fig. 6.5 is long lasting and displays a characteristic exponential decay. The rate of decay is highly dependent on internal energy transfer through molecular collisions [16], and detection within the first few ps reduces sensitivity to collisional energy transfer and greatly simplifies spectral interpretation [17-19]. The simulations of the time-dependent fs/ps RCARS signal at 306 K and 500 K are generated using the model described in the Theory section. The magnitude of the simulated data is adjusted to match the experimental intensities, although no adjustment was necessary for the time decay. Good agreement is found between the experimental and

simulated time decays, with fs/ps RCARS exhibiting a relative signal-to-nonresonant-background ratio of ~800:1 at 13.5 ps for 306 K and 500 K.

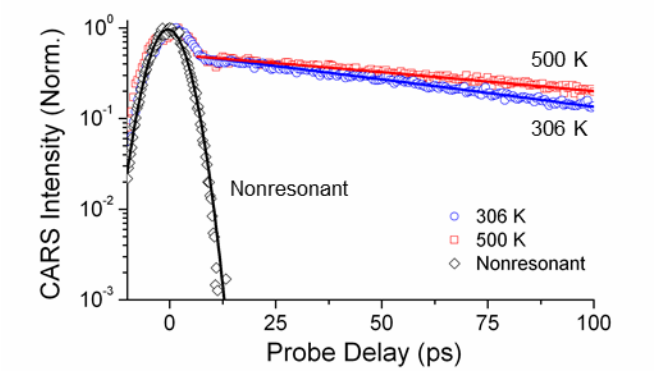

Figure 6.5. Normalized spectrally integrated fs/ps RCARS signal for nonresonant signal in Ar and spectrally-integrated resonant signal in pure N_2 at 306 K and 500 K. Open symbols represent experimental data and solid lines represent simulations.

The decay time constant of the rotational CARS spectra increases with an increase in temperature in accordance with a decrease in the linewidth [18,37]. This is in contrast to that observed for vibrational Q-branch CARS time-domain signals that decay more rapidly at higher temperature due to frequency-spread dephasing after the impulsive excitation [23]. Although the fs/ps RCARS signal normalized relative to time zero increases with temperature (see Fig. 6.5), the absolute signal decreases due to a drop in density and, therefore, N_2 concentration.

Although nonresonant suppression is not unique to fs/ps CARS [13-15, 18], the advantage of fs/ps RCARS over pure fs CARS or pure ps CARS is the ability to achieve three orders of magnitude nonresonant suppression at sufficiently short probe delays for minimizing collisional effects, especially near 13.5 ps, while maintaining spectral resolution

for frequency-domain detection. According to the data in Fig. 6.5, changes in the rate of collisional energy transfer from 306 K to 500 K are only significant beyond ~30 ps for the atmospheric-pressure conditions in this study.

It is well known that collisions between molecules can cause internal energy transfer which acts to decrease population of a given state as a function of time [37]. In the time domain, this manifests itself as a decrease in CARS signal strength as a function of time [41]. The decay rate is a strong function of thermodynamic properties, such as temperature, pressure, and molecular composition, that dictate the rate of collisions. The MEG model linearly relates the decay rate and pressure, while a more complex inverse relationship is given for the temperature and decay rate. In this way, for a given pressure the fastest rate of collisional energy transfer occurs at the lowest temperature, which is typically room temperature for many practical devices of interest. Additionally, the MEG model's assumption of an exponential relationship between the rate of energy transfer and the energy difference between the initial and final states results in a decrease in the rate of energy transfer at higher rotational energy states [37]. This is due to the increased angular momentum of higher J levels, which take longer to decay. The FWHM of the spectral linewidth can be calculated from the time constant of the exponential decay using the formulation of Kulatilaka *et al.* [16] and is given as Eq. (6.9),

$$\Gamma_J = \frac{1}{2\pi c \tau_{CARS,J}} \tag{6.9}$$

where Γ_J is the spectral linewidth in m^{-1} of the transition with initial state J, $\tau_{CARS,J}$ is the time constant in seconds of a single-exponential function for the same transition, and c is the speed of light in m/s.

In traditional frequency-domain spectroscopy, the exponential decay of the CARS signal as a function of time is used to determine the spectral linewidth. The spectral shape takes the form of a Lorentzian function, the Fourier transform of the exponential decay. While fully frequency-domain techniques must model only the spectral linewidth effect of collisional energy transfer, time-domain spectroscopic techniques are directly sensitive to time-dependent signal decay. For both temporally- and spectrally-resolved techniques (ps RCARS or fs/ps RCARS) the collisional energy transfer is manifest in both domains. Experimentally measured spectra at 306 K and probe delays of 13.5 ps (typical of fs/ps RCARS) and 300 ps (typical of ps RCARS) are given in the inset of Fig. 6.6. Each spectrum is normalized to unity. Because the high *J*-level transitions experience a relatively slower decay at room temperature as compared to the low *J* levels, the spectrally-detected signal appears to shift to higher frequencies and therefore higher temperature. The intensity of each transition can be independently analyzed as a function of time and fit using a single exponential decay, as shown in Fig. 6.6(a).

The difference in decay rate is easily observed for the $J = 6$ and $J = 14$ transitions. Because of the temporal and spectral resolution, the decay rate of each transition can be measured and the experimental linewidth computed using Eq. (6.6). The resulting spectral linewidths are plotted as a function of *J* level for N_2-N_2 collisions at 306 K in Fig. 6.6(b). The measured linewidths agree well with the published *Q*-branch data from Rahn and Palmer [37] utilizing the approximation for *S*-branch transitions [38].

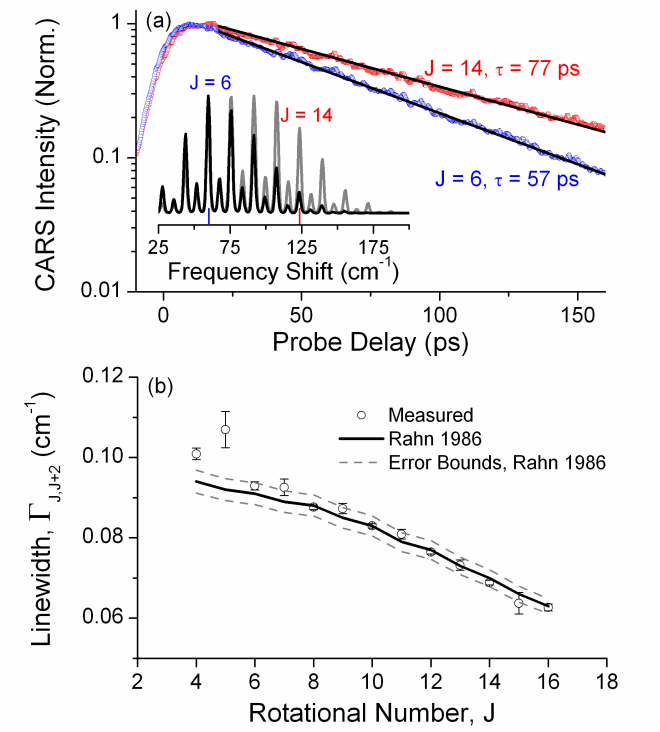

Figure 6.6. Direct time-domain measurement of *J-level* dependent collisional linewidths at 306 K. (a) Experimental data for $J = 6$ and $J = 14$ transitions along with best-fit single-exponential decays. Inset illustrates perceived shift of fs/ps RCARS spectra to higher temperature from probe delay of 13.5 to 300 ps. (b) Measured linewidth for each transition and published linewidth from Ref. 37. Error bars represent 95% confidence interval for exponential fit.

For ps RCARS, the perceived spectral shift can lead to a thermometry error of 46% at 360 ps, the time delay used in Ref. 18, if the *J*-level dependent decay is not considered. The ability to neglect the effect of collisional energy transfer greatly simplifies the spectral simulation process and may reduce uncertainty in the measurement. For this reason, it is important to consider the accuracy of collision-free fs/ps RCARS temperature measurements as a function of probe delay. The best-fit temperatures for spectra at 306 K and 500 K are given in Fig. 6.7(a) as a function of probe delay both including (squares) and neglecting (circles) the time-dynamics of *J*-level dependent collisional linewidth. The corresponding

error is plotted for both temperatures in Fig. 6.7(b). As expected, the full model which incorporates the collisional linewidth for each transition computes the temperature within 1% from 13.5 to 100 ps at both temperatures. If collisional energy transfer is neglected, the temperature bias at 306 K would reach 10% at 100 ps. For probe delays of ~150 ps or greater, typical of previous ps CARS measurements [18], the temperature bias is ~30% or greater and can lead to significant uncertainty if the gas temperature, density, or composition is varying in time. Because the effect of collisional energy transfer decreases with increased temperature, these effects may be ignored at high-temperature. However, for 300-500 K, it is anticipated that ps CARS measurements with ~100-ps pulses will require corrections of at least 10-30% due to collisional effects.

For probe delays less than 30 ps, however, there is no statistically significant difference between the collision-dependent and collision-free temperature measurements down to 300 K, which exhibit an error of ~1%. At atmospheric pressure, therefore, fs/ps RCARS thermometry can be performed while neglecting collisional energy transfer for temperatures greater than 300 K and probe delays less than 30 ps. This has implications for proper selection of the probe pulse delay. For nonresonant-free (~1000× reduction) and collision-free (<1% error) measurements, the delay is limited to 13.5–30 ps in the current work. If systematic errors up to 2.5% and nonresonant contributions of 1% are acceptable, this interval could be extended to 10.5–50 ps. On the other hand, the range for collision-free measurements may be reduced at high pressure.

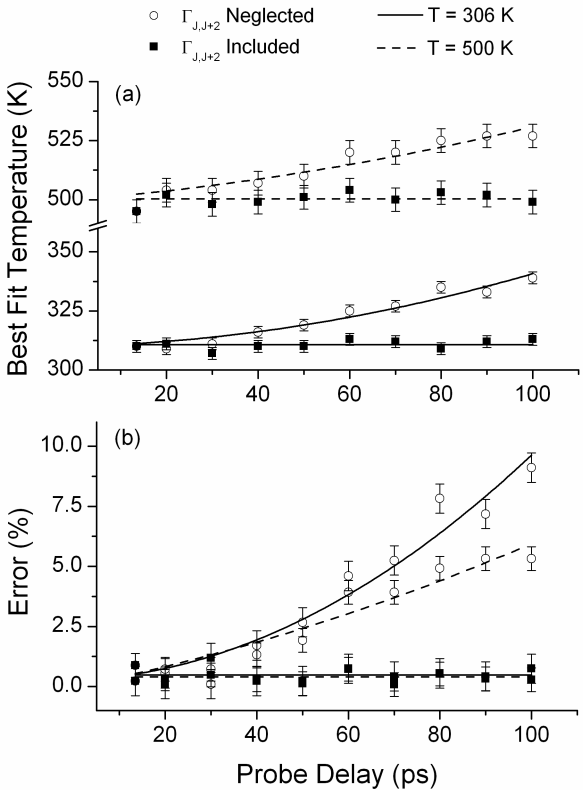

Figure 6.7. (a) Best-fit temperature and (b) associated percent error as a function of probe delay for simulations with (solid squares) and without (open circles) time-dependent collisional energy transfer at 306 K and 500 K. Error bars represent 1% uncertainty based on the data.

6.4 Single-Shot Thermometry

A significant advantage of fs/ps RCARS is the kHz repetition rate associated with ultrafast regenerative amplifiers, which is two to three orders of magnitude higher than current ns and ps sources used in CARS systems. To take advantage of the high repetition rates, accurate measurements must be possible using a single laser shot. An important factor when extracting temperature from an RCARS spectrum is the signal-to-noise ratio. The single-shot fs/ps RCARS spectra shown in Fig. 6.8 display an SNR of 3900:1 at 306 K, 425:1 at 500 K,

and 42:1 at 700 K. The residual is shown shifted by -0.1. A probe-pulse delay of 13.5 ps is used in all three cases, ensuring that the temperature bias due to collisions or nonresonant background is negligible. Hence, these spectra have sufficient SNR for best-fit temperatures to be extracted from the theoretical model with high accuracy. Single-shot spectra at 800 K were also collected while keeping all laser parameters constant, leading to an SNR of ~15:1 and representing the upper limit of single-shot temperature measurements for the current laser configuration. Application of this approach to higher temperatures by increasing the probe-pulse bandwidth (i.e., throughput of the 4-*f* pulse shaper) or by employing a laser with increased laser energy is the subject of future investigation.

Single-shot, collision- and nonresonant-background-free, pure-rotational hybrid fs/ps CARS thermometry of N_2 is demonstrated using a kHz-rate fs laser source. By delaying the 8.4-ps probe pulse by 13.5 ps after the arrival of the 100-fs pump and Stokes pulses, it is possible to achieve a signal-to-nonresonant-background ratio of 800:1. The current approach also allows direct measurements of *J*-level dependent dephasing rates in the range of 13.5 to 100 ps, which are used to show that measured temperatures are collision free (to within 1% or less) for probe delays below 30 ps at atmospheric pressure. Using a frequency- and time-domain model, best-fit temperatures for current RCARS spectra at a probe delay of 13.5 ps exhibit accuracies of ~1% in the range of 306 K to 700 K without the need for corrections due to nonresonant background or collisions. This model is also used to show that the temperature bias due to collisions (i.e., *J*-level dependent dephasing) can be corrected for probe delays beyond 30 ps. The temperature correction at 100 ps, for example, is ~10% near 300 K. This has important implications for the effects of collisions when using ps CARS with ~100-ps pulses; this approach can require probe delays of at least 150 ps to avoid

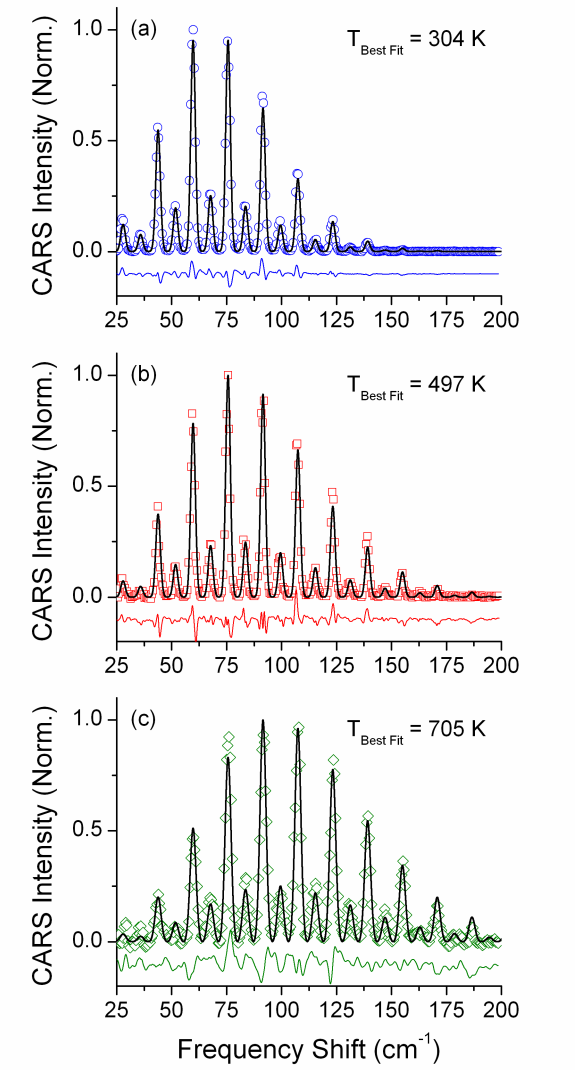

Figure 6.8. Single-shot pure-rotational hybrid fs/ps RCARS spectra of N_2 at (a) 306 K, (b) 500 K, and (c) 700 K. Open symbols represent experimental data while solid lines represent best fit simulations. Residual is shown shifted by -0.1.

nonresonant background, leading to temperature corrections of ~30% or more. Hence, the collision- and nonresonant-background-free fs/ps-RCARS approach can reduce uncertainty in unsteady flows where temperature, density, or composition may fluctuate in time. This is achieved using a kHz-rate fs laser source, although new amplified laser sources can

potentially allow measurements up to 10 kHz or beyond. Future work includes extension to higher temperatures using increased pulse energies and studies of collisional effects at higher pressure.

Funding was provided, in part, by the National Science Foundation (CBET-1056006, Dr. Arvind Atreya, Program Official), the Air Force Office of Scientific Research (Dr. Tatjana Curcic, Program Manager), and the Air Force Research Laboratory (AFRL) under Contract Nos. FA8650-09-C-2918 and FA8650-10-C-2008 (Ms. Amy Lynch, Program Manager). Equipment used for this work was funded, in part, by the Air Force Office of Scientific Research (Dr. Mitat Birkan, Program Manager). Joseph Miller was supported by the National Science Foundation and National Defense Science and Engineering Graduate Fellowship Programs. The authors also thank Dr. Hans Stauffer of Spectral Energies, LLC, Drs. Stephen Danczyk and Douglas Talley of the AFRL, and Drs. Sean Kearney and Darcie Farrow of Sandia National Laboratories for helpful discussions.

6.5 References

1. S. Roy, J. R. Gord, and A. K. Patnaik, "Recent advances in coherent anti-Stokes Raman scattering spectroscopy: Fundamental developments and applications in reacting flows," *Prog. Energ. Combust.* **36**, 280–306 (2010).
2. A. C. Eckbreth, *Laser diagnostics for combustion temperature and species* (Gordon and Breach Publishers, 1996).
3. J. Kiefer and P. Ewart, "Laser diagnostics and minor species detection in combustion using resonant four-wave mixing," *Prog. Energ. Combust.* **37**, 525–564 (2010).
4. S. A. Tedder, J. L. Wheeler, A. D. Cutler, and P. M. Danehy, "Width-increased dual-pump enhanced coherent anti-Stokes Raman spectroscopy," *Appl. Opt.* **49**, 1305–1313 (2010).
5. S. P. Kearney, R. P. Lucht, and A. M. Jacobi, “Temperature measurements in convective heat transfer flows using dual-broadband, pure-rotational coherent anti-Stokes Raman spectroscopy (CARS),” *Exp. Therm. Fluid Sci.* **19**, 13–26 (1999).

6. P. E. Bengtsson, L. Martinsson, M. Aldén, B. Johansson, B. Lassesson, K. Marforio, G. Lundholm, "Dual-broadband rotational CARS measurements in an IC engine," *P. Combust. Inst.* **25**, 1735–1742 (1994).
7. R. J. M. Westerhof, D. W. F. Brilman, W. P. M. van Swaaij, and S. R. A. Kersten, "Effect of temperature in fluidized bed fast pyrolysis of biomass: oil quality assessment in test units," *Ind. Eng. Chem. Res.* **49**, 1160–1168 (2010).
8. W. Chaiwat, I. Hasegawa, and K. Mae, "Examination of the low-temperature region in a downdraft gasifier for the pyrolysis product analysis of biomass air gasification," *Ind. Eng. Chem. Res.* **48**, 8934–8943 (2009).
9. J. A. Hoolroyd, "Low temperature oxidation catalyst development and applications," *American Filtration and Separation Society Annual Conference*, Valley Forge, PA, 19-22 May 2008.
10. S. Roy, T. R. Meyer, R. P. Lucht, M. Afzelius, P. E. Bengtsson, and J. R. Gord, "Dual-pump dual-broadband coherent anti-Stokes Raman scattering in reacting flows," *Opt. Lett.* **29**, 1843–1845 (2004).
11. A. C. Eckbreth and R. J. Hall, "Cars concentration sensitivity with and without non-resonant background suppression," *Combust. Sci. Technol.* **25**, 175–192 (1981).
12. M. Afzelius, P.-E. Bengtsson, J. Bood, J. Bonamy, F. Chaussard, H. Berger, and T. Dreier, "Dual-broadband rotational CARS modeling of nitrogen at pressures up to 9 MPa. II. Rotational Raman line widths," *Appl. Phys. B* **75**, 771–778 (2002).
13. S. Roy, T. R. Meyer, and J. R. Gord, "Broadband coherent anti-Stokes Raman scattering spectroscopy of nitrogen using a picosecond modeless dye laser," *Opt. Lett.* **30**, 3222–3224 (2005).
14. S. Roy, T. R. Meyer, and J. R. Gord, "Time-resolved dynamics of resonant and nonresonant broadband picosecond coherent anti-Stokes Raman scattering signals," *Appl. Phys. Lett.* **87**, 264103 (2005).
15. T. R. Meyer, S. Roy, and J. R. Gord, "Improving signal-to-interference ratio in rich hydrocarbon-air flames using picosecond coherent anti-Stokes Raman scattering," *Appl. Spectrosc.* **61**, 1135–1140 (2007).
16. W. D. Kulatilaka, P. S. Hsu, H. U. Stauffer, J. R. Gord, and S. Roy, "Direct measurement of rotationally resolved H_2 Q-branch Raman coherence lifetimes using time-resolved picosecond coherent anti-Stokes Raman scattering," *Appl. Phys. Lett.* **97**, 081112 (2010).
17. T. Seeger, J. Kiefer, Y. Gao, B. D. Patterson, C. J. Kliewer, and T. B. Settersten, "Suppression of Raman-resonant interferences in rotational coherent anti-Stokes Raman spectroscopy using time-delayed picosecond probe pulses," *Opt. Lett.* **35**, 2040–2042 (2010).
18. T. Seeger, J. Kiefer, A. Leipertz, B. D. Patterson, C. J. Kliewer, and T. B. Settersten, "Picosecond time-resolved pure-rotational coherent anti-Stokes Raman spectroscopy for N_2 thermometry," *Opt. Lett.* **34**, 3755–3757 (2009).
19. C. J. Kliewer, Y. Gao, T. Seeger, J. Kiefer, B. D. Patterson, and T. B. Settersten, "Picosecond time-resolved pure-rotational coherent anti-Stokes Raman spectroscopy in sooting flames," *P. Combust. Inst.* **33**, 831–838 (2011).
20. P. Beaud, H. M. Frey, T. Lang, and M. Motzkus, "Flame thermometry by femtosecond CARS," *Chem. Phys. Lett.* **344**, 407–412 (2001).

21. H. Frey, P. Beaud, T. Gerber, B. Mischler, P. Radi, and A. Tzannis, "Femtosecond nonresonant degenerate four-wave mixing at atmospheric pressure and in a free jet," *Appl. Phys. B* **68**, 735–739 (1999).
22. G. Knopp, P. Beaud, P. Radi, M. Tulej, B. Bougie, D. Cannavo, and T. Gerber, "Pressure-dependent N_2 Q-branch fs-CARS measurements," *J. Raman Spectrosc.* **33**, 861–865 (2002).
23. R. P. Lucht, S. Roy, T. R. Meyer, and J. R. Gord, "Femtosecond coherent anti-Stokes Raman scattering measurement of gas temperatures from frequency-spread dephasing of the Raman coherence," *Appl. Phys. Lett.* **89**, 251112 (2006).
24. J. R. Gord, T. R. Meyer, and S. Roy, "Applications of ultrafast lasers for optical measurements in combusting flows," *Annu. Rev. Anal. Chem.* **1**, 663–687 (2008).
25. S. Roy, W. D. Kulatilaka, D. R. Richardson, R. P. Lucht, and J. R. Gord, "Gas-phase single-shot thermometry at 1 kHz using fs-CARS spectroscopy," *Opt. Lett.* **34**, 3857–3859 (2009).
26. S. Roy, D. Richardson, P. J. Kinnius, R. P. Lucht, and J. R. Gord, "Effects of N_2-CO polarization beating on femtosecond coherent anti-Stokes Raman scattering spectroscopy of N_2," *Appl. Phys. Lett.* **94**, 144101 (2009).
27. Y. Coello, V. Lozovoy, T. Gunaratne, B. Xu, I. Borukhovich, C. Tseng, T. Weinacht, and M. Dantus, "Interference without an interferometer: a different approach to measuring, compressing, and shaping ultrashort laser pulses," *J. Opt. Soc. Am. B* **25**, A140–A150 (2008).
28. J. D. Miller, M. N. Slipchenko, T. R. Meyer, H. U. Stauffer, and J. R. Gord, "Hybrid femtosecond/picosecond coherent anti-Stokes Raman scattering for high-speed gas-phase thermometry," *Opt. Lett.* **35**, 2430–2432 (2010).
29. J. D. Miller, M. N. Slipchenko, and T. R. Meyer, "Probe-pulse optimization for nonresonant suppression in hybrid fs/ps coherent anti-Stokes Raman scattering at high temperature," *Opt. Express* **19**, 13326–13333 (2011).
30. S. Mukamel, *Principles of Nonlinear Optical Spectroscopy* (Oxford University Press, 1995).
31. B. D. Prince, A. Chakraborty, B. M. Prince, and H. U. Stauffer, "Development of simultaneous frequency- and time-resolved coherent anti-Stokes Raman scattering for ultrafast detection of molecular Raman spectra," *J. Chem. Phys.* **125**, 044502 (2006).
32. M. N. Slipchenko, B. D. Prince, S. C. Ducatman, and H. U. Stauffer, "Development of a simultaneously frequency- and time-resolved Raman-induced Kerr effect probe," *J. Phys. Chem. A* **113**, 135–140 (2009).
33. R. E. Palmer, "The CARSFT computer code for calculating coherent anti-Stokes Raman spectra: user and programmer information," Sandia Rep. SAND–89–8206 (Sandia National Laboratories, Livermore, CA, 1989).
34. F. Vestin, K. Nilsson, and P. E. Bengtsson, "Validation of a rotational coherent anti-Stokes Raman spectroscopy model for carbon dioxide using high-resolution detection in the temperature range 294-1143 K," *Appl. Opt.* **47**, 1893–1901 (2008).
35. A. Bohlin, P.-E. Bengtsson, and M. Marrocco, "On the sensitivity of rotational CARS N_2 thermometry to the Herman-Wallis factor," *J. Raman Spectrosc.*, Available Online Feb. 11, 2011.

36. K. P. Huber and G. Herzberg, *Molecular spectra and molecular structure - IV. Constants of diatomic molecules* (Van Nostrand Reinhold, 1979).
37. L. A. Rahn and R. E. Palmer, "Studies of nitrogen self-broadening at high-temperature with inverse Raman spectroscopy," *J. Opt. Soc. Am. B* **3**, 1164–1169 (1986).
38. L. Martinsson, P. E. Bengtsson, M. Alden, S. Kroll, and J. Bonamy, "A test of different rotational Raman linewidth models: Accuracy of rotational coherent anti-Stokes-Raman ccattering thermometry in nitrogen from 295 to 1850 K," *J. Chem. Phys.* **99**, 2466–2477 (1993).
39. R. L. Farrow and L. A. Rahn, "Optical Stark splitting of rotational Raman transitions," *Phys. Rev. Lett.* **48**, 395–398 (1982).
40. A. C. Eckbreth, "BOXCARS: Crossed-beam phase-matched CARS generation in gases," *Appl. Phys. Lett.* **32**, 421–423 (1978).
41. G. Knopp, P. Radi, M. Tulej, T. Gerber, and P. Beaud, "Collision induced rotational energy transfer probed by time-resolved coherent anti-Stokes Raman scattering," *J. Chem. Phys.* **118**, 8223–8233 (2003).

CHAPTER 7. INTERFERRENCE-FREE GAS-PHASE THERMOMETRY AT ELEVATED PRESSURE USING HYBRID FEMTOSECOND/PICOSECOND COHERENT ANTI-STOKES RAMAN SCATTERING

Modified from a paper published in *Optics Express* **20**, 5003–5010 (2012).

Joseph D. Miller,[1] Chloe E. Dedic,[1] Sukesh Roy,[2] James R. Gord,[3] and Terrence R. Meyer[1,4]

Nonresonant background and rotational-level-dependent dephasing rates can lead to significant uncertainties in coherent anti-Stokes Raman scattering (CARS) signals under high-pressure, low-temperature conditions if the gas composition is unknown. Hybrid femtosecond/ picosecond rotational CARS is employed to minimize or eliminate the influence of nonresonant background and collisions for accurate, frequency-domain thermometry at elevated pressure. The ability to ignore these interferences and achieve thermometric errors of <5% is demonstrated for N_2 and O_2 at pressures up to 15 atm. Similar accuracy can be achieved at higher pressure but this requires corrections for rotational-level-dependent dephasing rates using a time- and frequency-domain theoretical model.

[1] Department of Mechanical Engineering, Iowa State University, Ames, IA
[2] Spectral Energies, LLC, Dayton, OH
[3] Air Force Research Laboratory, Propulsion Directorate, WPAFB, OH
[4] SAOT, Erlangen Graduate School in Advanced Optical Technologies, University of Erlangen-Nuremberg, Erlangen, Germany

7.1 Introduction

Coherent anti-Stokes Raman scattering (CARS) is a highly accurate and precise nonlinear spectroscopic technique that has been utilized for the measurement of gas-phase temperature in a wide range of reacting and non-reacting flows [1]. While CARS offers excellent chemical specificity and efficient signal collection, measurement errors from composition-dependent interferences, such as nonresonant background and collisional energy transfer, significantly complicate the analysis, particularly in high-pressure environments [2]. The resonant and nonresonant background signals can be separated in the frequency domain using polarization techniques [3] or in the time domain by temporally separating the probe pulse from the pump and Stokes pulses. The time-domain approach has been demonstrated previously for both vibrational [1, 4] and rotational CARS [5], but the pulse widths were sufficiently long (~100 ps) that the rovibrational and rotational spectra were perturbed by the different collisional dephasing rates of individual rotational transitions. To avoid the effects of collisions, it is possible to employ femtosecond (fs) pulses and early probe-pulse timing. In this case, the profile of the time-domain signal is dominated by frequency-spread dephasing, which takes place within just a few ps and is a strong function of temperature only [1, 6]. Previous work has shown that frequency-spread dephasing is much faster than collisional dephasing for probe delays as long as 15 ps and pressures up to 10 atm [6, 7], meaning that uncertainties due to the complex collisional environment can be avoided. For single-shot thermometry, however, this approach requires a temporally chirped probe pulse, and it is unclear whether measurements that are free of both nonresonant background and collisional effects are possible at higher pressure.

Recently, the authors demonstrated a hybrid fs/ps CARS technique that employed 100-fs pump and Stokes pulses to induce coherent vibrational or pure rotational Raman oscillations in N_2 while probing the molecular response using a frequency-narrowed, time-delayed 1–10 ps probe pulse [8–10]. In this approach, a short (0.3–10 ps) probe-pulse delay was sufficient to avoid overlap with the pump and Stokes pulses to eliminate nonresonant background, while the transform-limited ps pulse allowed for frequency-domain detection of individual vibrational [9, 10] or rotational transitions [8]. In the current work, we investigate the ability of hybrid fs/ps rotational coherent anti-Stokes Raman scattering (RCARS) to avoid the effects of collisions for accurate, interference-free thermometry at high pressure. The ability to avoid collisional effects at high pressure is a significant innovation for frequency-domain thermometry, which typically carries inherent sensitivity to rotational-level-dependent linewidths in the case of ns or ps CARS. Expanding the technique to include fs/ps RCARS thermometry of O_2, we use a phenomenological model to compare the relative effects of collisions on O_2 and N_2 spectra for probe delays of 6.5 to 150 ps. For conditions in which collisions cannot be avoided, we evaluate the feasibility of improving temperature accuracy by minimizing the corrections using a time- and frequency-resolved theoretical model.

A detailed theoretical treatment of hybrid fs/ps CARS and experimental description can be found elsewhere [8,11]. For pure *S*-branch transitions (Δv = 0, ΔJ = +2), the molecular response from the pump (ω_{pump}) and Stokes (ω_{Stokes}) pulses is treated phenomenologically as a function of time, t,

$$R(t) = \sum I_{J+2,J}(T) e^{-i\omega_{J+2,J}t - \Gamma_{J+2,J}t} \tag{7.1}$$

where each transition is assigned an intensity, $I_{J+2,J}$, a frequency (s^{-1}), $\omega_{J+2,J}$, and linewidth (s^{-1}), $\Gamma_{J+2,J}$ [8,11]. The transition intensity $I_{J+2,J}$ is not a function of time, but is highly dependent on temperature, T. The response decays exponentially with a time constant $\tau_{J+2,J} = \Gamma_{J+2,J}^{-1}$. The linewidth is highly temperature and pressure dependent, displaying a linear dependence on pressure and more complex inverse relationship with temperature [12]. Because low rotational states decay more rapidly than high rotational states, the spectral and temporal features of the CARS signal begin to mimic higher temperatures at long delay times [5, 8, 13]. The resulting thermometric error is more pronounced at low temperature where the difference between linewidths of low and high rotational states is largest [5, 8]. At higher pressure, rapid collisional dephasing can also significantly enhance rotational energy transfer and require detection at short delay times for accurate interference-free thermometry.

N_2 and O_2 CARS spectra were recorded at 298 and 295 K, respectively, from 1–20 atm. The pure gases were pressurized in a cylindrical stainless-steel vessel, and the temperature was measured with a 1/16-inch diameter K-type thermocouple and pressure with a digital pressure gauge (0–500 ± 1.25 psi). The spectrally integrated RCARS signals as functions of probe delay are given in Fig. 7.1 for N_2 and O_2 at pressures of 1, 2.5, 5, 10, 15, and 20 atm.

The RCARS spectra are integrated from 10–200 cm^{-1} to avoid interferences from the forward scattered probe. The solid lines represent simulations using a time- and frequency-domain theoretical model with modified exponential gap (MEG) linewidth parameters from Seeger *et al.* [2] and *S*-branch linewidths approximated following Martinsson *et al.* [14]. The experimentally measured time decays are well predicted by the theoretical model and illustrate the short time window between nonresonant background and strong collisional

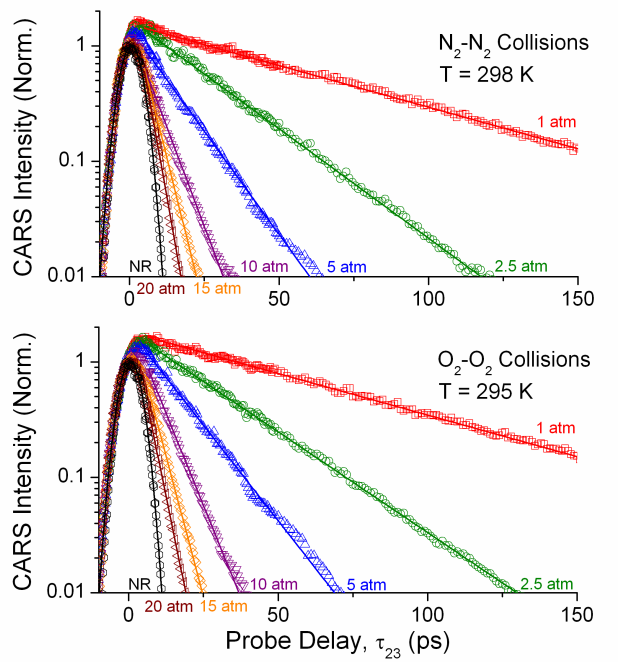

Figure 7.1. Spectrally integrated hybrid fs/ps RCARS signals from 1–20 atm for (a) N_2–N_2 collisions at 298 K, and (b) O_2–O_2 collisions at 295 K. The solid lines are theoretical simulations and the data are normalized to the nonresonant background.

dephasing at high pressure. The dephasing rate for N_2 is faster than that of O_2, which implies that N_2 CARS thermometry will be more sensitive to collisions.

7.2 Influence of Collision-Broadened Linewidth at Elevated Pressure

Because of rapid collisional dephasing at high pressure, the probe-pulse spectral bandwidth was increased from previous work (2.1 cm^{-1}) [8] to 3.6 cm^{-1} (4.1 ps) to achieve a minimum probe delay of 6.5 ps (~1000× nonresonant suppression). This bandwidth is sufficient to avoid spectral overlap of the transitions so that the effects of rotational energy transfer can be clearly observed in the frequency-domain spectra. For illustration, experimental O_2 spectra are presented in Fig. 7.2 at fixed delays of (a) 6.5 and (b) 25 ps and pressures of 1 atm and 10

atm (symbols). The theoretical O_2 spectrum (solid lines) assumes a pressure of 1 atm. At a probe delay of 6.5 ps, shown in Fig. 7.2(a), the difference between the two experimental spectra is negligible, leading to best-fit temperatures that are within 4% of 295 K. This illustrates the independence from collisional effects at short probe delays. For the longer probe delay of 25 ps, as shown in Fig. 7.2(b), the experimental spectrum at 1 atm is the same as that shown at 6.5 ps. However, for a probe delay of 25 ps and a pressure of 10 atm, the spectrum shows a significant population shift towards higher rotational states, leading to a best-fit temperature of 342 K. This represents an error of 16%.

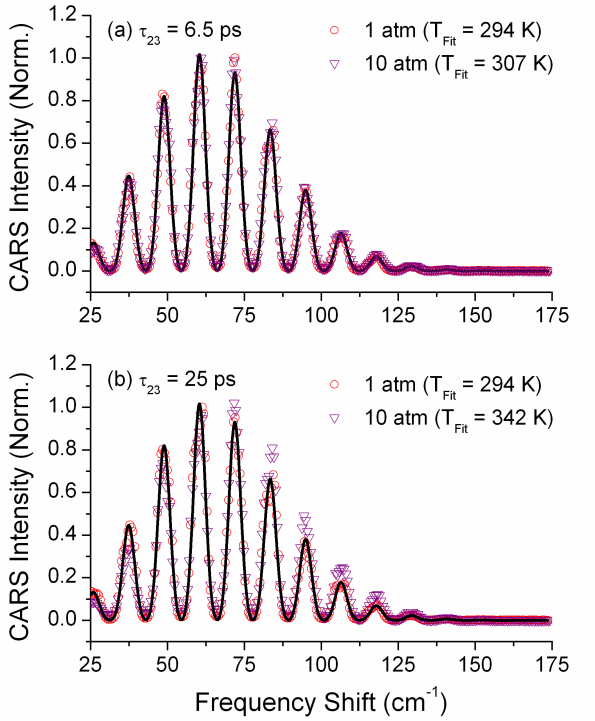

Figure 7.2. Spectrally resolved hybrid fs/ps RCARS spectra of O_2 at 1 atm and 10 atm and probe delays of (a) 6.5 ps and (b) 25 ps. The best fit temperatures neglecting collisional energy transfer are given and the solid line represents the best fit spectra at 1 atm.

As noted earlier avoiding model corrections for the effects of collisions is important when the gas composition is not known *a priori*, but at elevated pressure this requires that the probe pulse be shorter than and arrive sooner than 25 ps. To evaluate the potential for interference-free measurements from 1–20 atm, the thermometric error was investigated from a minimum probe delay of 6.5 ps (to avoid nonresonant background) to a maximum of 150 ps (typical of ps CARS with probe pulses of ~80 ps or higher). This investigation was performed by fitting the time-dependent spectra using a spectral database where the linewidth was set to zero in the molecular response function (Eq. 7.1) for all rotational transitions. Best-fit temperatures are plotted as a function of probe delay in Figs. 7.3(a) and 7.4(a). The constant solid line represents the actual temperature, and the constant dashed lines represent ±5% error.

7.3 Experimental Results for N_2 and O_2

The data of Figs. 7.3(a) and 7.4(a) show the quantitative impact of collisions on thermometric error associated with N_2 or O_2 CARS spectra at elevated pressure. At the shortest probe delay of 6.5 ps, for example, the thermometric error without corrections for nonresonant background or collisional energy transfer is <5% up to 15 atm. Even at 6.5 ps, however, the error increases to 9% at 20 atm, requiring corrections for the effects of collisions.

In cases for which corrections are necessary, the use of short probe delays clearly reduces the impact of collisions and minimizes the corresponding corrections for rotational-level-dependent dephasing with the time- and frequency-resolved theoretical model. As shown in Figs. 7.3(b) and 7.4(b), the theoretical model predicts temperatures that are within

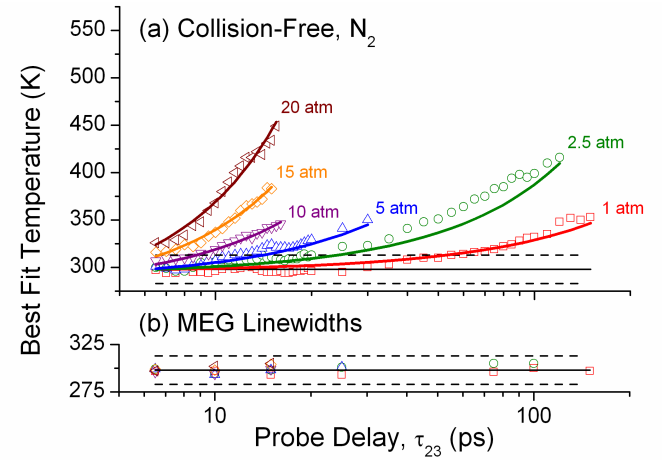

Figure 7.3. (a) Best-fit temperatures from experimental spectra for N_2 (at 298 K) invoking the collision-free assumption at pressures from 1–20 atm. Solid curve fits are based on Eq. 7.2 and dashed lines represent errors of ±5%. (b) Corrected temperatures using MEG linewidths.

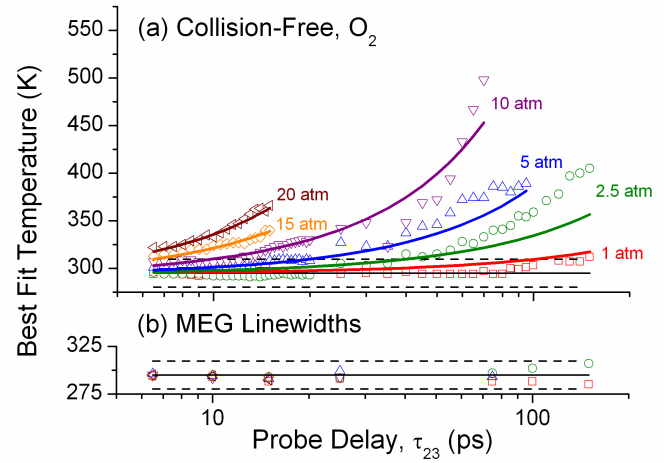

Figure 7.4. (a) Best-fit temperatures from experimental spectra for O_2 (at 295 K) invoking the collision-free assumption at pressures from 1–20 atm. Solid curve fits are based on Eq. 7.2 and dashed lines represent errors of ±5%. (b) Corrected temperatures using MEG linewidths.

5% of the known temperatures for all pressures and probe delays. At shorter probe delays (<100 ps), the accuracy is improved to 2.5% for all pressures, and at the shortest probe delay (6.5 ps), the accuracy improves to 1% for all pressures. The fact that the theoretical fit is improved at shorter probe delays is indicative of reduced interference from collisional

effects, which could be critical in environments with unknown species compositions. Since the composition is known in this case, the increase in thermometric error up to 5% at 150 ps can be attributed to differences between the *S*-branch linewidths and the MEG linewidths with *Q*-branch approximations. By minimizing the necessary corrections, the fs/ps hybrid RCARS approach also reduces the effects of errors associated with uncertainties in linewidth.

To characterize further the sensitivity to collisional dephasing and predict thermometric errors for arbitrary pressures and probe delays, we utilized a phenomenological model that captures the increase in thermometric error with pressure and time (as indicated by the solid lines in Fig. 7.3 and 7.4),

$$T_{App}\left(\tau_{23},P\right)=\left(1-a_1P\right)T_o\exp\left[\left(a_2P^2+a_3P\right)\tau_{23}\right] \tag{7.2}$$

where T_{App} is the apparent temperature with the collision-free assumption (K), τ_{23} is the probe delay (ps), T_o is the reference temperature (K), P is the pressure (atm), and a_i are fit parameters. The coefficients have been determined with a fair degree of consistency from 1–20 atm and at room temperature for N_2 (a_1 = 7.36×10^{-3} atm^{-1}, a_2 = 4.257×10^{-5} atm^{-2}ps^{-1}, and a_3 = 1.016×10^{-3} atm^{-1}ps^{-1}) and for O_2 (a_1 = 1.405×10^{-3} atm^{-1}, a_2 = 1.563×10^{-5} atm^{-2}ps^{-1}, and a_3 = 4.77×10^{-4} atm^{-1}ps^{-1}). The reduced sensitivity of O_2 to collisional effects at elevated pressure is quantified by the lower values of a_2 and a_3 in the exponential term in Eq. 7.2. This is due to greater uniformity in linewidth across the rotational energy levels of O_2. This simple model can also be used to estimate the probe delay, τ_{23}, and the associated minimum probe pulse width necessary for avoiding the effects of collisions at even higher pressures with frequency-domain ps or fs/ps CARS thermometry. At 20 atm, for example, the temperature shift is as high as 14.5 K/ps for N_2 and 5.7 K/ps for O_2. Without this knowledge,

the use of longer probe delays or slight jitter between the preparation and probe pulses can cause significant variations in the apparent temperature (as high as 5% per ps).

7.4 Time-Asymmetric Probe Pulse using a Fabry–Pérot Etalon

To reduce the necessary probe delay and greatly simplify the fs/ps RCARS setup, a time-asymmetric exponential probe pulse was introduced using a Fabry–Pérot etalon with Γ_{FWHM} = 5.6 cm^{-1} [15]. This probe pulse differs from our previous work in fs/ps VCARS which used a 13-cm^{-1} Lorentzian filter to produce the probe pulse [10]. In addition to reducing the necessary probe delay for nonreosnant suppression, the introduction of the etalon greatly simplifies the fs/ps RCARS experimental implementation. In the degenerate configuration of RCARS presented here, no frequency conversion is necessary while alignment of the etalon is significantly less complicated than construction of the 4-*f* pulse shaper. This implementation produces arguably the simplest CARS configuration reported in the literature.

As described in detail in Chapter 3, the etalon produces a sharp rise followed by an exponential decay with the time constant associated with the Lorentzian bandwidth (Eq. 6.9). The decay and spectral profile of the probe pulse are shown in Fig. 7.5 along with a best fit simulation of the pulse. The rising edge exhibits a HWHM of 121 fs while the exponential decay produces a Lorentzian bandwidth of 5.97 cm^{-1} in good agreement with the spectrally resolved linewidth of 5.93 cm^{-1}. Small fluctuations are visible in the time-domain data which correspond to interferrence between the main peak and two side bands at ± 290 cm^{-1}, approximately equal to the free-spectral range of the etalon.

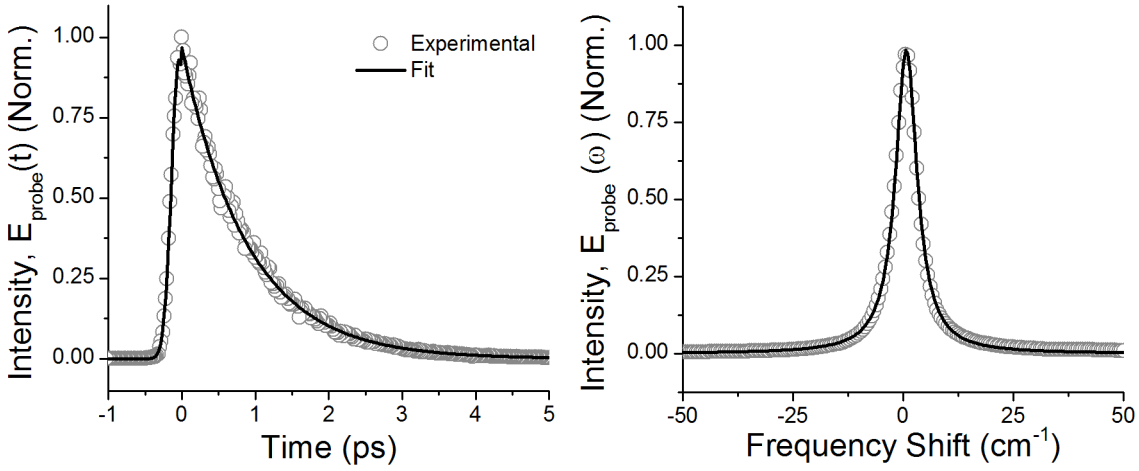

Figure 7.5. Temporal (left) and spectral (right) profile of the time-asymmetric probe pulse using the Fabry–Pérot etalon.

The fast rising edge of the time-asymmetric exponential probe pulse produces a unique time-domain profile for N_2 and O_2 RCARS signal. As shown in Fig. 7.6 for N_2 (top) and O_2 (bottom), the CARS signal drops rapidly after the initial excitaiton and rises slowly towards the first partial recurrence. Good agreement is observed between the experimental spectrally-integrated *S*-branch CARS signal and the computed molecular response. For N_2, the maximum signal occurs at the first major (half) recurrence at ~4.2 ps although the probe delay can be reduced to 2.1 ps if the first minor (quarter) recurrence is used. Since only the odd transitions are active for O_2, the maximum signal occurs during the first major recurrence at 2.9 ps.

Of particular interest in this work is the spectral resolution of the resulting CARS signal. The experimental RCARS spectra for N_2 at τ_{23} = 2.1 ps (top) and 4.2 ps (bottom) are compared with an isolated line computation using a 2.1-cm^{-1} Gaussian probe pulse in Fig. 7.7. During the first minor (quarter) recurrence only the even transitions are observed while

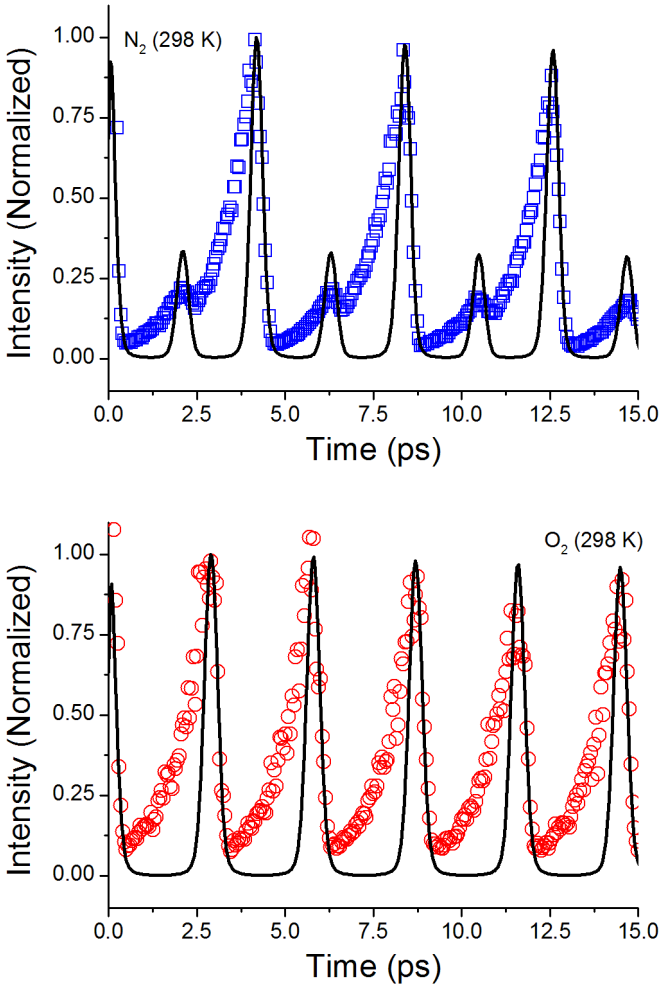

Figure 7.6. Spectrally-integrated time-domain RCARS signal (symbols) for (top) N_2 and (bottom) O_2 along with the theoretical molecular response (line).

both odd and even transitions are observed during the first major (half) recurrence. This behavior can be described in terms of the total alignment of the temporally evolving rotational wavepacket as described in our current publication and will not be described here [15]. The advantage of the first minor recurence is that even transitions are completely isolated and readily resolved with the Lorentzian bandwidth. Additionally, the probe delay is reduced to 2.1 ps which will be advantageous at elevated pressure currently under

investigation. In contrast, the spectral O_2 RCARS signal is identical at all recurrences since only the odd transitions are active. The time-asymmetric and isolated CARS spectra are given in Fig. 7.8. As expected, the time-asymmetric probe produces a significantly broader spectra than the narrowband Gaussian probe.

Finally, the etalon probe was investigated in air. The spectrally-integrated time-domain *S*-branch RCARS signal is given in Fig. 7.9 (top) along with the N_2 and O_2 molecular response functions. The peaks associated with the N_2 and O_2 recurrences are observed with

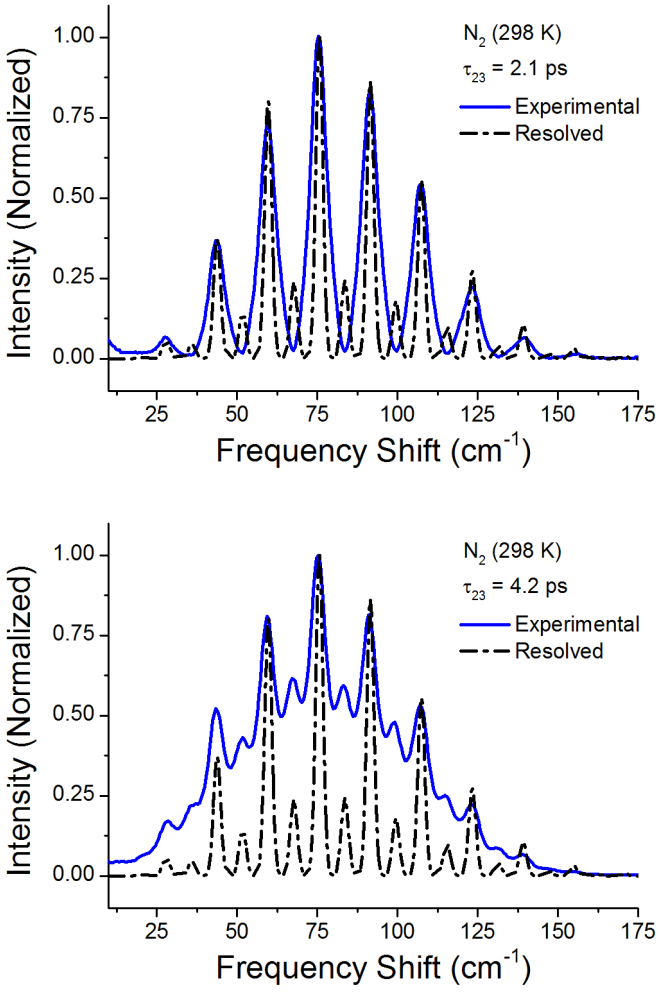

Figure 7.7. Spectral N_2 RCARS signal at (top) τ_{23} = 2.1 ps and (bottom) 4.2 ps. The isolated RCARS spectrum is given for comparison.

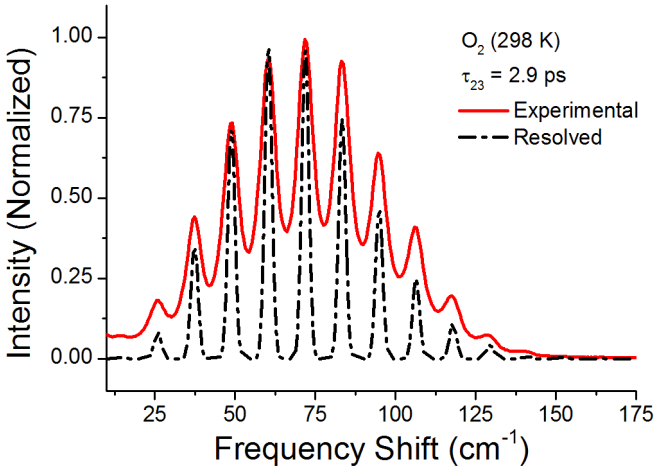

Figure 7.8. Spectral O_2 RCARS signal at τ_{23} = 2.9 ps. The isolated RCARS spectrum is given for comparison.

maximum signal occuring at ~8.4 ps where a major recurrence of both molecules overlaps. A unique advantage of the sharp rising edge is the ability to select probe delays where individual molecules are dominant. For instance, at 6.45 ps the second minor (three-quarter) recurrence of N_2 can be separated from the O_2 molecular response. The spectral RCARS signal at this delay is given in Fig. 7.9 (bottom) along with the pure N_2 RCARS spectrum. At this delay, the air spectrum is dominated by the even transitions of the N_2 molecule although interactions with O_2 influence the spectrum, especially at longer frequencies where the transitions intensities appear attenuated.

In summary, we have quantified the effects of pressure on hybrid fs/ps CARS thermometric errors for both N_2 and O_2 up to 20 atm. Utilizing fs pump and Stokes pulses and a probe-pulse delay of 6.5 ps, it is possible to avoid the effects of collisions for pressures up to 15 atm and minimize corrections for collisional effects at even higher pressures. This

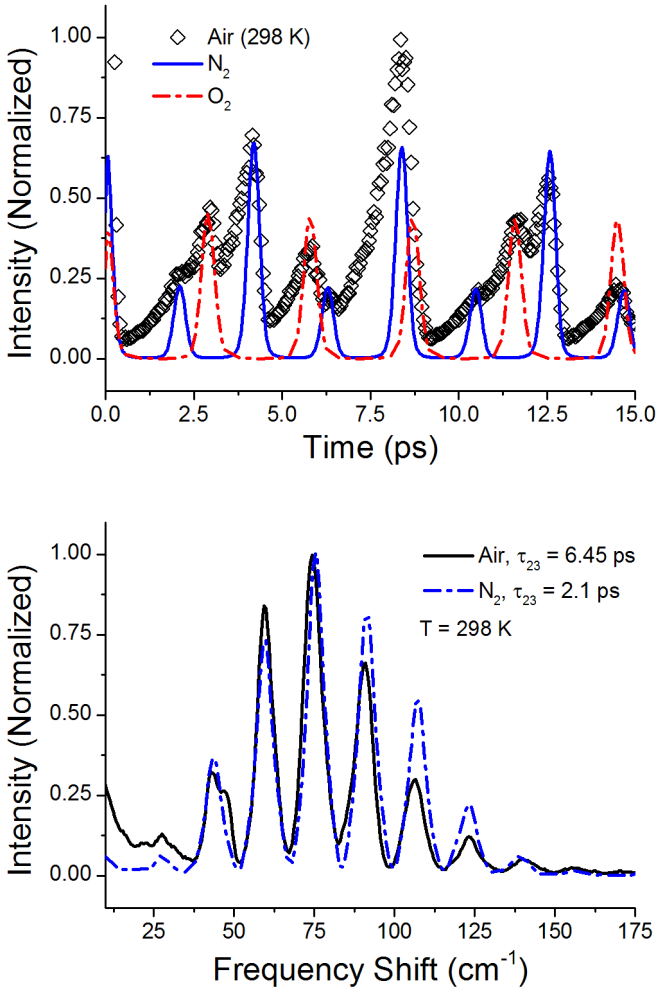

Figure 7.9. Time-domain RCARS signal of air (top) with the theoretical N_2 and O_2 molecular responses and RCARS spectrum of air (bottom) at 6.45 ps compared to the pure N_2 spectrum at 6.3 ps.

can be achieved while avoiding nonresonant background and isolating individual rotational transitions for accurate frequency-domain thermometry within unknown gas-phase mixtures. Additionally, a time-asymmetric exponential probe pulse was introduced using a narrow-bandwidth Fabry–Pérot etalon. This probe pulse allows a reduction in probe delay from 6.5 ps to 2.1 ps with sufficient resolution for isolating even rotational transitions during the first quarter recurrence of the rotational wavepacket. In air the temporal and spectral response

becomes more complicated, but a judicious choice of probe delay can help to isolate the response of an individual molecular component of air.

Funding was provided, in part, by the National Science Foundation (CBET-1056006, Dr. A. Atreya, Program Official) and Air Force Office of Scientific Research (Drs. T. Curcic and M. Birkan, Program Managers). J. Miller was supported by the National Science Foundation Graduate Fellowship Program. The authors also thank Dr. H. Stauffer of Spectral Energies, LLC, M. Johnson and B. Halls of Iowa State University, and Drs. S. Danczyk and D. Talley of the Air Force Research Laboratory.

7.5 References

1. S. Roy, J. R. Gord, and A. K. Patnaik, "Recent advances in coherent anti-Stokes Raman scattering spectroscopy: Fundamental developments and applications in reacting flows," *Prog. Energ. Combust.* **36**, 280–306 (2010).
2. T. Seeger, F. Beyrau, A. Brauer, and A. Leipertz, "High-pressure pure rotational CARS: comparison of temperature measurements with O_2, N_2 and synthetic air," *J. Raman Spectrosc.* **34**, 932–939 (2003).
3. F. Vestin, M. Afzelius, and P. E. Bengtsson, "Development of rotational CARS for combustion diagnostics using a polarization approach," *Proc. Combust. Inst.* **31**, 833–840 (2007).
4. T. R. Meyer, S. Roy, and J. R. Gord, "Improving signal-to-interference ratio in rich hydrocarbon-air flames using picosecond coherent anti-stokes Raman scattering," *Appl. Spectrosc.* **61**, 1135–1140 (2007).
5. T. Seeger, J. Kiefer, A. Leipertz, B. D. Patterson, C. J. Kliewer, and T. B. Settersten, "Picosecond time-resolved pure-rotational coherent anti-Stokes Raman spectroscopy for N_2 thermometry," *Opt. Lett.* **34**, 3755–3757 (2009).
6. R. P. Lucht, S. Roy, T. R. Meyer, and J. R. Gord, "Femtosecond coherent anti-Stokes Raman scattering measurement of gas temperatures from frequency-spread dephasing of the Raman coherence," *Appl. Phys. Lett.* **89**, 251112 (2006).
7. G. Knopp, P. Beaud, P. Radi, M. Tulej, B. Bougie, D. Cannavo, and T. Gerber, "Pressure-dependent N_2 Q-branch fs-CARS measurements," *J. Raman Spectrosc.* **33**, 861–865 (2002).
8. J. D. Miller, S. Roy, M. N. Slipchenko, J. R. Gord, and T. R. Meyer, "Single-shot gas-phase thermometry using pure-rotational hybrid femtosecond/picosecond coherent anti-Stokes Raman scattering," *Opt. Express* **19**, 15627–15640 (2011).

9. J. D. Miller, M. N. Slipchenko, T. R. Meyer, H. U. Stauffer, and J. R. Gord, "Hybrid femtosecond/ picosecond coherent anti-Stokes Raman scattering for high-speed gas-phase thermometry," *Opt. Lett.* **35**, 2430–2432 (2010).
10. J. D. Miller, M. N. Slipchenko, and T. R. Meyer, "Probe-pulse optimization for nonresonant suppression in hybrid fs/ps coherent anti-Stokes Raman scattering at high temperature," *Opt. Express* **19**, 13326–13333 (2011).
11. B. D. Prince, A. Chakraborty, B. M. Prince, and H. U. Stauffer, "Development of simultaneous frequency- and time-resolved coherent anti-Stokes Raman scattering for ultrafast detection of molecular Raman spectra," *J. Chem. Phys.* **125**, 044502 (2006).
12. L. A. Rahn and R. E. Palmer, "Studies of nitrogen self-broadening at high-temperature with inverse Raman-spectroscopy," *J. Opt. Soc. Am. B* **3**, 1164–1169 (1986).
13. B. Lavorel, H. Tran, E. Hertz, O. Faucher, P. Joubert, M. Motzkus, T. Buckup, T. Lang, H. Skenderovi, G. Knopp, P. Beaud, and H. M. Frey, "Femtosecond Raman time-resolved molecular spectroscopy," *C. R. Phys.* **5**, 215–229 (2004).
14. L. Martinsson, P. E. Bengtsson, M. Alden, S. Kroll, and J. Bonamy, "A test of different rotational Raman linewidth models: accuracy of rotational coherent anti-Stokes-Raman scattering thermometry in nitrogen from 295 to 1850 K," *J. Chem. Phys.* **99**, 2466–2477 (1993).
15. H. U. Stauffer, J. D. Miller, S. Roy, J. R. Gord, and T. R. Meyer, “Communication: Hybrid femtosecond/picosecond coherent anti-Stokes Raman scattering thermometry using a narrowband time-asymmetric probe pulse,” *J. Chem. Phys.* **136**, 111101 (2012).

CHAPTER 8. TIME-DOMAIN MEASUREMENT OF HIGH-PRESSURE N_2 AND O_2 SELF-BROADENED LINEWIDTHS USING HYBRID FEMTOSECOND/PICOSECOND COHERENT ANTI-STOKES RAMAN SCATTERING

Modified from a paper published in *Journal of Chemical Physics* **135**, 201104 (2011).

Joseph D. Miller,[1] Sukesh Roy,[2] James R. Gord,[3] and Terrence R. Meyer[1,4]

The direct measurement of self-broadened linewidths using the time decay of pure-rotational hybrid femtosecond/picosecond coherent anti-Stokes Raman scattering (fs/ps RCARS) signals is demonstrated in gas-phase N_2 and O_2 from 1–20 atm. Using fs pump and Stokes pulses and a spectrally narrowed ps probe pulse, collisional dephasing rates with time constants as short as 2.5 ps are captured with high accuracy for individual rotational transitions. *S*-branch linewidths of N_2 and O_2 from ~0.06 to 2.2 cm^{-1} and the line separation of O_2 triplet states are obtained from the measured dephasing rates and compared with high-resolution, frequency-domain measurements and *S*-branch approximations using the modified exponential gap model. The accuracy of the current measurements suggests that the fs/ps RCARS approach is well suited for tracking the collisional dynamics of gas-phase mixtures over a wide range of pressures.

[1] Department of Mechanical Engineering, Iowa State University, Ames, IA
[2] Spectral Energies, LLC, Dayton, OH
[3] Air Force Research Laboratory, Propulsion Directorate, WPAFB, OH
[4] SAOT, Erlangen Graduate School in Advanced Optical Technologies, University of Erlangen-Nuremberg, Erlangen, Germany

8.1 Introduction

The use of femtosecond (fs) and picosecond (ps) laser sources for gas-phase coherent anti-Stokes Raman scattering (CARS) thermometry has grown significantly in recent years due to the high peak powers of these laser sources and interest in resolving the time dynamics of the molecular response [1]. In fs CARS the temporally short and spectrally broad (transform-limited) pump and Stokes pulses allow highly efficient, in-phase and impulsive excitation of the entire rovibrational or pure-rotational manifold [1–3]. In this case the molecular response is resolved in time using the spectrally integrated signal, but the dephasing rate of individual (*J*-level) transitions cannot be measured directly [2, 3]. In ps CARS the ability to measure short time decays is limited by relatively long pump, Stokes, and probe pulse widths (typically ~100 ps), and by the need to avoid nonresonant background by temporally separating the probe pulse from the pump and Stokes pulses [4–6]. For measurements of collisional dephasing rates, especially at high pressure, the ideal approach is to utilize broad (fs) pump and Stokes pulses and a spectrally narrowed (ps) probe pulse that can simultaneously isolate each molecular transition while still resolving short ~ps decay times.

Recently, the authors demonstrated a hybrid fs/ps CARS technique that uses 100-fs pump and Stokes pulses to impulsively excite vibrational or pure rotational transitions of a molecule and a spectrally narrowed, 1–10 ps probe pulse for frequency-domain thermometry [7, 8]. A similar single-beam approach using a pulse-shaped 7-fs pulse to produce the pump, Stokes, and probe pulses via phase and polarization discrimination has been demonstrated, although the spectral resolution was limited to ~5 cm^{-1} by the spatial light modulator [9]. The hybrid fs/ps CARS approach offers the ability to temporally discriminate against nonresonant background, similar to either fs or ps CARS, but has the unique capability to

resolve gas-phase rotational spectra within several hundred fs after Raman excitation [10]. These features are ideal for studying the time dynamics of individual rotational transitions at elevated pressure. Above 1 atm, the linewidths of N_2 and O_2 can be considered purely pressure broadened, and Doppler contributions to the linewidth can be neglected. Hence, detection of collisional decay rates for rotational transitions using fs/ps CARS allows for direct measurement of spectral linewidths [7].

In this work, a time- and frequency-resolved fs/ps RCARS technique is used to accurately measure and report self-broadened *S*-branch linewidths of N_2 and O_2 from 1–20 atm. Few direct measurements of self-broadened *S*-branch linewidths are reported in the literature, and many ps and ns rotational CARS models rely on *S*-branch approximations from *Q*-branch data which can lead to errors at high pressure [11, 12]. These measurements are critical for the determination of temperature and relative species concentrations in gas-phase media, especially at high pressure, because rotational-level and species-dependent collisional dephasing rates can alter the Raman spectra and lead to significant measurement errors [4, 6].

8.2 Linewidth Measurement Approach

The hybrid fs/ps RCARS system has been described previously and is summarized briefly in this Communication [7, 8, 10]. The pump and Stokes pulses were derived from the 100-fs output of a regeneratively-amplified Ti:sapphire laser centered at ~790 nm. An energy of 40 μJ was used for each pulse at atmospheric pressure and was decreased at elevated pressure to avoid stimulated Raman pumping and interference from sustained molecular alignment. A 2-cm^{-1} full-width at half maximum (FWHM), 8.1-ps probe pulse was formed in a 4-*f* pulse

shaper by spectrally filtering the beam using a square slit. This bandwidth was sufficient to isolate individual transitions while minimizing the probe delay for nonresonant suppression. The slit was slightly rotated to produce a nearly Gaussian time-domain profile [7]. The three beams were focused in a BOXCARS phase-matching configuration using a 300-mm lens. The CARS beam was spatially filtered and then detected using a 0.303-m spectrometer with a 1200 line/mm grating and an electron-multiplied charge-coupled device camera. The gases were pressurized in a cylindrical stainless steel vessel equipped with a 1/16-inch diameter K-type thermocouple and digital pressure gauge (0–500 ±1.25 psi).

A theoretical description of the hybrid fs/ps RCARS process is given elsewhere [7, 8, 13]. Of particular interest here is the treatment of the molecular response function. For pure rotational transitions ($\Delta v = 0$), a phenomenological function is given as the summation of all active *O*-branch ($\Delta J = -2$) and *S*-branch transitions ($\Delta J = +2$) from state *m* to *n*

$$R(t) = \sum I_{n,m}(T) e^{-i\omega_{n,m}t - \Gamma_{n,m}t} \tag{8.1}$$

where $I_{n,m}$ is the intensity of each rotational Raman transition as a function of temperature [7] and $\omega_{n,m}$ (s^{-1}) is the frequency of each transition. The linewidth, $\Gamma_{n,m}$ (s^{-1}), is related to the *S*-branch spectral linewidth (m^{-1}, FWHM) and decay constant, $\tau_{CARS,J+2,J}$ (s)

$$\Gamma_{J+2,J}\Big|_t = 2\pi c \Gamma_{J+2,J}\Big|_\omega = \left(\tau_{CARS,J+2,J}\right)^{-1} \tag{8.2}$$

where *c* is the speed of light (m/s) [5]. The linewidth represents a single-exponential decay of the molecular response in time due primarily to inelastic molecular collisions [2, 14]. The modified exponential gap (MEG) model is frequently employed to calculate the transition dependence (initial state *m*) of the collisional linewidth assuming a linear dependence on pressure [14]. In this work, comparisons are made with the MEG model using parameters for

self-broadened N_2 and O_2 from Seeger *et al.* and the rotational approximation of Martinsson *et al* [11, 15].

For simple linear molecules such as N_2, the rotational levels are well known and the rotational transitions are indicated by the total angular momentum, J, of the initial state. For O_2, the ground state exhibits a nuclear spin of zero and an electronic spin, S, of one which leads to a splitting of the rotational states into triplets [16, 17]. In this case, the rotational transitions are given as a function of the rotational quantum number, N, of the initial state while the splitting occurs due to the N-S coupling with the total angular momentum given by $J = (N\text{-}1, N, N\text{+}1)$ [16].

Rotationally resolved RCARS signals of N_2 (298 K) and O_2 (295 K) are shown as a function of probe delay in Fig. 8.1 for pressures of 1, 10, and 20 atm. Three independent scans for each pressure were performed over a one week period to verify repeatability. Only the J = 4 and 14 transitions for N_2 and N = 5 and 15 transitions for O_2 are shown for simplicity. The RCARS signals are compared to the normalized and spectrally integrated nonresonant background from argon to show the relative rates of decay. The time constant of each rotational transition was measured by fitting a single exponential function to the decay of the RCARS signal spectrally integrated over each individual transition, and the spectral linewidth was computed using Eq. 8.2. For most conditions, the fitting process was initiated after a probe delay of 10.5 ps when the nonresonant background dropped by 10^2, as shown in Fig. 8.1. At a fixed probe delay, however, the relative influence of the nonresonant background increased at higher pressure because the resonant signal was sensitive to collisions. To offset this effect, the fitting process for rotational transitions with the lowest signal levels was initiated at longer delays (≥12 ps) to allow the nonresonant to decay even

further. This ensured that the signal-to-nonresonant ratio in the spectral band of each transition, estimated from the nonresonant susceptibilities of Ar, N_2, and O_2, was always 10^2 or higher.

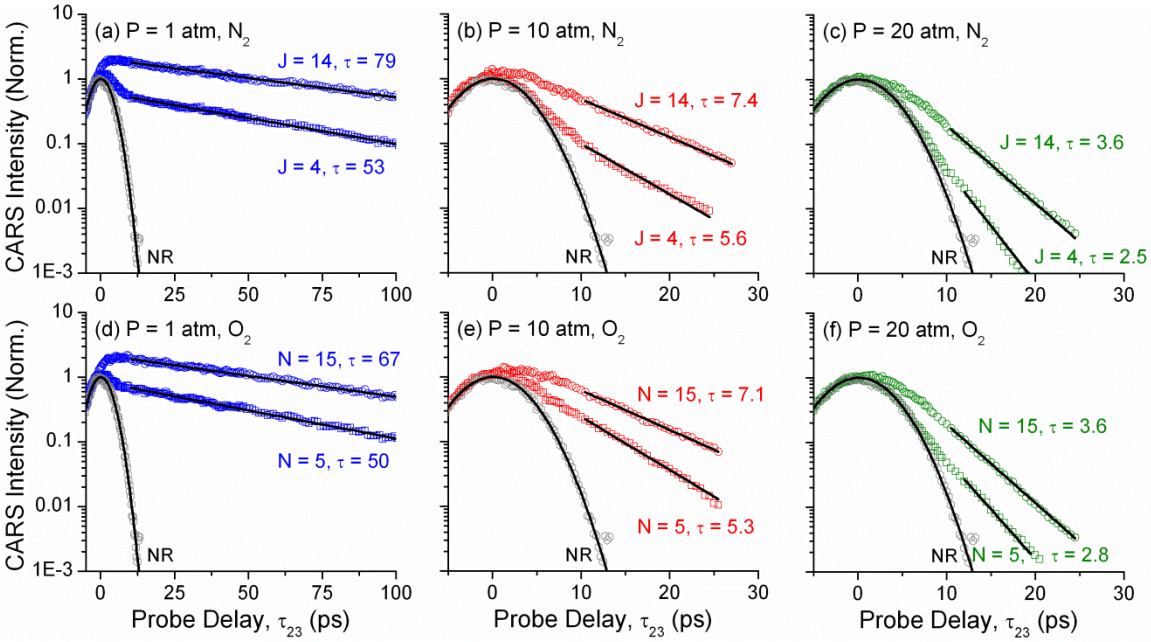

Figure 8.1. Spectrally resolved hybrid fs/ps RCARS signals from $J = 4$ and 14 for N_2 at (a) 1 atm, (b) 10 atm, and (c) 20 atm and $N = 5$ and 15 for O_2 at (d) 1 atm, (e) 10 atm, and (f) 20 atm. Solid lines are exponential fits to signal decay.

8.3 Self-Broadened Linewidths of N_2 and O_2

The measured self-broadened *S*-branch linewidths are shown in Fig. 9.2 at pressures of 1, 10, and 20 atm and tabulated for pressures of 1, 2.5, 5, 10, 15, and 20 atm in Tables 9.1 and 9.2. The uncertainty was calculated from the 95% confidence interval of the average fit with an additional systematic experimental uncertainty (~2%) combined in quadrature. The 95% confidence interval of the average data is comparable to the standard deviation from the three individual data sets. Generally, the *S*-branch linewidths were measured with 1–2% uncertainty at 1 atm, which represents an improvement over previous frequency-domain

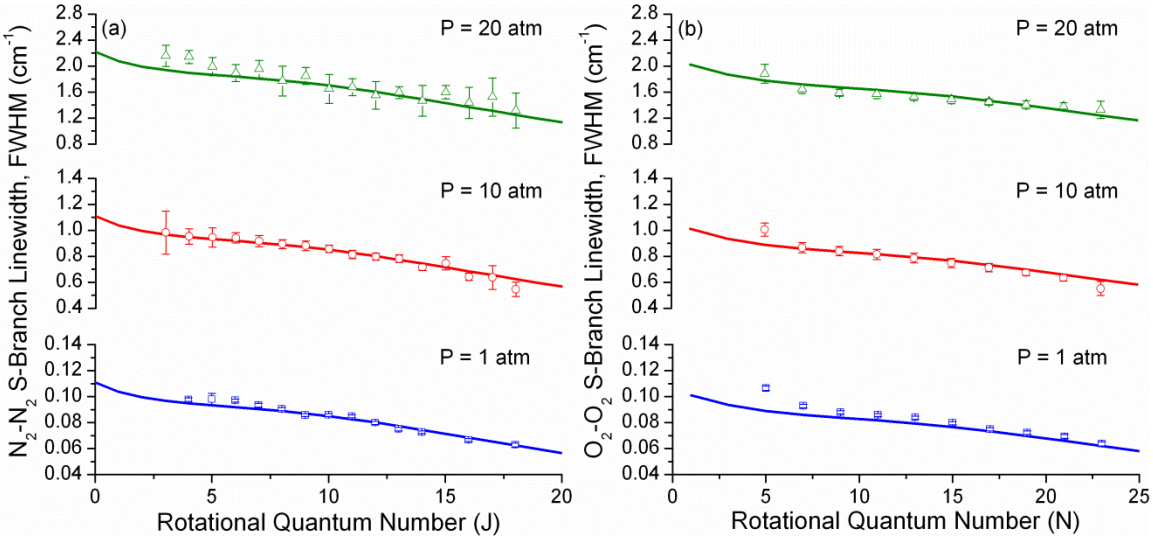

Figure 8.2. Measured (a) N_2 and (b) O_2 self-broadened linewidths as a function of initial rotational state at pressures of 1, 10, and 20 atm. Solid lines are MEG linewidths using *S*-branch approximation. Bars represent calculated uncertainty.

measurements under similar conditions [14, 16]. At the highest pressure of 20 atm, the decay rate constant is as small as 2.5 ps, leading to higher uncertainties for low and high rotational transitions of N_2 and O_2 and odd transitions of N_2.

The solid lines in Fig. 8.2 represent self-broadened linewidths for N_2 and O_2 computed using the MEG model *Q*-branch linewidths derived from frequency-domain measurements with the *S*-branch approximation [11, 15]. The computed linewidths agree well with the current data for N_2 but deviate at low rotational levels as found in previous time-domain [4, 7] and frequency-domain [18] measurements at 1 atm. This shift is due to re-orientation of the molecular axis after collisions, which does not contribute to *Q*-branch linewidths from which the MEG model was derived [12].

The O_2 measured linewidths for high rotational numbers are in agreement with the MEG model at 1 atm and with previous *S*-branch measurements using spontaneous Raman

Table 8.1. Experimental N_2 self-broadened linewidths, FWHM (cm^{-1})

J	1 atm	2.5 atm	5 atm	10 atm	15 atm	20 atm
3		0.266 ± 0.020		0.984 ± 0.165		2.158 ± 0.162
4	0.098 ± 0.001	0.259 ± 0.016	0.505 ± 0.023	0.954 ± 0.060	1.518 ± 0.186	2.140 ± 0.099
5	0.098 ± 0.004	0.262 ± 0.017	0.490 ± 0.025	0.946 ± 0.074	1.505 ± 0.233	1.993 ± 0.141
6	0.097 ± 0.001	0.256 ± 0.017	0.468 ± 0.017	0.943 ± 0.040	1.397 ± 0.174	1.891 ± 0.129
7	0.093 ± 0.001	0.236 ± 0.015	0.456 ± 0.019	0.917 ± 0.043	1.357 ± 0.162	1.956 ± 0.134
8	0.090 ± 0.001	0.233 ± 0.015	0.441 ± 0.015	0.895 ± 0.034	1.335 ± 0.157	1.772 ± 0.230
9	0.086 ± 0.001	0.226 ± 0.015	0.428 ± 0.015	0.882 ± 0.037	1.278 ± 0.170	1.850 ± 0.129
10	0.086 ± 0.001	0.229 ± 0.014	0.430 ± 0.015	0.858 ± 0.029	1.252 ± 0.152	1.649 ± 0.222
11	0.085 ± 0.001	0.221 ± 0.014	0.398 ± 0.015	0.814 ± 0.033	1.192 ± 0.175	1.678 ± 0.130
12	0.080 ± 0.001	0.203 ± 0.013	0.383 ± 0.014	0.798 ± 0.027	1.162 ± 0.149	1.553 ± 0.214
13	0.075 ± 0.001	0.199 ± 0.013	0.362 ± 0.020	0.783 ± 0.030	1.088 ± 0.178	1.594 ± 0.090
14	0.073 ± 0.001	0.194 ± 0.013	0.358 ± 0.014	0.717 ± 0.026	1.051 ± 0.150	1.466 ± 0.235
15		0.191 ± 0.015	0.314 ± 0.018	0.747 ± 0.051	0.926 ± 0.172	1.597 ± 0.105
16	0.067 ± 0.001	0.173 ± 0.012	0.308 ± 0.016	0.643 ± 0.028	0.931 ± 0.145	1.435 ± 0.239
17			0.265 ± 0.050	0.637 ± 0.092	0.790 ± 0.186	1.522 ± 0.294
18	0.063 ± 0.001	0.158 ± 0.019	0.246 ± 0.025	0.548 ± 0.055	0.815 ± 0.147	1.316 ± 0.272

scattering [16]. The linewidths of the low rotational states are influenced by the triplet ground state of the O_2 molecule, which exhibits three transitions (S_-, S_0, S_+) separated by ~1.99 cm^{-1} [16]. Because the triplet is spectrally overlapped by the probe pulse, this separation results in a temporal oscillation of the RCARS signal, as shown in Fig. 9.3 for N = 1 and 3 at 1 atm. A cosine function is used to fit the oscillation with resulting periods of 16.8 ps and 16.9 ps for N = 1 and 3, respectively. These represent separations of 1.98 cm^{-1} and

Table 8.2. Experimental O_2 self-broadened linewidths, FWHM (cm^{-1})

N	1 atm	2.5 atm	5 atm	10 atm	15 atm	20 atm
5	0.107 ± 0.002	0.244 ± 0.015	0.459 ± 0.017	1.006 ± 0.051	1.329 ± 0.039	1.881 ± 0.145
7	0.093 ± 0.001	0.221 ± 0.013	0.434 ± 0.016	0.866 ± 0.040	1.282 ± 0.036	1.646 ± 0.070
9	0.088 ± 0.001	0.212 ± 0.013	0.420 ± 0.014	0.840 ± 0.036	1.243 ± 0.034	1.588 ± 0.056
11	0.086 ± 0.001	0.213 ± 0.013	0.409 ± 0.015	0.815 ± 0.039	1.200 ± 0.039	1.569 ± 0.067
13	0.084 ± 0.001	0.209 ± 0.013	0.398 ± 0.015	0.787 ± 0.036	1.155 ± 0.039	1.523 ± 0.050
15	0.080 ± 0.001	0.196 ± 0.012	0.374 ± 0.015	0.749 ± 0.035	1.114 ± 0.039	1.485 ± 0.061
17	0.075 ± 0.001	0.186 ± 0.012	0.353 ± 0.015	0.714 ± 0.032	1.034 ± 0.042	1.448 ± 0.051
19	0.072 ± 0.001	0.183 ± 0.012	0.333 ± 0.017	0.676 ± 0.025	0.968 ± 0.040	1.406 ± 0.062
21	0.069 ± 0.001	0.168 ± 0.012	0.310 ± 0.023	0.635 ± 0.027	0.927 ± 0.068	1.380 ± 0.056
23	0.064 ± 0.002	0.163 ± 0.016	0.261 ± 0.055	0.552 ± 0.054	0.807 ± 0.144	1.329 ± 0.134

1.97 cm^{-1}, which are within 1% of theoretical and experimental values [16]. While the intensity of the triplets are of the same order for $N = 1$, they are negligible for $N > 5$ [16]. At elevated pressure the CARS signal decays significantly within the first period of the triplet oscillation; thus the oscillation cannot be resolved, and the measured linewidths may be larger than expected due to interference of the triplet oscillation. For this reason we have not reported linewidth data for $N = 1$ and 3 in this work.

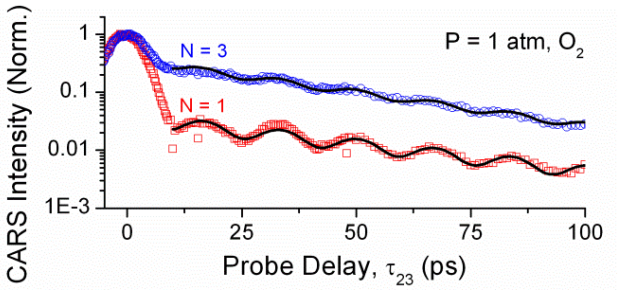

Figure 8.3. Decay of $N = 1$ and 3 rotational lines of O_2. Solid lines show measured oscillations due to triplet ground state with periods of 16.8 ps and 16.9 ps, respectively.

In summary, hybrid fs/ps RCARS was used to measure the collisional decay rates and individual *S*-branch transition linewidths of N_2 and O_2 from 1–20 atm. Excellent sensitivity to transition-resolved signal decay was achieved at high pressures where the rate constants are as low as 2.5 ps. Agreement was found with previous N_2 and O_2 *S*-branch measurements available at low pressure, which indicate a small positive offset from the MEG model. This relationship was confirmed at high pressures. The accuracy for low *J* levels of N_2 at higher pressure was bounded by a combination of nonresonant background, small decay rate constants, and low spectral intensity. In the case of O_2, oscillations in the time decay due to interference of the triplet ground state limited the accuracy of linewidth measurements for low rotational states.

Funding was provided by the National Science Foundation (CBET-1056006, Dr. A. Atreya, Program Official) and Air Force Office of Scientific Research (Drs. R. Parra and C. Li, Program Managers). J. Miller was supported by the National Science Foundation Graduate Fellowship Program. The authors also thank C. Dedic, M. Johnson, and B. Halls of Iowa State University.

8.4 References

1. S. Roy, J. R. Gord, and A. K. Patnaik, "Recent advances in coherent anti-Stokes Raman scattering spectroscopy: Fundamental developments and applications in reacting flows," *Prog. Energ. Combust.* **36**, 280–306 (2010).
2. G. Knopp, P. Beaud, P. Radi, M. Tulej, B. Bougie, D. Cannavo, and T. Gerber, "Pressure-dependent N_2 *Q*-branch fs-CARS measurements," *J. Raman Spectrosc.* **33**, 861–865 (2002).
3. M. Motzkus, T. Lang, H. M. Frey, and P. Beaud, "High resolution femtosecond coherent anti-Stokes Raman scattering: Determination of rotational constants, molecular anharmonicity, collisional line shifts, and temperature," *J. Chem. Phys.* **115**, 5418–5426 (2001).

4. C. J. Kliewer, Y. Gao, T. Seeger, J. Kiefer, B. D. Patterson, and T. B. Settersten, "Picosecond time-resolved pure-rotational coherent anti-Stokes Raman spectroscopy in sooting flames," *Proc. Combust. Inst.* **33**, 831–838 (2011).
5. W. D. Kulatilaka, P. S. Hsu, H. U. Stauffer, J. R. Gord, and S. Roy, "Direct measurement of rotationally resolved H_2 Q-branch Raman coherence lifetimes using time-resolved picosecond coherent anti-Stokes Raman scattering," *Appl. Phys. Lett.* **97**, 081112 (2010).
6. T. Seeger, J. Kiefer, A. Leipertz, B. D. Patterson, C. J. Kliewer, and T. B. Settersten, "Picosecond time-resolved pure-rotational coherent anti-Stokes Raman spectroscopy for N_2 thermometry," *Opt. Lett.* **34**, 3755–3757 (2009).
7. J. D. Miller, S. Roy, M. N. Slipchenko, J. R. Gord, and T. R. Meyer, "Single-shot gas-phase thermometry using pure-rotational hybrid femtosecond/picosecond coherent anti-Stokes Raman scattering," *Opt. Express* **19**, 15627–15640 (2011).
8. J. D. Miller, M. N. Slipchenko, T. R. Meyer, H. U. Stauffer, and J. R. Gord, "Hybrid femtosecond/picosecond coherent anti-Stokes Raman scattering for high-speed gas-phase thermometry," *Opt. Lett.* **35**, 2430–2432 (2010).
9. S. Roy, P. Wrzesinski, D. Pestov, T. Gunaratne, M. Dantus, and J. R. Gord, "Single-beam coherent anti-Stokes Raman scattering spectroscopy of N_2 using a shaped 7 fs laser pulse," *Appl. Phys. Lett.* **95**, 074102 (2009).
10. J. D. Miller, M. N. Slipchenko, and T. R. Meyer, "Probe-pulse optimization for nonresonant suppression in hybrid fs/ps coherent anti-Stokes Raman scattering at high temperature," *Opt. Express* **19**, 13326–13333 (2011).
11. T. Seeger, F. Beyrau, A. Brauer, and A. Leipertz, "High-pressure pure rotational CARS: comparison of temperature measurements with O_2, N_2 and synthetic air," *J. Raman Spectrosc.* **34**, 932–939 (2003).
12. M. Afzelius, P. E. Bengtsson, J. Bood, J. Bonamy, F. Chaussard, H. Berger, and T. Dreier, "Dual-broadband rotational CARS modeling of nitrogen at pressures up to 9 MPa. II. Rotational Raman line widths," *Appl. Phys. B* **75**, 771–778 (2002).
13. B. D. Prince, A. Chakraborty, B. M. Prince, and H. U. Stauffer, "Development of simultaneous frequency- and time-resolved coherent anti-Stokes Raman scattering for ultrafast detection of molecular Raman spectra," *J. Chem. Phys.* **125**, 044502 (2006).
14. L. A. Rahn and R. E. Palmer, "Studies of nitrogen self-broadening at high-temperature with inverse Raman-spectroscopy," *J. Opt. Soc. Am. B* **3**, 1164–1169 (1986).
15. L. Martinsson, P. E. Bengtsson, M. Alden, S. Kroll, and J. Bonamy, "A test of different rotational Raman linewidth models - Accuracy of rotational coherent anti-Stokes-Raman scattering thermometry in nitrogen from 295 K to 1850 K," *J. Chem. Phys.* **99**, 2466–2477 (1993).
16. M. Berard, P. Lallemand, J. P. Cebe, and M. Giraud, "Experimental and theoretical-analysis of the temperature-dependence of rotational Raman linewidths of oxygen," *J. Chem. Phys.* **78**, 672–687 (1983).
17. G. Millot, R. Saintloup, J. Santos, R. Chaux, H. Berger, and J. Bonamy, "Collisional effects in the stimulated Raman *Q* branch of O_2 and O_2-N_2," *J. Chem. Phys.* **96**, 961–971 (1992).

18. G. Fanjoux, G. Millot, and B. Lavorel, "Collisional shifting and broadening coefficients for the rovibrational anisotropic S(J) lines of nitrogen studied by inverse Raman spectroscopy," *J. Raman Spectrosc.* **27**, 475–483 (1996).

CHAPTER 9. CONCLUSIONS

9.1 Summary

A hybrid fs/ps CARS technique was developed for thermometric measurements in gas-phase reacting flows. This dissertation describes the ability to perform measurements at both high temperature (using vibrational fs/ps CARS) and low temperature (using rotational fs/ps CARS). Through optimization of the probe pulse characteristics, it was possible to minimize the influence of both nonresonant background and collisions, thereby eliminating a key source of temperature uncertainty in turbulent reacting flows. It was further shown that accurate temperature measurements could be made at kHz rates in unsteady flames, which is of potential use in studying combustion dynamics in practical combustors. Finally, the advantages of fs/ps CARS for studying the effects of collisions on CARS signal were demonstrated at various temperatures and pressures. This is useful for establishing key parameters needed to improve the accuracy of conventional ps or ns CARS experiments.

A theoretical framework for fs/ps CARS was developed in Chapter 3, which addresses the time-dependent nature of the resonant and nonresonant third-order polarization and phenomenological molecular response function. The molecular response function was constructed from fundamental molecular parameters available in the current literature, and accurate Raman transition strengths, frequencies, and linewidths were calculated. The influence of probe pulse shape ($sinc^2$, Gaussian, and time-asymmetric exponential) and delay on spectral CARS intensity was investigated using the theoretical model. An evolutionary optimization algorithm was then utilized to perform best-fit thermometry on experimental spectra for obtaining quantitative temperature measurements.

The first demonstration of fs/ps CARS for high-temperature measurements in a flame, as highlighted in Table 9.1 and detailed in Chapter 4, utilized vibrationally-excited *Q*-branch N_2. Using a 12-cm^{-1} $sinc^2$ probe with 2.36-ps delay, sufficient spectral resolution was obtained to perform frequency-domain thermometry while simultaneously suppressing nonresonant background by 100×. Using 500-Hz single-shot spectra, precision >1.8% and accuracy within 2.9% of equilibrium values were recorded, validating the applicability of fs/ps CARS for quantitative thermometry. Similar values were obtained for single-shot 1-kHz measurements from ~1400 K to 2400 K. Precision was found to increase with a reduction in temperature, while accuracy increased with an increase in temperature. Finally, 500-Hz measurements were performed in a pulsed H_2–air flame with sufficient acquisition bandwidth to resolve large-scale instabilities at 3 Hz and localized oscillations at 30 Hz.

The influence of probe pulse shape on nonresonant suppression at high temperature was investigated in Chapter 5. Two $sinc^2$ functions with Γ_{FWHM} = 6.5 cm^{-1} and 12 cm^{-1} were generated using a 4-*f* pulse shaper and compared with a time-asymmetric exponential pulse from a drop-in Lorentzian filter with Γ_{FWHM} = 13 cm^{-1}. The minimum probe delay for the $sinc^2$ pulses was limited to the first minimum of the function (5.5 ps and 2.77 ps respectively), while the time-asymmetric function rose rapidly with 1000× nonresonant suppression at 0.31 ps. At this delay and 2000 K, the time-asymmetric pulse yielded a signal-to-nonresonant background ratio of 112:1 while the $sinc^2$ ratio was 18:1 and 50:1 respectively. The time-asymmetric pulse shape is particularly useful under high-temperature or high-pressure conditions where initial decay of the Raman coherence is rapid. The time-asymmetric frequency-domain spectrum exhibited similar temperature sensitivity to the 4-*f* shaped pulses even with 2× greater resolution. The spectral sensitivity is primarily a function

of the ratio of the ground and first-excited vibrational transitions ($\Delta\omega \sim 30$ cm^{-1}) which was readily resolved by the Lorentzian filter ($\Gamma_{FWHM} = 13$ cm^{-1}).

Pure-rotational fs/ps CARS of N_2 was first demonstrated in Chapter 6 and shows excellent sensitivity at low temperature. Narrow-bandwidth 4-*f* pulse shaping was used to generate a 2.1-cm^{-1} Gaussian probe with sufficient bandwidth to resolve individual *S*-branch rotational transitions ($\Delta\omega \sim 8$ cm^{-1}). Nonresonant suppression of 1000× was achieved at a delay of 13.5 ps, and excellent temporal and spectral agreement was found between the experimental data and theoretical model. In agreement with ps CARS, it was observed that collisional energy transfer produces an apparent shift in spectral temperature with increasing probe delay since the low rotational states transfer energy more efficiently than high rotational states. The error associated with this process was quantified as a function of probe delay and temperature, with error reaching 10% at 300K for a 100-ps delay. At 500 K, this was reduced to 5% due to increased uniformity in the collision efficiency of all transitions. For the first time, a time- and frequency-resolved model was used to correct for this error at long delay times, while accurate temperature measurements were demonstrated up to 705 K neglecting collisional energy transfer at 13.5 ps.

Quantification of the collision-free assumption was detailed in Chapter 7 using pure-rotational fs/ps CARS of N_2 and O_2 at pressures up to 20 atm and probe delays of 150 ps. A rapid decrease in CARS signal with probe delay was observed at elevated pressure, placing greater significance on the use of a time-asymmetric exponential probe pulse. At 6.5 ps and 300 K, temperature measurements within 5% of the actual value were possible at pressures of 1–15 atm while neglecting collision energy transfer for both N_2 and O_2. Above 15 atm, energy transfer corrections using the Modified Exponential Gap model were necessary for

accurate thermometry. The apparent temperature shift was fit with an empirical model as a function of pressure and probe delay, allowing predictive analysis of collision-induced thermometry error. A time-asymmetric exponential probe pulse was introduced using a Fabry–Pérot etalon with Γ_{FWHM} = 5.6 cm^{-1}. This yielded sufficient spectral resolution to completely resolve even rotational transitions during the first ¼ recurrent feature at 2.1 ps and may provide a significant advantage over the Gaussian probe at high pressure.

The direct time-domain measurement of self-broadened N_2 and O_2 linewidths was performed at 300 K and pressure up to 20 atm as reported in Chapter 8. At 1 atm, the measured linewidths were in good agreement with the Modified Exponential Gap model and previous measurements of *S*-branch linewidths. The linewidths increased linearly with pressure for both N_2 and O_2 with values as high as 2.158 cm^{-1} and 1.881 cm^{-1} respectively at 20 atm. These are the first reported time-domain *S*-branch linewidth measurements for N_2 and O_2 at elevated pressure. Additionally, 1.99-cm^{-1} spacing between the triplet ground states of O_2 was observed and measured for low rotational states.

In conclusion, fs/ps CARS has been successfully applied for quantitative gas-phase thermometry of N_2 and O_2. A detailed theoretical treatment of the time- and frequency-resolved CARS signal was developed and applied for best-fit thermometry using frequency-domain experimental spectra. Single-shot measurement accuracy and precision within 2.9% was achieved at temperatures of ~2400 K while resolving transient combustion instabilities. Nonresonant suppression of 1000× was achieved with delays as short as 0.31 ps using time-asymmetric probe pulses. Pure-rotational fs/ps CARS was demonstrated with excellent temperature sensitivity up to 700 K and the influence of collision energy transfer was quantified at 300 and 500 K. Interference-free fs/ps RCARS was demonstrated up to 15 atm

for N_2 and O_2 at 300 K. The ability to resolve time-dependent features of the molecular response function was utilized to directly measure self-broadened Raman linewidths of N_2 and O_2 up to 20 atm and triplet spacing in ground state O_2.

Table 9.1. Significant innovations in CARS spectroscopy from this dissertation

Year	Innovation	Author
2010	Quantitative thermometry using hybrid fs/ps CARS (N_2)	Miller *et al.*, Opt. Lett.
2010	Single-shot 1-kHz thermometry using frequency-domain CARS	Miller
2011	Single-shot kHz-rate pure-rotational CARS	Miller *et al.*, Opt. Express
2011	Time-domain measurement of N_2 and O_2 Raman linewidths at pressures above 1 atm	Miller *et al.*, J. Chem. Phys.
2012	Single-shot nonresonant- and collision-free CARS thermometry	Miller *et al.*, Opt. Express

9.2 Directions for Future Work

While this dissertation validates the use of fs/ps CARS for high-speed interference-free gas-phase thermometry, several unsolved challenges remain providing a direction for future research in this field. First, although a 1-kHz measurement rate is sufficient for resolving combustion instabilities of up to 500 Hz, extension of the measurement bandwidth would increase its applicability to high-speed combustion. While extension to 10 kHz is possible using currently available regeneratively-amplified Ti:Sapphire lasers, the availability of low-noise high-speed spectroscopic cameras is a limiting factor. Several candidates have been proposed including high-speed intensified CMOS cameras and line-transfer CCD cameras although these can suffer from reduced resolution and increased noise at high repetition rates.

Second, a major limitation at high temperature is the decrease in signal-to-noise ratio. The pump and Stokes energy cannot be increased without risk of Raman pumping or interference from sustained molecular alignment, and the probe power is limited by the bandwidth. For narrow bandwidth probes pulses, up to 99% of the input energy is unused. The ability to maintain narrow probe bandwidth while increasing probe power is the most important issue facing the application of fs/ps CARS in practical combustors. Several solutions have been proposed including the use of multiple slits in the 4-*f* pulse shaper to further multiplex the CARS signal, amplification of the probe pulse after initial shaping, and the synchronization of multiple amplified systems using the same oscillator.

Third, the extension of CARS thermometry to higher dimensions is the subject of much current research. Line-CARS (from point to 1D) has been demonstrated with ps and fs CARS systems. The introduction of a line-fs/ps CARS system is not necessarily straightforward due to the limited narrow-bandwidth probe energy. However, current work in this field is ongoing, and is important for studying spatio-temporal dynamics in turbulent flames.

Finally, although not directly related to the experimental configuration of the fs/ps CARS technique, the volume of experimental data produced during a measurement campaign can easily stretch the limits of current CARS thermometry computer codes. Research into highly-efficient processing and fitting algorithms should be a focus of future work, along with the introduction of massively parallel processing. One potential solution is the use of graphical processing units (GPU) for parallel processing on a single desktop PC. This method can provide several teraflops of processing power on a small workstation which, when coupled with the Matlab Parallel Computing Toolbox, may provide a simple solution

for decreasing processing time for large CARS thermometry datasets. This could be particularly useful in producing the spectral libraries for multiple variables.

In conclusion, several areas of important research remain in the development of fs/ps CARS thermometry. These include the extension to 10-kHz measurement bandwidth, the increase of probe power while maintaining narrow bandwidth, the introduction of line CARS, and the development of highly-efficient CARS processing codes. The solution to these challenges provides a clear direction for future innovations in fs/ps CARS thermometry in practical combustors.

APPENDIX: HYCARS SPECTRAL FITTING CODE

The HyCARS spectral simulation code is implemented in 64-bit Matlab R2011b (7.13.0.564) for Mac (maci64). The code requires the Signal Processing and Curve Fitting Toolbox for the processing functions. The application of selected functions and sub-functions are described in detail in Chapter 3 and Fig. 3.16 specifically. As a baseline, a single fs/ps CARS spectrum can be generated in 4.2 s using the HyCARSMain.m function on a MacBook Pro running 64-bit OS X Lion (Version 10.7.3) with a 2.8 GHz Intel Core i7 and 4 GB 1333-MHz DDR3 memory.

Pre-Processing Functions

Function: "SpectraRead.m"

```
%% SpectraRead.m
%
%   Opens a .spe file generated from Andor Solis.
%
%   Updated Feb 20, 2012
%
%% Begin Code

clear; clc;

%% User Input

res = 0.01; %Resolution [mm]
numFrames = 500; %Number of frames
xres = 1600; %Number of x pixels (1600)
yres = 1; %Number of y pixels
bg = 0; %background file (0 = no, 1 = yes)
bnum = 50; %Number of background frames

%% Open File

OG = cd; %Set original execution folder
[fileName, pathName] = uigetfile({'*.spe'},'Open WinView .spe File');
```

```
%Determine file name and file path
cd(pathName); %Open file folder

fid = fopen(fileName,'r');
b = 1;
for a = 1:numFrames
    if b == 1
        header=fread(fid,1025,'float32'); %Header is at the beginning of
the first frame only
    end
    ImMat = fread(fid,xres*yres,'float32');
    rawIm = reshape(ImMat,xres,yres);
    rawData.Image(:,a) = rawIm;
    b = b + 1;
end
fclose(fid);
spec = rawData.Image;

clear ImMat rawIm rawData

if bg == 1

    [backName, backPath] = uigetfile({'*.spe'},'Open Background .spe
File'); %Determine file name and file path
    cd(backPath); %Open file folder

    fid=fopen(backName,'r');
    b = 1;
    for a = 1:bnum
        if b == 1
            header=fread(fid,1025,'float32'); %Header is at the beginning
of the first frame only
        end
        ImMat = fread(fid,xres*yres,'float32');
        rawIm = reshape(ImMat,xres,yres);
        rawData.Image(:,a) = rawIm;
        b = b + 1;
    end
    fclose(fid);

    Back = rawData.Image;
    avgBack = mean(Back,2);

else
    avgBack = zeros(xres,yres);
end

%% Subtract background

for i = 1:size(spec,2)
    subSpec(:,i) = spec(:,i) - avgBack;
end

%% Normalize Spectra
```

```
specNorm = zeros(size(subSpec,1),size(subSpec,2));
for i = 1:size(spec,2)
    specNorm(:,i) = subSpec(:,i)./max(subSpec(:,i));
end

%% Average Spectra

avgSpec = mean(subSpec(:,50:80),2);
avgBack = mean(subSpec(:,100:200),2);
realSpec = avgSpec - avgBack;
```

Processing Functions

Function: "HyCARSFit.m"

```
%% HyCARSFit.m
%
%   Fit the simulated CARS spectra to the experimental data using
%   Differential Evolution to minimize the residual with variables of
%   constant offset and scaling.  A databas of simulated spectra is
%   included for quantifying accuracy.  This script also fits the entire
%   series of data.  New addition includes Differential Evolution
selection
%   of best fit simulation to reduce processing time.
%
%% Begin Code

clear; clc;

%% User Inputs

num = 1; %Number of spectra to fit
lowTh = 11; %Lower threshold on simulated frequency [cm-1]
upTh = 199; %Upper threshold on simulated frequency [cm-1]

%% Select Simulated Database

og = cd;
[fileName,pathName] = uigetfile({'*.mat'},'Select Simulation Database');

cd(pathName);
database = load(fileName); %Simulation database
simDB = database.Out;
simFreq = simDB(2:end,1); %Simulation frequency vector
simData = simDB(2:end,2:end); %Simulation data vectors
simTemp = simDB(1,2:end)'; %Temperature of simulation

%% Select Experimental Data
```

```
[fileName,pathName] = uigetfile({'*.xlsx'},'Select Experimental Data');

cd(pathName);
Data = xlsread(fileName,'Sheet1'); %Simulation database
cd(og);

expFreq = Data(2:end,1); %Experimental frequency vector
expData = Data(2:end,2:end); %Experimental data vectors
expTime = Data(1,2:end)'; %Time of experimental spectra

ind = find(expFreq < upTh);
expFreq = expFreq(ind);
expData = expData(ind,:);

%% Resample Data
%Use timeseries variables to resample frequency data

tic

simDataRe = zeros(size(expFreq,1),size(simData,2));

for i = 1:length(simTemp)
    ts = timeseries(simData(:,i),simFreq,'name','Simulation');
    tsR = resample(ts,expFreq); %Use linear interpolation method
    simFreqRe = tsR.Time;
    simDataRe(:,i) = tsR.Data;

    lg = isnan(simDataRe(:,i));
    ind = find(lg == 1);
    TF = isempty(ind);

    if TF == 0
        simDataRe(ind,i) = 0;
    end
    clear ts tsR lg ind TF
end

X = zeros(num,3);
optSim = zeros(size(expFreq,1),num);
res = zeros(size(expFreq,1),num);

for j = 1:num %length(expTime)

    % Optimize Fit

    [f,X(j,:)] = DECARSFit(expData(:,j),simDataRe,size(simDataRe,2));

    %%
    amp = X(j,1);
    offset = X(j,2);
    ind = X(j,3);
    optSim(:,j) = amp*simDataRe(:,ind) + offset;
    [R(j,1),res(:,j)] = scale(expData(:,j),simDataRe,X(j,:));
    clear f amp offset
```

```
    % Find Best Fit

    bestT(j,1) = simTemp(ind);
    bOff = X(j,2);

    % Normalize Data

    mS = max(optSim(:,j) - bOff);
    mE = max(expData(:,j) - bOff);
    mX = max(mS,mE);

    simNorm(:,j) = (optSim(:,j) - bOff)./mX;
    expNorm(:,j) = (expData(:,j) - bOff)./mX;
    resNorm(:,j) = res(:,j)./mX;

    clear mS mE mX
    %%
end

OutputEX = zeros(length(expFreq),num+1);
OutputSM = zeros(length(expFreq),num+1);
OutputRE = zeros(length(expFreq),num+1);
OutputBF = zeros(num,4);

OutputEX(:,1) = expFreq;
OutputEX(:,2:end) = expNorm;

OutputSM(:,1) = expFreq;
OutputSM(:,2:end) = simNorm;

OutputRE(:,1) = expFreq;
OutputRE(:,2:end) = resNorm;

OutputBF(:,1) = bestT;
OutputBF(:,2) = R;
OutputBF(:,3) = X(:,1);
OutputBF(:,4) = X(:,2);

toc

%% Plot

plot(expFreq,expNorm,expFreq,simNorm,expFreq,resNorm);
```

Sub-Function: "DECARSFit.m"

```
function [f,X] = DECARSFit(exp,sim,num)

%Differential Evolution is an optimization algorithm developed by Ranier
%Storn and Ken Price
%This scrpit is modified and used with permission from "Differential
Evolution: In
```

```
%Search of Solutions" by Vitaliy Feoktistov, 2006

%% Control Parameters

D = 3; %Number of unknowns to solve
NP = 20; %Size of Population (at least 10*D)
F = .9; %Scale factor for differential (0-1)
CR = 0.8; %Crossover constant (.5-1)
GEN = 100; %Maximum number of generations (iterations)
L(1) = 0; %Low boundary constraint for input 1
H(1) = 100; %High boundary constraints for input 1
L(2) = -10000; %Low boundary constraint for input 2
H(2) = 10000; %High boundary constraints for input 2
L(3) = 1; %Low boundary constraint for input 2
H(3) = num; %High boundary constraints for input 2

%% Initialize Variables

X = zeros(D,1); %Trial vector
Pop = zeros(D,NP); %Population
Fit = zeros(1,NP); %Fitness of the population
iBest = 1; %Index of the best solution
r = zeros(3,1); %Randomly selected indices

%% Create Population

rand('state',sum(100*clock));
for j = 1:NP
    Pop(1,j) = L(1) + (H(1)-L(1))*rand;
    Pop(2,j) = L(2) + (H(2)-L(2))*rand;
    Pop(3,j) = round(L(3) + (H(3)-L(3))*rand);
    Fit(1,j) = scale(exp,sim,Pop(:,j));
end

%% Optimization

for g = 1:GEN
    for j = 1:NP

        %Choose 3 random individuals from the population which are
mutually
        %different

        r(1) = floor(rand*NP) + 1;
        while r(1) == j
            r(1) = floor(rand*NP) +1;
        end
        r(2) = floor(rand*NP) + 1;
        while (r(2) == r(1)) || (r(2) == j)
            r(2) = floor(rand*NP) +1;
        end
        r(3) = floor(rand*NP) + 1;
        while (r(3) == r(2)) || (r(3) == r(1)) || (r(3) == j)
            r(3) = floor(rand*NP) +1;
        end
```

```
        %Create the trial individual in which at least 1 parameter is
        %changed

        Rnd = floor(rand*D) + 1;
        for i = 1:D
            if (rand < CR) || (Rnd == i)
                if i == 3
                    X(i) = round(Pop(i,r(3)) + F*(Pop(i,r(1)) -
Pop(i,r(2))));
                else
                    X(i) = Pop(i,r(3)) + F*(Pop(i,r(1)) - Pop(i,r(2)));
                end
            else
                X(i) = Pop(i,j);
            end
        end

        %Verify boundary constraints
        for i = 1:D
            if (X(i) < L(i)) || (X(i) > H(i))
                if i == 3
                    X(i) = round(L(i) + (H(i)-L(i))*rand);
                else
                    X(i) = L(i) + (H(i)-L(i))*rand;
                end
            end
        end

        %Select the best individual between the trial and current vectors
        %and calculate the fitness of the trial individual

        f = scale(exp,sim,X);
        if f <= Fit(j)
            Pop(:,j) = X;
            Fit(j) = f;
            if f <= Fit(iBest)
                iBest = j;
            end
        end
    end

end

%% Results

f = Fit(iBest);
X = Pop(:,iBest);
```

Sub-Function: "scale.m"

```
function [R,res] = scale(expdata,simdata,X)

amp = X(1);
```

```
offset = X(2);
ind = X(3);
res = expdata - (amp*simdata(:,ind) + offset);
R = (sum(abs(res)))^2;
```

ACKNOWLEDGEMENTS

I would be remiss to begin without first saying that none of this work would be possible without the patience and support of my advisor, Dr. Terrence Meyer. He has encouraged me to try new things, never discouraged me from pursuing a crazy idea, set his expectations incredibly high but always helped me achieve them, and I can think of no other person I would rather have as a doctoral advisor. It has been a privilege to learn from him, from the time I was a high school intern at Wright-Patterson AFB through my dissertation research at Iowa State. Through a 20-hour drive to NASA Langley, two months in Erlangen, countless late night conversations and data collection campaigns, broken lasers, 40 revisions on journal manuscripts, and enthusiastic discussions centered on what makes a good name for a laser, Terry has made my years in graduate school truly memorable!

In addition, I am grateful to my committee members, Dr. Rodney Fox, Dr. James Gord, Dr. Mike Olsen, Dr. Shankar Subramaniam, and Dr. Jigang Wang, who have contributed significantly to my research. Thank you for actively taking part in this process and providing encouragement as I finish. I am also indebted to a group of excellent scientists who continue to have a significant impact on my research, career, and life. Chief among these is Dr. James Gord. Jim gave me my first shot at combustion diagnostics research in 2002 and has been a constant encouragement and support ever since. Without Jim, I fear I would be sitting in a tiny cubicle under fluorescent lighting designing the same widget over and over and over again. Thank you for introducing me to the world of lasers and chemical physics, and fueling my desire to pursue my Ph.D. Dr. Sukesh Roy and Dr. Hans Stauffer have been the impetus of many of the ideas in this dissertation and always willing to help me

when I can't figure out a particularly perplexing topic. Finally, I believe that Dr. Mikhail Slipchenko may have magical powers. He is the only person who can make an experiment work just by walking in the room! My experimental skills are a result of many hours in the lab under his tutelage as a first year grad student.

I cannot thank my lab mates enough for their support and encouragement when I was convinced I would never graduate. Special thanks go to Jake Schmidt and Dr. Derek Wissmiller who made the first years of grad school hilarious. Dr. Aravind Viadyanathan always provided a smile and plenty of hope and joy! Maybe one day I will reach demi-god status. More recently Dr. Miao Li, Mark Cecconi, Jordan Tiarks, Clint Moody, Harish Subramani, and Praveen Kumar have been a joy to work with in the lab. A special thanks goes to Ben Halls for helping me procrastinate by talking about football and astrophysics, and for being so good at building things. You put me to shame. Chloe Dedic has been an incredible help in the lab and this dissertation would be significantly shorter without her assistance. I just hope she remembers me when she is famous! I am also grateful to so many undergraduate assistants who have invested time in the fs/ps CARS work: Tony Lanphier, Micayla Haugen, Kathy Schuller, Mike Romey, Kate Kuehn, and Mark Johnson.

It has been my privilege to study with support from the Department of Defense through the National Defense Science and Engineering Graduate Fellowship Program, and National Science Foundation through the Graduate Research Fellowship program. I am also thankful to Sascha Engel, Johannes Tröger, Prof. Thomas Seeger and Prof. Alfred Leipertz for making my time abroad in Erlangen, Germany so productive and enjoyable!

While my dissertation research has taken the better part of five years, the journey really began much earlier. I would like to personally thank Mr. Tom Minor who instilled in

me a love for physics and chemistry in high school, and taught me dimensional analysis which I am still using and teaching today. I am also grateful to Prof. Harwood Hegna who was always willing to talk and offer excellent advice during my time at Cedarville University.

This would never have been possible without an excellent group of supportive friends: Nathan and Sarah Compton, Chris and Lyndee Heemstra, and Jesse and Erin Doyle. I am eternally grateful for your support and encouragement every week to keep on going.

Most importantly, my family has played a vital role in shaping who I am. My in-laws, David and Brenda Terpstra, have been incredibly supportive in every aspect of this journey, including editing this dissertation! I would like to say thank you to my brothers, Andy and John, who are both exceptional musicians and helped me to better understand my research through the analogy of music. My parents, Dan and Chris Miller, have always supported me, even when they had to sacrifice to do so. Thank you for patiently raising me and providing amazing experiences including the opportunity to attend Dayton Christian and Cedarville. I am forever grateful for your godly example.

Lana, how can I ever say enough thanks for supporting me through the hardest years of my life. You have sacrificed and given more of yourself to support me than I deserve. Still, you have made these the best years of my life and I can't believe I was lucky enough to experience them with you! Looking forward to our next great experiment in July …

Finally, I have been truly blessed to "think God's thoughts after Him" in regards to the "book of nature." It is His grace that has sustained me, for He is the Maker of the invisible, the Creator of all things, and the Author of my salvation. *Soli Deo gloria*.

VITA

NAME OF AUTHOR: Joseph Daniel Miller

DATE AND PLACE OF BIRTH: March 26, 1984, Dayton, Ohio

DEGREES AWARDED:

B.S. in Mechanical Engineering, Cedarville University, Cedarville, OH, 2006
Dipl., Dayton Christian High School, Dayton, OH, 2002

HONORS AND AWARDS:

Research Excellence Award, Iowa State University, 2011
National Science Foundation, Graduate Research Fellowship, 2009–2012
Department of Defense, National Defense Science and Engineering Graduate Fellowship, 2007–2010
Department of Defense, Science, Mathematics, and Research for Transformation Scholarship, 2005–2006
Ohio Board of Regents, Ohio Academic Scholarship, 2002–2004

PROFESSIONAL EXPERIENCE:

Research Assistant, Department of Mechanical Engineering, Iowa State University, Ames, IA, 2007–2012
Guest Scientist, Erlangen Graduate School in Advanced Optical Technologies (SAOT), University of Erlangen-Nürnberg, Erlangen, Germany, 2010–2011
Associate Mechanical Engineer, Air Force Research Laboratory, Propulsion Directorate, Wright-Patterson Air Force Base, OH, 2006–2007

ARCHIVAL PUBLICATIONS:

J.D. Miller, S.R. Engel, J.W. Tröger, T.R. Meyer, T. Seeger, and A. Leipertz, "Characterization of a CH planar laser-induced fluorescence imaging system using a kHz-rate multimode-pumped optical parametric oscillator," *Appl. Opt*. **51**, 2589–2600 (2012).

M.N. Slipchenko, J.D. Miller, S. Roy, J.R. Gord, S.A. Danczyk, and T.R. Meyer, "Quasi-continuous burst-mode laser for high-speed planar imaging," *Opt. Lett.* **37**, 1346–1348 (2012).

H.U. Stauffer, J.D. Miller, S. Roy, J.R. Gord, and T.R. Meyer "Communication: Hybrid femtosecond/ picosecond rotational coherent anti-Stokes Raman scattering thermometry using a narrowband time-asymmetric probe pulse," *J. Chem. Phys.* **136**, 111101 (2012).

J.D. Miller, C.E. Dedic, S. Roy, J.R. Gord, and T.R. Meyer, "Interference-free gas-phase thermometry at elevated pressure using hybrid femtosecond/picosecond coherent anti-Stokes Raman scattering," *Opt. Express* **20**, 5003–5010 (2012).

A.C. Lynch, R.G. Batchelor, B.V. Kiel, J.D. Miller, J.R. Gord, and M.F. Reeder, "Spray-characteristics of a pressure-swirl fuel injector subjected to a crossflow and a coflow," *Atomization Sprays* **21**, 625–643 (2011).

J.D. Miller, S. Roy, J.R. Gord, and T.R. Meyer, "Communication: Time-domain measurement of high-pressure N_2 and O_2 self-broadened linewidths using hybrid femtosecond/picosecond coherent anti-Stokes Raman scattering," *J. Chem. Phys.* **135**, 201104 (2011).

J.D. Miller, S.R. Engel, T.R. Meyer, T. Seeger, and A. Leipertz, "High-speed CH planar laser-induced fluorescence imaging using a multimode-pumped optical parametric oscillator," *Opt. Lett.* **36**, 3927–3929 (2011).

J.D. Miller, S.Roy, M.N. Slipchenko, J.R. Gord, and T.R. Meyer, "Single-shot gas-phase thermometry using pure-rotational hybrid femtosecond/picosecond coherent anti-Stokes Raman scattering," *Opt. Express* **19**, 15627–15640 (2011).

J.D. Miller, M.N. Slipchenko, and T.R. Meyer, "Probe pulse optimization for nonresonant background suppression in hybrid fs/ps coherent anti-Stokes Raman scattering at high temperature," *Opt. Express* **19**, 13326–13333 (2011).

N. Jiang, M. Webster, W. R. Lempert, J. D. Miller, T. R. Meyer, C. B. Ivey, and P. M. Danehy, "MHz-rate NO PLIF imaging in a Mach 10 hypersonic wind tunnel," *Appl. Opt.* **50**, A20–A28 (2011).

J.D. Miller, M. N. Slipchenko, T. R. Meyer, H. U. Stauffer, and J. R. Gord, "Hybrid fs/ps coherent anti-Stokes Raman scattering for high-speed gas-phase thermometry," *Opt. Lett.* **35**, 2430–2432 (2010).

J.D. Miller, M.N. Slipchenko, T.R. Meyer, N. Jiang, W.R. Lempert, and J.R. Gord, "Ultrahigh-frame-rate OH fluorescence imaging in turbulent flames using a burst-mode optical parametric oscillator," *Opt. Lett.* **34**, 1309–1311 (2009).

N. Jiang, W.R. Lempert, M.N. Slipchenko, J.D. Miller, T.R. Meyer, and J.R. Gord, "High-power UV lasers: Tunable ultraviolet burst-mode laser system produces high-energy pulses," *Laser Focus World* **44**, 79–83 (2008).

T.R. Meyer, S. Roy, T.N. Anderson, J.D. Miller, V.R. Katta, R.P. Lucht, and J.R. Gord, "Measurements of temperature and OH mole fraction up to 20 kHz by using a diode-laser-based UV absorption sensor," *Appl. Opt.* **44**, 6729–6740 (2005).